Feasibility Study on Sensitive Partial Discharge Measurements on Long Cable Systems

Saliha Abdul Madhar

Master Thesis

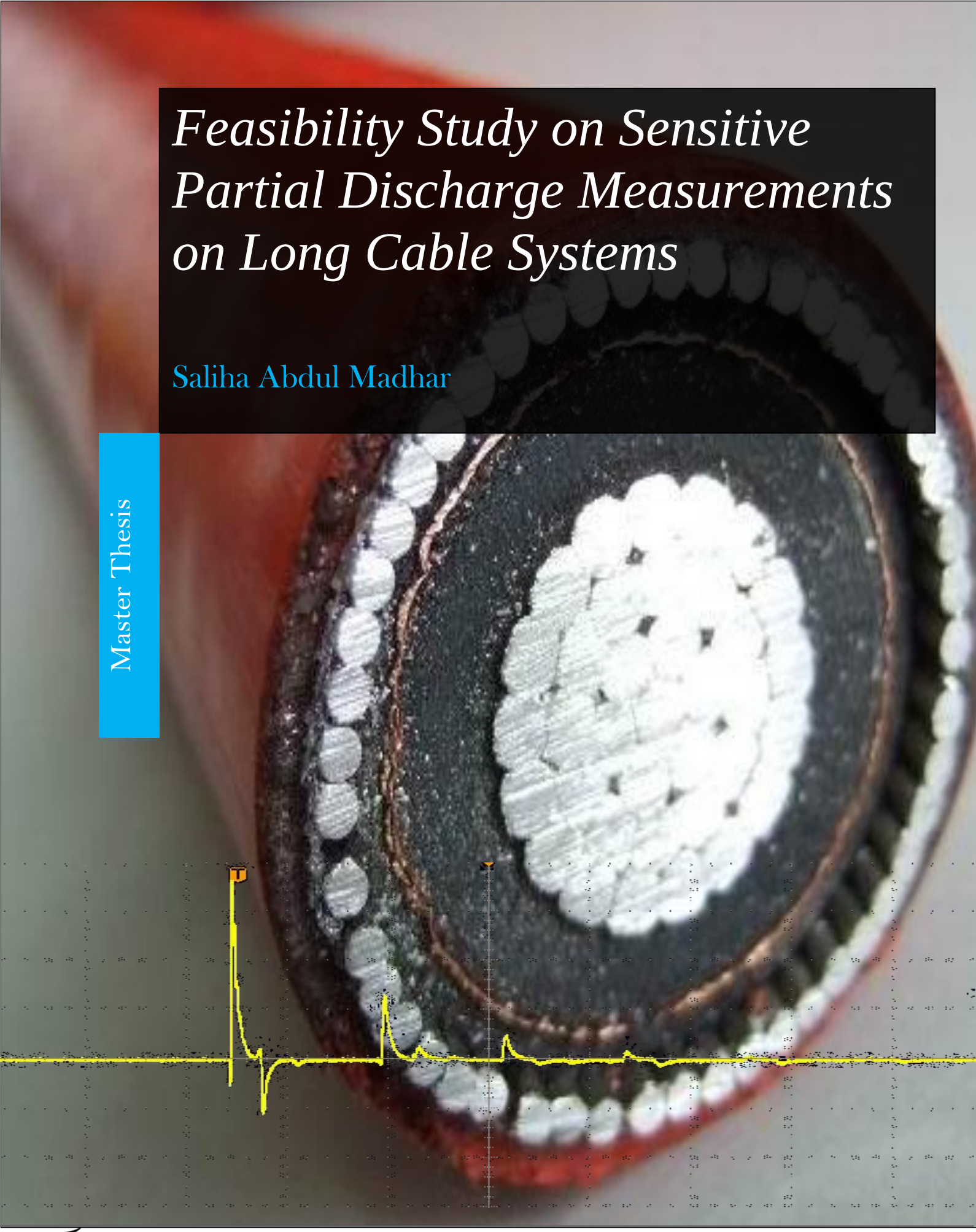

TU Delft Delft University of Technology

Challenge the future

Feasibility Study on Sensitive Partial Discharge Measurements on Long Cable Systems

by

Saliha Abdul Madhar
4512197

in partial fulfilment of the requirements for the degrees of

Master of Science
in Electrical Sustainable Energy

at the Delft University of Technology.
To be defended publicly on Friday September 22, 2017 at 10am

Supervisor:	Dr.ir.A. Rodrigo Mor	TU Delft
Co-supervisor:	Ir.B.C. van Maanen	DNV GL
Thesis Committee:	Prof. ir. Peter Vaessen	TU Delft
	Prof. dr. ir. E.F. Steennis	TU Eindhoven
	Dr. ir. A. Rodrigo Mor	TU Delft
	Ir. B.C. van Maanen	DNV GL

An electronic version of this thesis is available at http://repository.tudelft.nl/.

TU Delft

DCE&S
DC systems, Energy conversion & Storage

DNV·GL

Front cover: *Aluminium wire armoured, PVC sheath, single phase, XLPE, 6/10 (12) kV, underground power cable. Courtesy: Shenghua cables.*

Abstract

The phenomenon of partial discharge has been long studied in various power components and in recent times, it has been agreed that the occurrence of such discharges can be considered as a vital parameter of component health. Partial discharges in power cables is a pervasive phenomenon that over time may lead to failure. For this reason, their monitoring has become increasingly sought after by asset owners. Nevertheless, the symmetry in the structure of a coaxial cable makes the isolation of the discharges in power cable more complicated when compared to other power components. In addition to this, there are added limitations to a given system with regard to the sensitivity of measurements and the maximum length of cable monitored, due to the increased attenuation towards high frequencies. Therefore, this thesis investigates the possible methods that could be used for online-monitoring of sensitive partial discharges ($\sim$10 pC) in long cable systems ($>$10 km), by means of new techniques or new applications of existing techniques.

In this thesis a comprehensive feasibility study is followed by a thorough evaluation of the most promising methods and a demonstration of proof of concept of the parts thereof. The prime focus of this thesis is to investigate distributed measurement over a long cable system with the help of built-in sensor units. A built-in capacitive sensor type is modelled analytically, and simulated to check its performance before being tested experimentally in the last phase of this project. The final results indicate the feasibility of its implementation. Furthermore, the possibility of communication between such distributed sensor nodes is explored. One such method of communication proposed in this thesis is the wireless communication inside a cable using antennas. This thesis proves and quantifies to a certain extent the performance of an antenna (transceivers) inside a coaxial power cable paving the way for other tailor-made applications using 'RFID-like' (Radio Frequency Identification) technology in the future.

Acknowledgements

I would like to extend my sincere gratitude to my supervisor Dr.ir.Armando Rodrigo Mor for his constant guidance, not just during the time of the thesis, but during the entire 2 year period of my master study at TU Delft. This project would not have been possible without his support and encouragement. My deepest thanks to my co-supervisor at DNV GL, Ir.Bernd van Maanen for being a part of several brainstorming sessions and pushing me towards my goal. I would like to thank him for believing in my ability and giving me this splendid opportunity to work with a great company like DNV GL. I would also like to thank my thesis committee Chair, Prof.ir.Peter Vaessen for his encouragement and involvement in the project, his wise words have helped me tremendously.

This section is incomplete without thanking the three great mentors at DNV GL who extended their unconditional guidance and support; Prof.dr.ir.Fred Steenis, Dr.Paul Wagenaars and Dr.Peter van der Wielen. The ideas they pitched in always kept me thinking. I would like to express a special heart felt gratitude to Paul for his valuable insights and for patiently bearing with me during several of our discussions. I would also like to thank my other colleagues at the company Assido, Edwin, Shreya, Wim among many others for their motivation and support. Special thanks to Dr.Ramiro Serra for his keen interest and his valuable time. His timely help and guidance deserves a heartfelt appreciation.

I would like to take this opportunity to thank Radek, Wim and Remko for helping me setting up my experiments at the High voltage lab at TU Delft. And of course, all my friends, from all around the world for their support during crucial times, my apologies for not mentioning each of them by their names.

Lastly, but certainly one of the most important, I would like to take a moment to thank my family, my parents for their love and prayers and my sister for her constructive criticism. And the rest of my extended family, my uncles, aunts, grandparents and cousins who have been there for me during thick and thin. I am lucky to have so many people in my life who wish so well for me. At the end of the day, none of this would have been possible without the willingness of the Almighty, All praise be to him (SubhanAllah), no day shall pass without His remembrance.

CONTENTS

LIST OF FIGURES

LIST OF TABLES

'Indeed, with hardship comes ease'

CHAPTER

1

INTRODUCTION

1.1 Background

Partial discharge (PD) as the name indicates is a phenomenon in High Voltage (HV) where the discharge partially bridges the dielectric between two electrodes. Although the magnitude of such discharges is small, it could progressively lead to failure [1].Hence, partial discharges could be considered as both the symptom and the cause of insulation deterioration. Failure statistics in power equipment like transformers and GIS show that around 50% of the equipment failure is due to insulation breakdown. Owing to which newly installed equipment are faced with strict quality assurance tests, one of which involves the partial discharge test (according to IEC 60270) in order to confirm the fitness of the unit before installation. While on the contrary HV equipment that have been in operation for several years and are approaching the end of their life need a method to parametrize their component health and estimate remaining life. Especially when the concerned high power equipment is crucial to the operation of the grid, like the high voltage power cable, and unexpected failures need to be avoided, demand for a robust and continuous monitoring mechanism becomes crucial. Partial discharge monitoring is one such tool.

In most cases, partial discharges can be considered as a precursor of failure. However, it is not possible to estimate the remaining life of the defective component that

is generating the partial discharges [2]. This claim is supported by the knowledge rules derived from the large database of KEMA Laboratories (DNV GL), having diagnosed more than 7000 km of cable circuit. Therefore, this necessitates the continuous and online monitoring of partial discharges in crucial power components, for instance the power cables. The major limitation in PD detection specifically in cable systems is the drastic attenuation of the high frequency components of the PD pulse which is an inherent characteristic of the power cable. This limits the maximum length of cable circuit that can be monitored with a given sensitivity. Most commonly used methods of detection are the electrical methods which estimate the apparent charge by measuring the current or voltage pulse, but there are also a wide variety of non-electrical methods for the detection of partial discharges as shown in Figure 1.1.

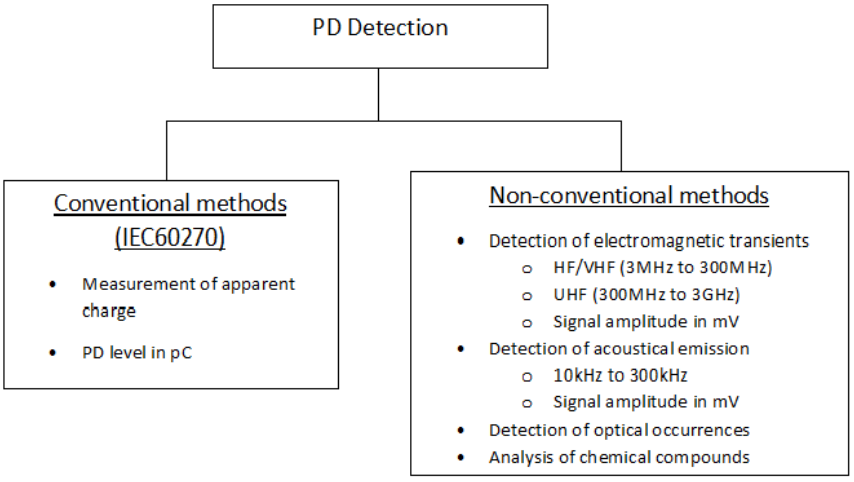

Figure 1.1: PD Detection methods [3]

1.2 Motivation

With increasing cross-border trade of energy, the energy market is becoming competitive like never before. This stresses on the need to develop new and improved strategies of asset condition monitoring to ensure smooth business operations. Currently, the increasing share of investment in offshore wind projects around Europe and globally, predict a steep rise in the market for inter-connectors and long sub-sea cables. And subsequently the need for a well-designed, robust and highly reliable cable system emerges. Furthermore, the tremendous costs involved in the outage,

service and repair of such arterial cable circuits sparks interest in new research towards the possibilities of implementing a reliable and continuous asset condition monitoring system, that would allow for preventive and condition based maintenance; thereby, delivering large savings.

Nevertheless, from state of the art it is evident that there exist no reliable methods to check PD activity online on cable lengths greater than 10 km with sensitivities of approximately 10 pC. Moreover, electrical methods of detection have dominated the field of PD monitoring in power cables due to obvious reasons of simplicity and good sensitivity but this does not prove that there are no alternative potential techniques. This dire need to bridge the knowledge gap and to extend the scope of existing technologies gives rise to a project such as this one.

1.3 State of the art

Off-line tests for partial discharge measurements on power cables are well designed [4] [5] and the IEC standard IEC60270 specifies its requirements. The VLF (Very Low Frequency) or 0.1 Hz partial discharge test, being one of the most commonly used, measures with one sensor connected to one end of the cable with the other end of the cable left open or disconnected. The sensor is normally a capacitive divider or an inductive core and it employs a low frequency source to energize the cable to keep the capacitive charging currents small. The discharges are then localized based on the PD pulse and its reflections at the cable end. However, these methods are limited by the attenuation of the pulse and can be used for cable lengths up to 4 km only. The method of PD detection using two sensors connected at both cable ends is proposed in [6]. With this technique, it is possible to extend on-line PD monitoring to cable lengths up to 8-10 km with a sensitivity of 100 pC.

Tian et al [7] investigates several potential methods of on-line PD detection, namely the use of capacitive couplers, Acoustic Emission (AE) sensors and Radio Frequency Current Transducers (RFCT). The AE detection sensitivity is very low due to the drastic attenuation of the AE signal in cable joints and hence the technique was rendered unavailing in comparison to the two others. Some others, such as [8] investigates the application of four different sensor technologies for power cables namely, HF pulse current sensor, AE sensor, Transient Earth Voltage (TEV) sensor and UHF Electromagnetic wave sensor. It makes recommendations on the bandwidth of operation of each of the given sensors and their suitable position of installation in the cable circuit. [9] Demonstrates a novel method of PD detection in MV power cables with the sensors located on cable ends. It employs an inductive sensor in the form of a toroid with a ferro-magnetic core to improve the pick-up sensitivity. It also

further describes the various propagation channels of the PD pulse and in conclusion recommends the most ideal location for the installation of the sensor, which is past the last earth connection at the substation. The localization accuracy is around 1% of the total length of circuit analyzed. The technique is further extended in [10] where two time synchronized sensors are used for defect localization, this is called PD Detection On-line with Localization (PDOL, now referred to as the Smart Cable Guard or SCG). It uses a pulse injection method for time synchronization of the two sensors. The pulses are injected and measured by the sensors on both cable ends, based on the pulse velocity and the time delay between the two pulses the defect is localized. E.Azordegan et al. in [11] describe a method of condition inspection of porcelain insulators by EM radiation signature. It utilizes a wideband electric field sensor which provides a voltage at its terminals proportional to the time derivative of the electric field flux. Conversely, this technique is not of direct applicability in the field of power cables as the electric field radiated by a PD pulse is confined to the coaxial cable. This is because at these high frequencies the skin depth is in the order of micrometers and the PD is considered as a travelling wave within the coaxial structure of the cable acting as a wave guide. Further,[12][13] reflects upon the influence of the semi-conductive layer in the power cable on the transmission and localization of the PD pulse. And [14] gives an equivalent model for the semi-conducting layer taking into consideration the current distribution due to skin effect and its effect on wave propagation and transient characteristics of the cable.

Non-electrical methods of PD detection such as using fiber optic sensor for acoustic emission detection as described in [15] are also of interest as these measurement channels are free from electrical interference. These sensors are commonly employed in GIS and indoor joints and have a performance comparable to commercially developed TEV sensors. However, their direct application in power cable is not a possibility due to the lack of required range and sensitivity.

1.4 Scope of the thesis

This project aims at assessing possible solutions (feasibility check) for highly sensitive (order of 10 pC) partial discharge measurements to be performed on long AC cables ($>$ 10 km). One proposed potential solution that is a part of the study is the application of distributed sensors that are embedded in the power cable during production. This provides the prospect of achieving better sensitivities over a short range, since the existence of noise yields a poor SNR with greater distance. The project investigates potential opportunities with extruded cables and looks at applications that can be implemented in new cable systems instead of existing cables

in the field.

Relevant background information that is studied during the course of the project includes that regarding cables, cable systems and their construction, ageing mechanisms, theory of PDs, PD measurement techniques, PD sensors, PD characteristics and travelling wave theory among others.

This project examines multiple potential techniques for the PD sensing application in order to pick the more suitable alternative. The theoretical assessment of the most promising solutions is supported by practical set-ups to show proof of concept or parts thereof.

1.5 Problem statement

The problem statement of this thesis project can be formulated as follows:

The current systems for measuring PDs in cables are limited by length of circuit (<10 km) as the electrical pulse from the Partial Discharge gets attenuated beyond the sensitivity of conventional measuring systems. Therefore, there is a need to extend the range and sensitivity of these systems.

1.5.1 Research goals

Main research question:

How to detect and measure Partial Discharges in long cable systems?

The main research question is an amalgamation of several others as listed below:

1. Which PD sensing technology is most suitable for long power cables?
2. Is it feasible to implement sensors distributed along the cable? If yes, what are the requirements and constraints of such a system?
3. How will the multiple sensors synchronize and communicate?
4. What will be the performance of such a system?

1.6 Thesis layout

This thesis presents in Chapter 2 the technical details and the physics associated with the problem. In Chapter 3, the results of the feasibility study are presented with selected simulation and estimation results. The anticipated design of the final sensor is presented in Chapter 4. The system engineering approach is adopted here to deal with design challenges. In Chapter 5 the PD sensor alternatives with the most promising outcomes in the first phase are analysed in greater detail using MATLAB simulations to predict their performance. At the end of which, one final choice of the PD sensor is chosen. Laboratory measurements on the built-in capacitive sensor and transceivers in power cables is discussed in Chapter 6. It concludes with a thorough analysis of the outcomes of the experimental phase. Finally, the last chapter, Chapter 7 summarizes the outcomes of the entire research with some concluding remarks and recommendations for further investigation. Figure 1.2 describes the research methodology adopted and the associated steps by means of a flow chart.

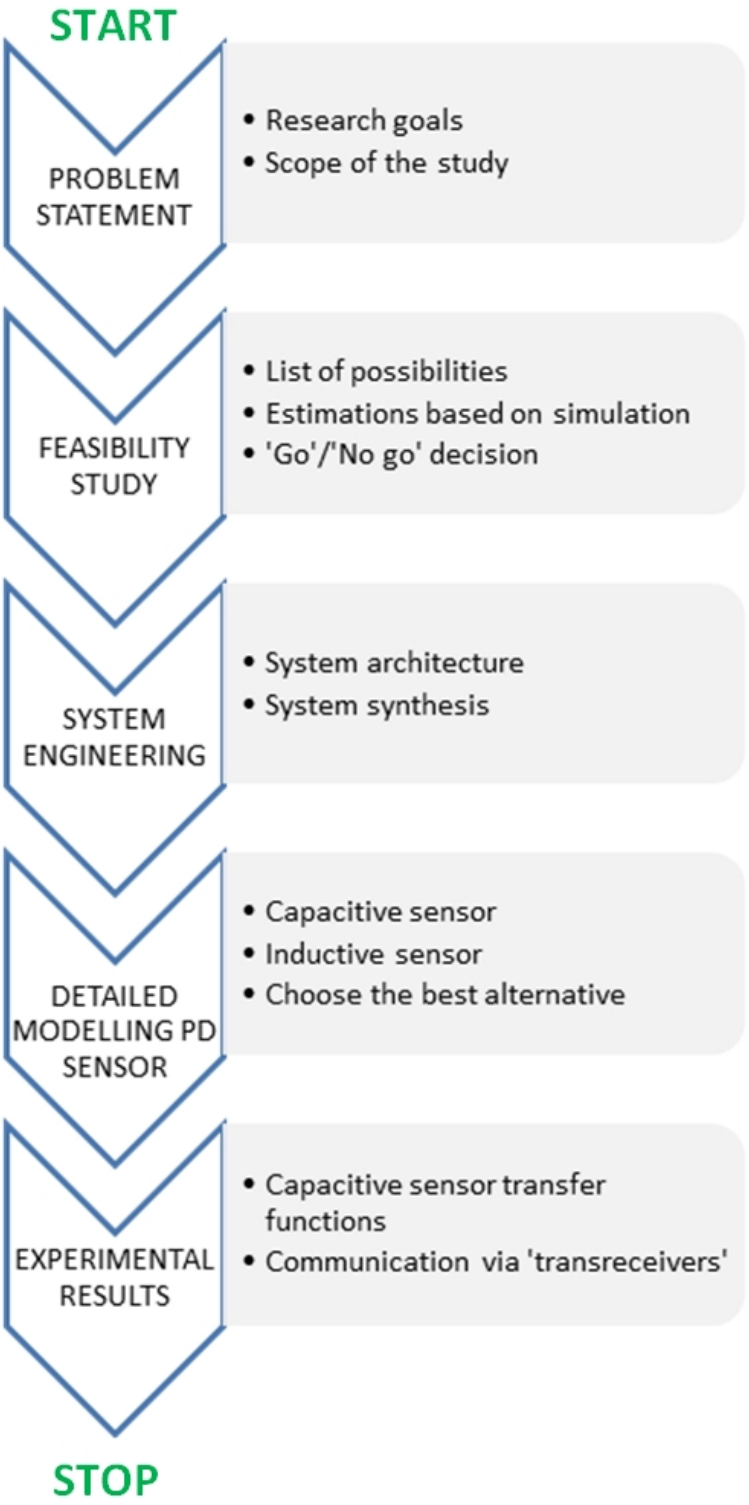

Figure 1.2: Research methodology

CHAPTER

2

THE PHYSICS OF PD PULSE

2.1 Introduction

This chapter presents the underlying physics associated with a partial discharge pulse. Selected technical information on the topic that is vital for comprehending the complex partial discharge phenomenon and its propagation along the power cable is described in this chapter. The following subjects are discussed in detail, namely, the partial discharge model, travelling wave theory, cable construction and the influence of semiconducting layers. The last section of this chapter validates a high frequency cable model from literature in order to facilitate its application during the modelling phase of this project.

2.2 Partial Discharge model

In order to formulate new and innovative techniques to measure and monitor partial discharges it is vital to understand the underlying mechanism. During the occurrence of a PD the voltage across the defect is largely neutralized, followed by a redistribution of charges in the metal shields and interfaces surrounding the dielectric. This causes a small voltage pulse in the nanosecond (ns) range. This voltage

pulse couples dominantly to the coaxial wave guide i.e. to the conductor and the earth screen of the cable and propagates through it in the TEM (Transverse Electro Magnetic) mode. Most of the electrical detection techniques rely on this principle for its detection.

In [1], F.H.Kreuger describes the behaviour of the voltage and currents from a partial discharge with the well-known abc-circuit as shown in Figure 2.1. C_c represents the capacitance of the configuration that breaks down, the capacitance C_b in series with it is used to represent the capacitance of the remaining healthy dielectric. The remaining part of the dielectric is represented by capacitance C_a, this is in most cases equivalent to the capacitance of the entire sample.

Under the condition $C_a >> C_c >> C_b$, which is most commonly the case, the charge is approximated by [1];

$$q_c \approx \triangle V_c(C_b + C_c) \tag{2.1}$$

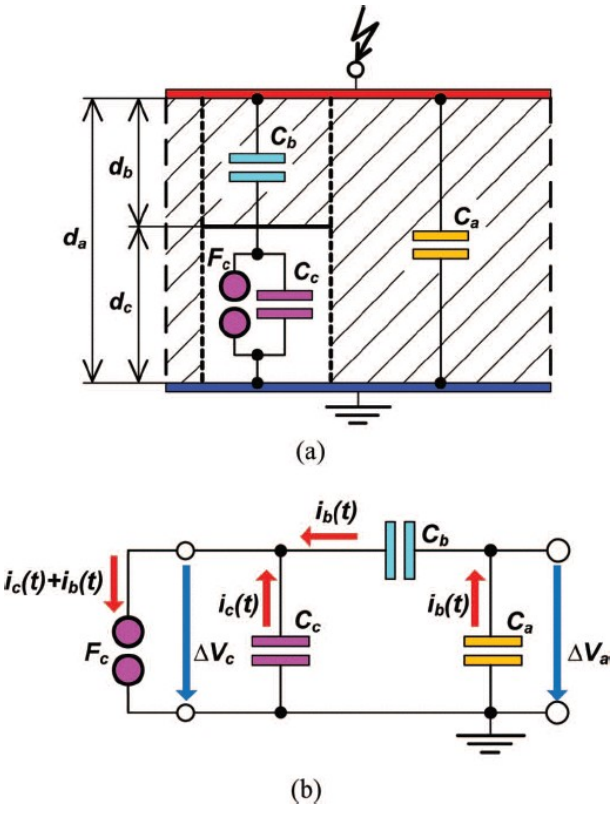

Figure 2.1: Capacitive partial discharge model. (a)showing the passive circuit elements (b)transient currents through the model[16]

.

From the transient model shown in Figure 2.1 it can be estimated that the external charge detectable at the terminals of the sample is;

$$q_a = \triangle V_a.C_a \approx \triangle V_c.C_b \tag{2.2}$$

From Eq.2.1 and 2.2, we obtain;

$$q_a = q_c \frac{C_b}{C_b + C_c} \approx q_c \frac{C_b}{C_c} \tag{2.3}$$

And from the condition assumed that $C_c >> C_b$, the external charge detectable at the terminals of the sample is much lower than the actual internal discharge. Thus the international testing standards for partial discharge IEC 60270[17] is quoted as saying "The apparent charge detectable at the terminals of the test object is not equal to the amount of that charge involved at the site of the discharge, which cannot be measured directly". This model of partial discharge based on the estimation of apparent charge is challenged and refuted by many including [16] using the Pedersen model of partial discharges which proposes a field theoretical approach based on the dipole model.

2.3 Travelling Wave Theory

All circuit voltage and current equations in the cable can be described by the travelling wave theory through the 'Telegraphers equations'. The telegraph equations are a set of 2 equations given in Eq.2.4 and 2.5, they are a generalization of the Kirchoff's law at high frequency on one hand and a special case of Maxwell's curl equations in one dimension on the other.

$$\frac{\partial V(z,t)}{\partial z} = -Ri(z,t) - L\frac{\partial i(z,t)}{\partial t} \tag{2.4}$$

$$\frac{\partial I(z,t)}{\partial z} = -Gv(z,t) - C\frac{\partial v(z,t)}{\partial t} \tag{2.5}$$

The telegrapher's equations can also be given in the frequency domain as;

$$\frac{\mathrm{d}V(z)}{\mathrm{d}z} = -(R + j\omega L)I(z) \tag{2.6}$$

$$\frac{\mathrm{d}I(z)}{\mathrm{d}z} = -(G + j\omega C)V(z) \tag{2.7}$$

Where V and I are complex valued amplitudes of voltage and current. The Eq.2.6 and 2.7 are decoupled to obtain Eq.2.8 and 2.9. While the general solution for the voltage and the current wave can be expressed in terms of a forward and a backward travelling wave as in Eq.2.10 and 2.11.

$$\frac{\mathrm{d}^2V(z)}{\mathrm{d}z^2} - \gamma^2 V(z) = 0 \tag{2.8}$$

$$\frac{\mathrm{d}^2I(z)}{\mathrm{d}z^2} - \gamma^2 I(z) = 0 \tag{2.9}$$

$$V(z) = V_o^+ e^{-\gamma z} + V_o^- e^{\gamma z} \tag{2.10}$$

$$I(z) = I_o^+ e^{-\gamma z} + I_o^- e^{\gamma z} \tag{2.11}$$

Where,

$$\gamma = \alpha + j\beta = \sqrt{(R + j\omega L) + (G + j\omega C)} \tag{2.12}$$

The propagation constant (γ) gives the attenuation and the wave number of the wave. The units of attenuation are in Np/m and that of the wave number is rad/m. However, it is more meaningful and convenient to convert the wave-number in terms of the phase velocity of the wave through Eq.2.13.

$$V_p = \frac{\omega}{\beta} \tag{2.13}$$

The characteristic impedance of the line is given by the expression;

$$Z_c = \frac{R + j\omega L}{\gamma} = \sqrt{\frac{R + j\omega L}{G + j\omega C}} \tag{2.14}$$

It reduces to $Z_c = \sqrt{L/C}$ in case the attenuation of the cable is zero, which is never the case.

It is also important to describe briefly the voltage reflection and transmission coefficients arising from mismatch in the characteristic impedance. The EM waves travelling through a line with characteristic impedance Z_c towards a load impedance Z_L undergo a partial reflection/transmission. This is described by the voltage reflection coefficient given by the ratio of the backward (V_o^-) and the forward (V_o^+) travelling wave as given in Eq.2.15 while the voltage transmission coefficient is given in Eq.2.16.

$$\tau = \frac{V_o^-}{V_o^+} = \frac{Z_L - Z_c}{Z_L + Z_c} \tag{2.15}$$

$$\Gamma = \frac{V_o^+}{V_o^-} = 1 + \tau = \frac{2Z_L}{Z_L + Z_c} \tag{2.16}$$

2.4 Cable construction

An understanding of the cable structure and materials is vital for studying partial discharges, since they entail an appreciable influence on the partial discharge pulse propagation. In the field of high voltage cable manufacturing, every cable is tailor made based on its field of application. However, for the sake of simplicity we chose a generalized and common model of a single-core cable as shown in Figure 2.2, the sections that follow use this cable model unless explicitly mentioned otherwise. As the figure represents, a power cable primarily consists of three functional layers, namely the conductor and the earth sheath which are metallic and comprise the coaxial structure of the cable and the dielectric material in between them which is dominantly capacitive in nature with a very small resistive loss (characterized by the tanδ).

From the Poynting equation (S=E $\times$ B) for power transfer it can be inferred that the power is transferred through the dielectric of the cable which has a non-zero component of Electric (E) and magnetic (B) field. Due to the large magnitude of electric field in the dielectric no inclusions, anomalies or deformities are tolerated in the dielectric, as it will lead to field distortion, which may successively and potentially cause a partial or a complete breakdown in certain cases. The conductor screen and the insulation screen shown in Figure 2.2 are semi-conductive layers. They are included to provide a smooth transition of the electric field lines and for good adhesion between the layers. These layers are employed purely based on practical requirements however their electrical behaviour is of interest when it comes to

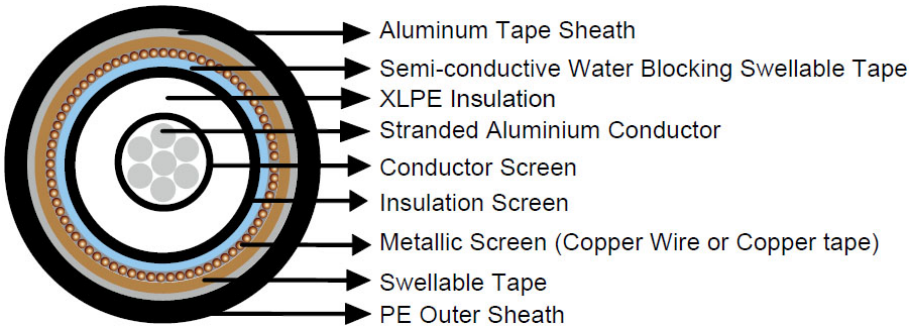

Figure 2.2: Cross-sectional view of a typical single-core cable

the propagation of the PD pulse. The influence of the layers on the attenuation characteristics of the cable at higher frequencies is very dominant and is discussed in detail in the next section. Above the insulation screen is present the swelling tape, which is also electrically a semi-conductive. In certain cases a second layer of semi-conductive water blocking tape is present to prevent water ingress during operation. They are followed by the earth sheath which could be either a stranded screen or a continuous screen or sometimes both. Not so commonly, the last layer before the protective polyethylene layer is the lead sheath. The lead sheath provides mechanical strength and increases the short circuit capacity of the cable.

2.5 Influence of semi-conductive layers

The semiconductive layer in the high voltage cables is a very peculiar meterial which is not electrically standardized, its presence is mainly for practical purposes. To have an idea of the composition of such a layer, the layer composition is listed from the Hitachi Cable US patent (US 4909960A): Ethylene based co-polymer- ethylene-vinyl acetate co-polymer, Carbon black additive (Actylene black), EPR- Ethylene Propylene Rubber, Polyethylene, 4,4-Thiobis (3-methyl-6-tertbutyl phenol), 1,3-Bis (tert-butyl peroxy isopropyl) benzyle. Therefore, it is not a pure compound like the dielectric of the cable with standard and well tested electric properties. HD Standard HD605 specifies the method for measurement of resistivity of the semi-conducting screens. However as described in [18], at higher frequencies the capacitive reactance of the cable layers is small and the resistive losses dominate. And as the resistive loss of the dielectric layer is very small, the high frequency characteristics of the cable are dictated by the performance of the semiconductor.

2.5.1 High frequency cable model

In [19][18] the high frequency cable model is presented. The semi-conductive layers are modelled as a capacitor in parallel with a resistance where the resistance represents the tanδ losses. The resistive losses of the dielectric is neglected as it is very small compared to that of the semi-conductive layer. The equivalent circuit model is shown in Figure 2.3.

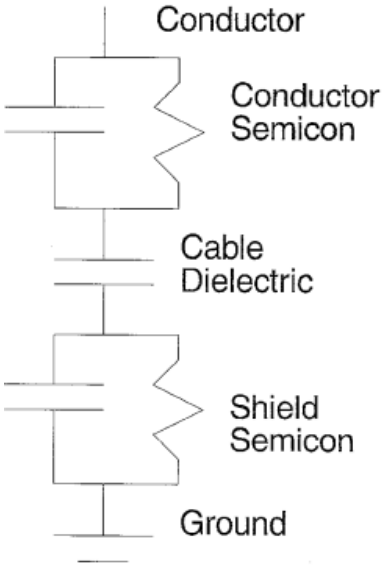

Figure 2.3: High frequency model of a shielded power cable[18]

As described in [18], attenuation is a result of the dielectric loss (tanδ) and the current propagating through the semiconducting layers, likewise the propagation constant is given by,

$$\gamma(\omega) = \sqrt{zy} = \alpha(\omega) + j\beta(\omega) \tag{2.17}$$

where z is the series impedance per metre and y is the shunt admittance per metre. The shunt admittance of each semiconducting layer is given by Eq.2.18 where the complex permittivity ϵ^* along with the geometric capacitance C_o is used to calculate the complex capacitance C^*. The real part of the complex capacitance gives the capacitive impedance of the layer while the imaginary term sums up to provide the resistive losses in the layer. Mugala et al. present an expression for the complex permittivity which is a dielectric response function fitted to the values obtained through measurements through a two Cole-Cole function, it is as given in Eq.2.19

$$y = j\omega C^*(\omega) = j\omega C_o(\epsilon^{'}(\omega) - j\epsilon^{''}(\omega)) \tag{2.18}$$

$$\epsilon(\omega) = \frac{A_1}{1 + (j\omega\tau_1)^{1-\alpha_1}} + \frac{A_2}{1 + (j\omega\tau_2)^{1-\alpha_2}} + \frac{\sigma_{dc}}{j\omega\epsilon_o} + \epsilon_\infty \tag{2.19}$$

Here, A_1 and A_2 are amplitude factors, τ_1 and τ_2 are relaxation times, α_1 and α_2 describe the width of the relaxation peaks, σ_{dc} is the DC conductivity and ϵ_∞ is the high frequency component of the relative permittivity.

$$z = \frac{1}{2\pi r_i}\sqrt{\frac{j\omega\mu_o}{\sigma_{cond}}} + \frac{j\omega\mu_o}{2\pi} ln\frac{r_o}{r_i} + \frac{1}{2\pi r_o}\sqrt{\frac{j\omega\mu_o}{\sigma_{screen}}} \tag{2.20}$$

The series impedance of the cable insulation is calculated using Eq. 2.20, where r_i and r_o are the radius of the inner conductor and the outer screen.

Table 2.1: Parameters of the cable used in the MATLAB Simulation

	Cable 1	**Cable 2**
Conductor radius (r_c)	8.85 mm	19.5 mm
Thickness of conductor screen (t_{cs})	0.45 mm	1.2 mm
Outer radius of insulation (r_i)	13 mm	36.1 mm
Thickness of insulation screen (t_{is})	1 mm	1 mm
Thickness of outer semicon-bed (th_{sb})	0.5 mm	0.5 mm
Inner radius of earth screen (r_s)	14.5 mm	37.6 mm
Thickness of earth screen (th_s)	1 mm	1 mm
Relative permittivity of insulation (ϵ_r^*)	2.3+0.001i	2.3+0.001i
Electrical conductivity of the conductor (σ_c)	$3.7e^7$ S/m	$3.7e^7$ S/m

2.5.2 Validation of the high frequency model

The attenuation of a 11 kV cable is modelled in MATLAB as presented in the previous section and compared with the measured values of propagation constant available in DNV GL's database (also known as KEMA database). The geometric specifications of the cables used are given in Table 2.1. Cable 1 is rated 11 kV, 300 mm^2 and cable 2, 150 kV, 1200 mm^2. The values of propagation constant obtained using the model presented by Mugala et al. conform with the measured values obtained from DNV GL's database. However, the measured values are reliable only up to 30 MHz and the limits of the estimated complex permittivity is between 30 kHz and 500 MHz and hence the deviation below 30 kHz and above 30 MHz is ignored.

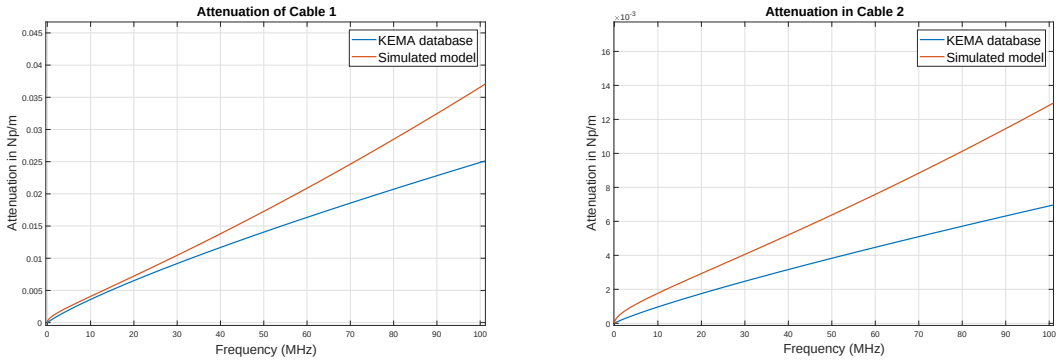

(a) Cable 1 (b) Cable 2

Figure 2.4: Measured and estimated attenuation of cables 1 and 2

The cable attenuation which is given by the real part of the propagation constant is given in Figure 2.4, and instead of presenting the results of the phase constant directly, the propagation velocity derived through Eq.2.13 is presented in Figure 2.5. Alternatively the propagation velocity can be roughly estimated by the expression $c/\sqrt{\epsilon_r}$. The estimated values of the complex cable permittivity for the semi-conductive layers is presented in Figure 2.6.

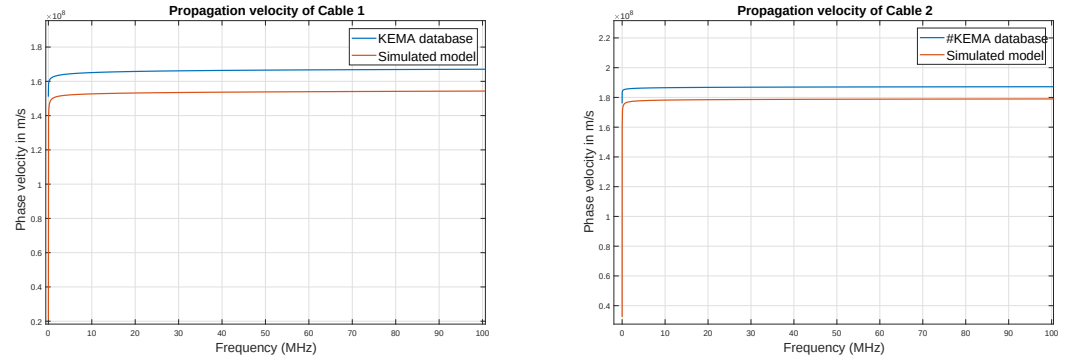

(a) Cable 1 (b) Cable 2

Figure 2.5: Measured and estimated propagation velocities of cables 1 and 2

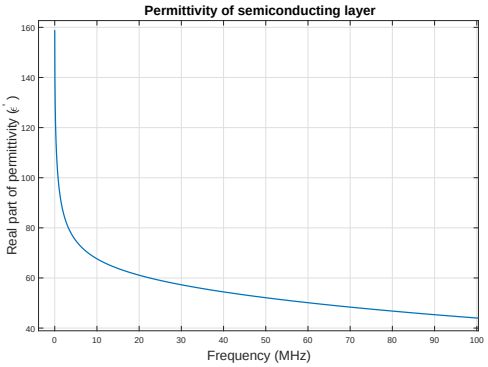

(a) Real part of permittivity

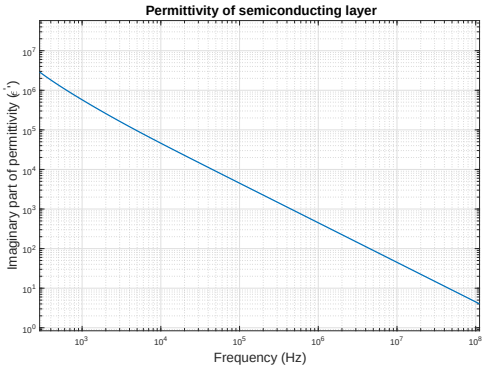

(b) Imaginary part of permittivity

Figure 2.6: Real and imaginary part of the complex permittivity of the semiconductive layers used in the simulation

2.6 Conclusion

The model for cable attenuation presented in [13] is validated against the measured values from DNV GL's database in the frequency range upto 30 MHz. The results of this section are utilized in the analysis and modelling phase of the project presented in Chapter 4 and 5.

CHAPTER

3

FEASIBILITY STUDY ON PD MEASUREMENT TECHNIQUES

3.1 Introduction

This chapter makes a comprehensive evaluation of all the possible techniques for measuring partial discharges in cable systems. The research follows a distinctive pattern in which it explores several techniques to measure a PD through the various physical phenomenon associated with it. Based on rational and logical reasoning and taking leads from literature, the techniques are marked as either applicable or not applicable. The fundamental changes that occur due to a partial discharge are as listed below:

- Charge redistribution leading to a small voltage pulse and an associated current pulse in the nanosecond range leading to travelling waves in the coaxial cable.
- Electromagnetic radiation due to the charge acceleration
- A small explosion leading to a short acoustic pulse characterized by pressure variations

- Irradiated light
- Heat radiation
- Chemical degradation producing by-products (residual gases) and
- Ionizing radiations

Continuous, on-line measurement of partial discharges in cables based on the pressure variations, irradiated light, heat, gases and ionizing radiations was investigated and it was concluded that it was practically not feasible due to the drastic damping of acoustic pulses and the extremely small percentage of energy that is converted to these alternative forms (heat, light and radiation). Which in-turn will yield a very poor sensitivity of the measurement system.

The branching diagram with all potential techniques/ideas is given in Figure 3.1, this is an exhaustive list and out of these the most practical ideas are presented as a consolidated list and their brief evaluation is presented at the end of this chapter in Table 3.5. The next sections present some of the simulation results for the techniques that were categorized as feasible preliminarily.

3.2 Simulations and estimations of potential techniques

The possibility of physically altering the earth screen of a cable in order to manipulate the magnetic field lines arising from the PD such that they can be picked up using an inductive sensor applied over the cable came across as an appealing technique to measure PDs. Two such possibilities that were investigated during the course of the project are presented in Sections 3.2.1 and 3.2.2. Meanwhile, the concept of antennas for radiation and reception of EM fields indicated a suitability towards this application (Table3.5). Hence, the simulation results on two different antenna models are discussed in Section 3.2.3.

3.2.1 Helical wire strip below the earth sheath

The inclusion of a helical wire below the earth screen creates the possibility for the PD current to follow a helical path and thereby give rise to a parallel component (with respect to the cable axis) of magnetic field which will in turn allow the application of an wire loop over the helical layer to sense the discharge. This technique has been used in the past as a method to detect discharges in medium voltage cables

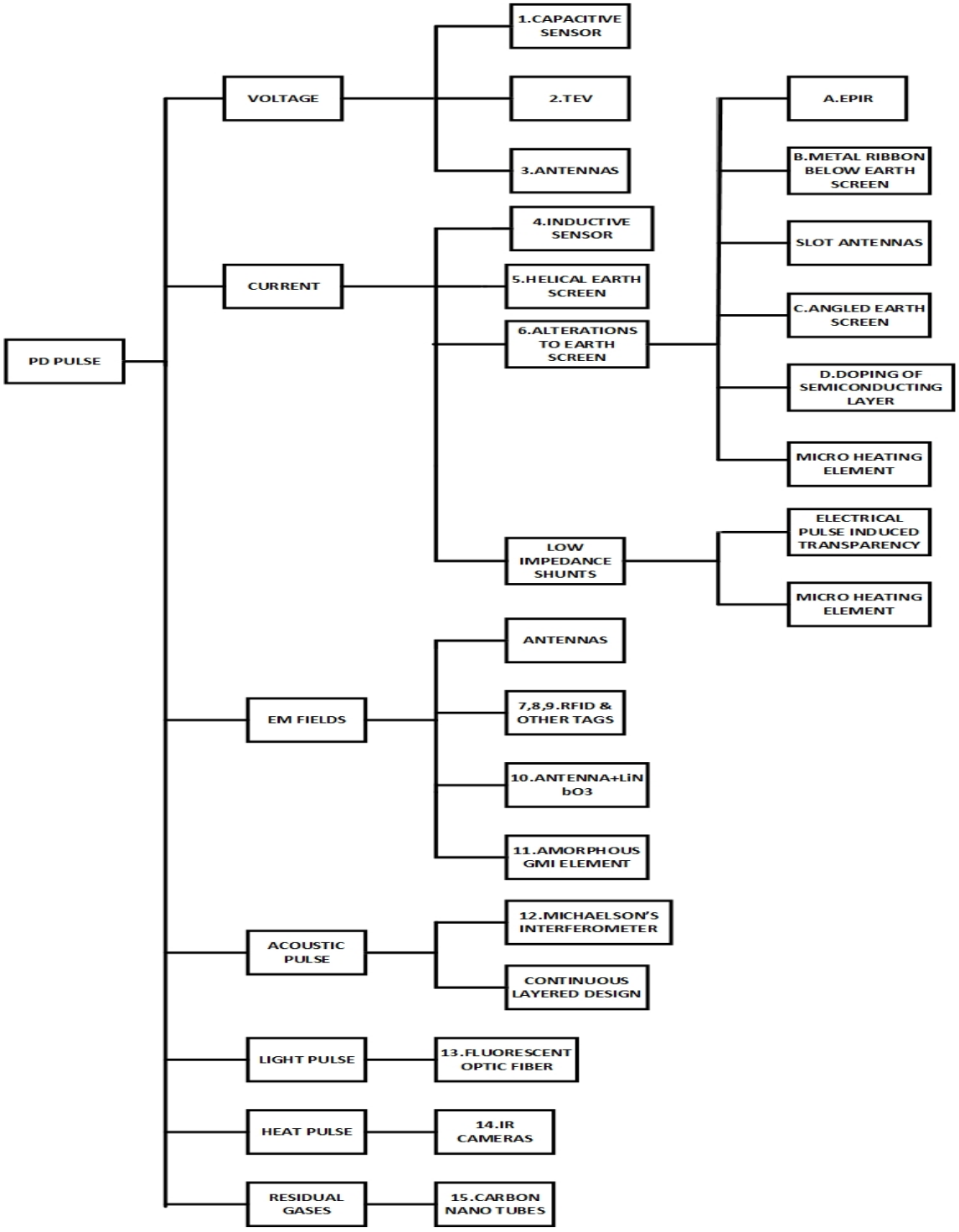

Figure 3.1: List of methods investigated during the feasibility study

with a single, helical screen [20]. However, it was not possible to implement this for cables with lead screens due to the high skin effect. Therefore, a simulation is performed to check the possibility of including a short section of (additional) helical screen and a wire loop below the original earth sheath/lead sheath. The model for the simulation was built using the Solidworks software and imported into COMSOL Multiphysics, it is as shown in Figure 3.2. As can be seen from Figure 3.2, the helical wire is made flat in order to have greater radial area so that more current is induced against the current induced over the earth screen. And the flat section of the wire is also expected to reduce the skin effect. The dimension of the helical wire is $3 \times 0.5\,mm$.

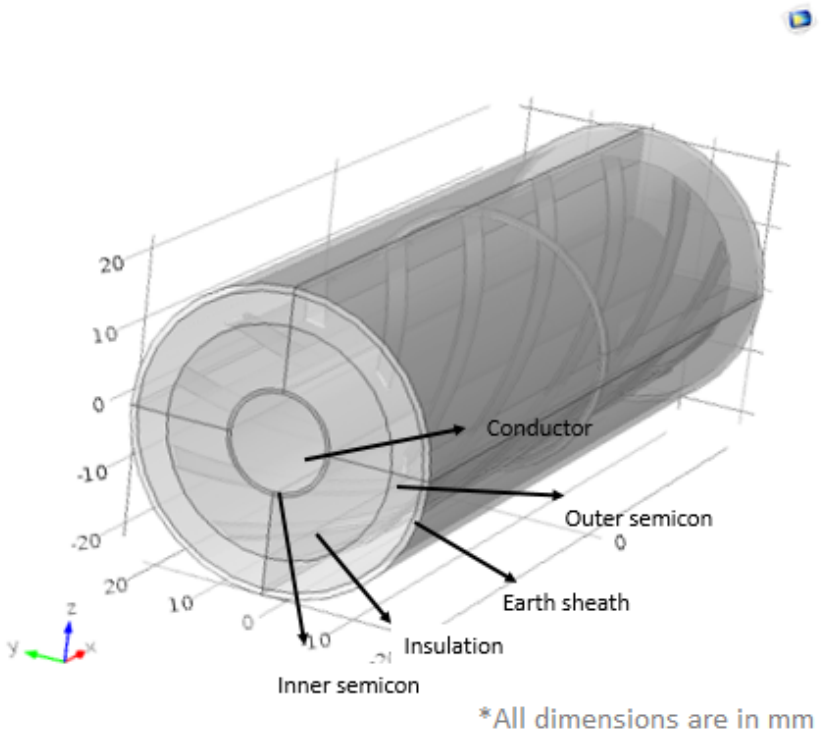

Figure 3.2: COMSOL model of the helical wire included below the earth screen of the coaxial cable

Th characteristic impedance of the cable section is assigned at the 'Zc' field under electromagnetic module using the expression;

$$Z_{ref} = \frac{Zo_{const}}{2\pi\sqrt{\epsilon_r}} log\frac{r_o}{r_i} \tag{3.1}$$

where Zo_{const} is the default impedance of the port internally assigned by COMSOL

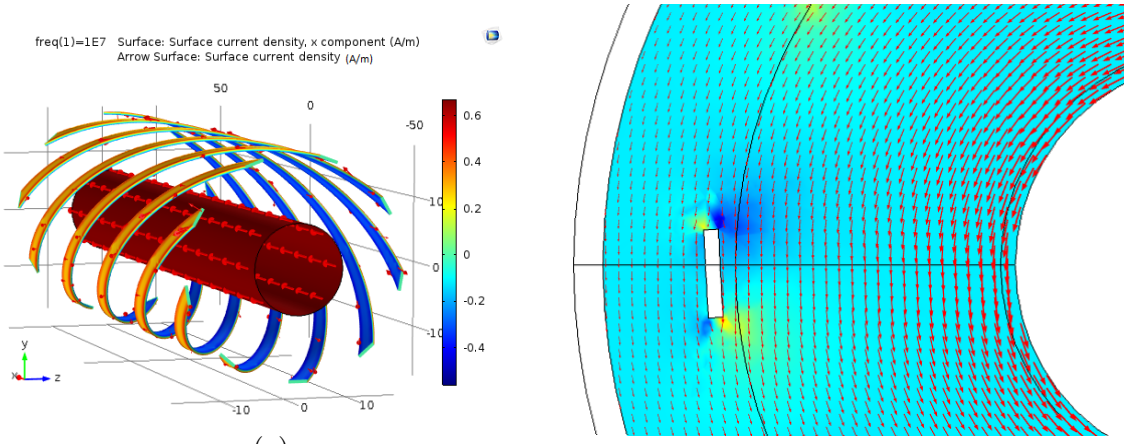

(a) (b)

Figure 3.3: Results of the COMSOL simulation (a) plot of surface current density (in A/m) showing extreme skin effect over the conductive surfaces and (b) the magnetic field lines in the cable section

(50Ω), ϵ_r is the relative permittivity of the cable dielectric, r_o is the outer radius of the cable earth screen and r_i is the radius of the inner conductor.

A wave excitation of 1 V is assigned over the insulation of one cable end using the 'Lumped port 1' feature available in the physics module. The other cable end is assigned to 'Lumped port 2' with no wave excitation. The model is solved through a frequency study at 10 MHz. The need to solve the model using a PD like pulse (wide frequency) was discounted over a constant frequency study because the goal of the simulation was to look at the orientation/distribution of the currents and fields in the model, the implementation of a PD like pulse would mean that a time dependent study will be required. And a time dependent study in COMSOL for a 3D model requires high computation time.

The results of the COMSOL study are shown in Figure 3.3 and 3.4, Figure 3.3a shows the surface current distribution over the conductor and the helical wire, in this case the earth sheath has been made invisible for proper visualization. It can be seen that there is extreme skin effect over the helical wire strip and a similar effect is observed on the earth sheath. The skin depth at 10 MHz for aluminium is 30 μm and hence the idea of including a helical wire below the earth screen is futile. In addition, there is absolutely no field outside the earth sheath due to the presence of these compensating skin currents. Figure 3.3b shows the magnetic field distribution in a radial section of the cable, the bending of the field lines along the metallic boundaries of the helical wires can be observed. The current distribution over the metallic loop/ring around the helix is shown in Figure 3.4. The random distribution

Table 3.1: Current distribution in various layers obtained from COMSOL simulation of the helix model

	Surface current along x-axis Jsx
Current through conductor	15.7 mA
Current through earth screen	-14.7 mA
Current through helix (net.)	-0.3 mA
	Normal component of surface current
Current through metallic loop	0.3 mA

can be explained by the coarse mesh and the fact that there is practically no current through the loop as the net current in the helix is as low as 0.3 mA.

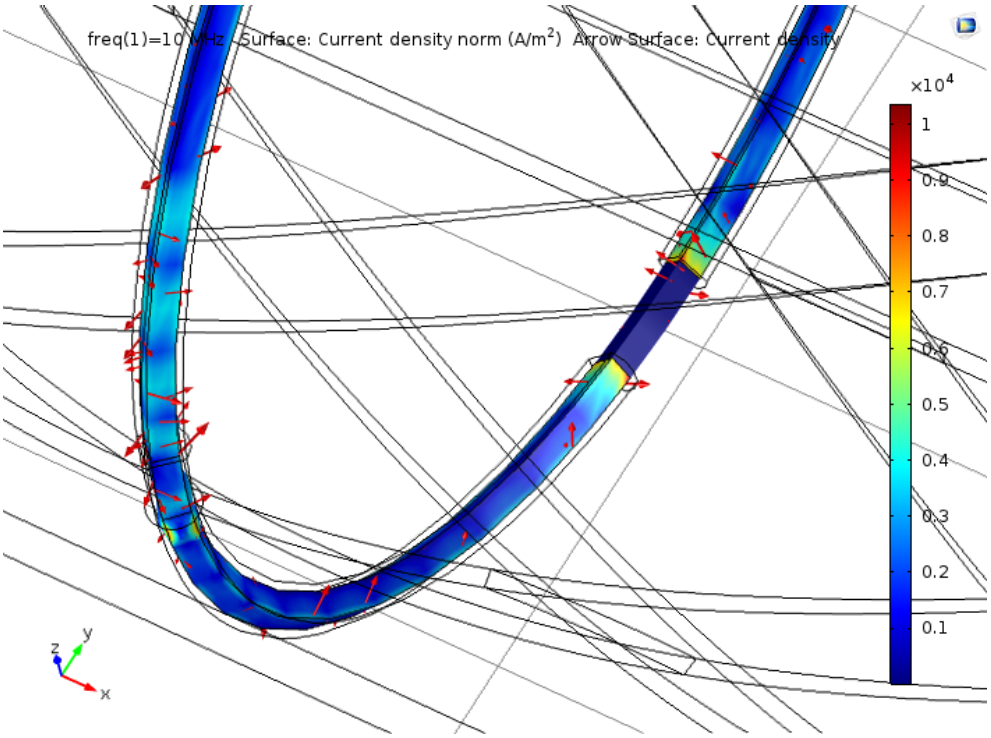

Figure 3.4: Current density (in A/m^2) in the metallic loop around the helical wire

Conclusion

Table 3.1 concludes the results of the simulation. The absence of field outside the solid screen ruled out the possibility of employing an inductive core from the outside of the cable however the possibility of inclusion of a small metallic loop below the

earth screen was investigated to no avail. This method also requires an additional spaces (>4mm) under the earth sheath for the inclusion of the helix and the wire loop, this is not possible from a practical standpoint. Therefore, this alternative will not be explored further.

3.2.2 Slot antennas

The alternative of implementing slot antennas, which can otherwise be described as slits on the earth sheath of the cable was explored as a method to enable the coupling of an inductive sensor coil from the outside of the cable with least damage to the integrity of the cable structure.

Slot antennas are cut out of a metallic wave guide which is the coaxial cable in this case. They radiate maximum power at a resonant frequency and this is exploited in radar systems for communication. The model of the cable earth sheath with slits of 1 mm thickness was built using Solidworks software and imported to COMSOL. The two slits are made with different lengths in order to study the effect of slit size on frequency. In COMSOL the other cable layers were added and the simulation was executed using a frequency study at 1,10,100 and 1000 MHz. Figure 3.5 shows the COMSOL geometry that was used in the simulation.

The magnetic field pattern of the cable model is shown through Figure 3.6a and 3.6b. The magnetic field radiating out of the slits on the earth sheath of the cable can be seen in Figure 3.6b. Using a boundary probe over the area of the slits the flux output is calculated through intergrating the normal component of magnetic flux density (B). The magnetic flux output is calculated using the expression;

$$\phi = \frac{B}{A} \Rightarrow \phi = \iint B.ds \tag{3.2}$$

By Faraday's law,

$$emf = -N.\frac{d\phi}{dt} \tag{3.3}$$

The values of the magnetic flux at various frequencies for the two slits are given in Table 3.2. By substitution in Eq.3.3 the maximum voltage output when an inductive sensor coil is employed is calculated and listed in the same table. The values clearly increase with frequency and size of slit. However, the simulation is a steady state

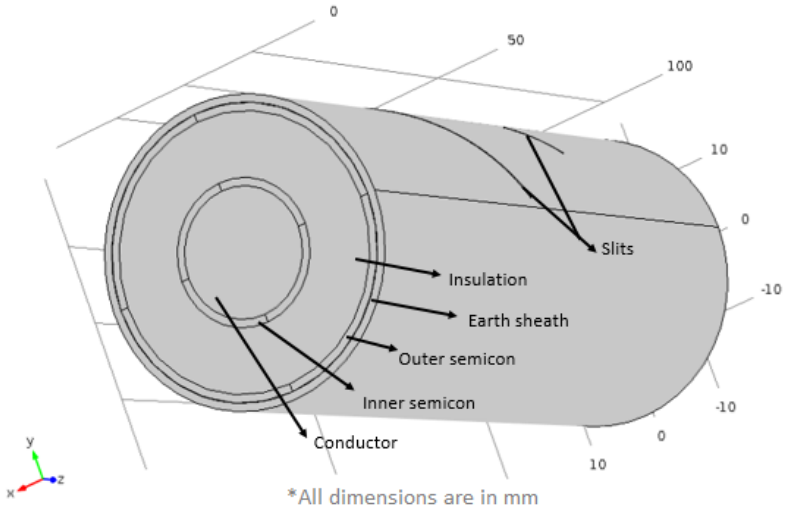

Figure 3.5: COMSOL geometry of the Coaxial cable with slot antennas on its earth sheath

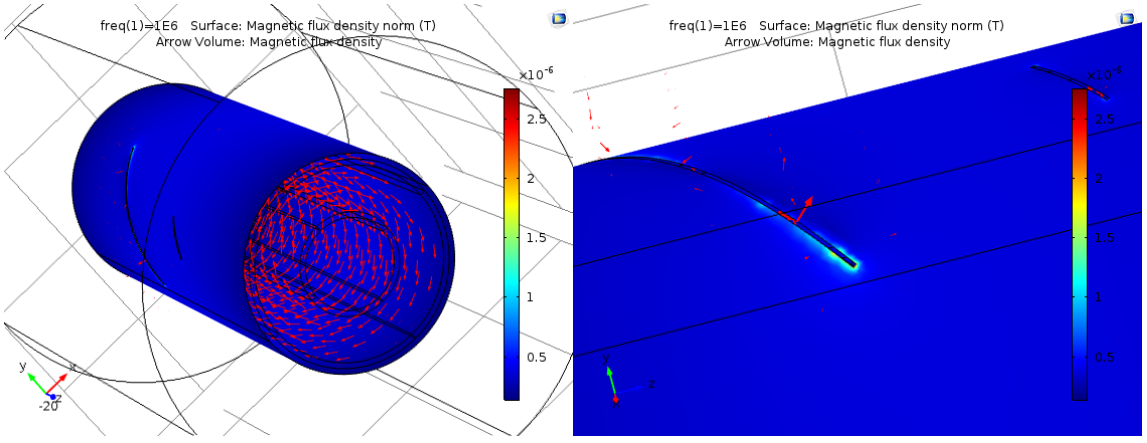

(a) (b)

Figure 3.6: Results of the COMSOL simulation with slits on the cable earth sheath,(a) shows the magnetic field lines inside the cable structure and (b) shows the magnetic field radiating out of the slits

frequency study and does not represent the actual partial discharge case where the input pulse is a wideband frequency pulse. Thus the transfer function will be much different in that case but the details are inconsequential for this initial investigation.

Table 3.2: COMSOL Results of Flux output and maximum emf using the slot antennas

Frequencies	**Big slit**		**Small slit**	
	Flux (Wb)	**emf (V)**	**Flux(Wb)**	**emf(V)**
1MHz	5.45E-12	5.45E-6	6.43E-13	6.43E-7
10MHz	6.44E-12	6.44E-5	7.44E-13	7.44E-6
100MHz	6.54E-12	6.54E-4	7.82E-13	7.82E-5
1000MHz	3.17E-11	3.17E-2	1.75E-12	1.75E-3

Conclusion

After careful consideration it was concluded that this alternative is unattainable since cable manufacturing is governed by strict regulations and it will not be allowed to create any deliberate breaches on the outer sheath of the cable as this will compromise the robustness of the structure. Hence, this alternative was decided not to be explored further.

3.2.3 Antennas in cable

This section investigates the application of antennas as transceivers in cables when placed below the earth screen (above the extruded insulation screen). There are two important tasks that are performed on the antenna design.

1. Finding the resonant frequency of the given antenna model
2. Finding the coupling coefficient from the antenna to the coaxial cable and vice versa

Dipole antenna model

The first cycle of simulations were performed with the most simple antenna configuration, the dipole antenna. The antenna was designed with dimensions based on Eq.3.4 to 3.7 [21]. The dimensions of the antenna were decided based on the substrate the antenna was subjected to be placed in. Since in this case, the antenna

is located just below the earth sheath and above the extruded semiconducting layer, the value of effective dielectric constant is calculated considering the dielectric constant of the cable insulation and the extruded semiconducting layer. The dielectric permittivity of the semiconducting layer was modelled in COMSOL using the analytical equation presented in Section 2.5.1, to be frequency dependant and the same is shown in Figure 3.7

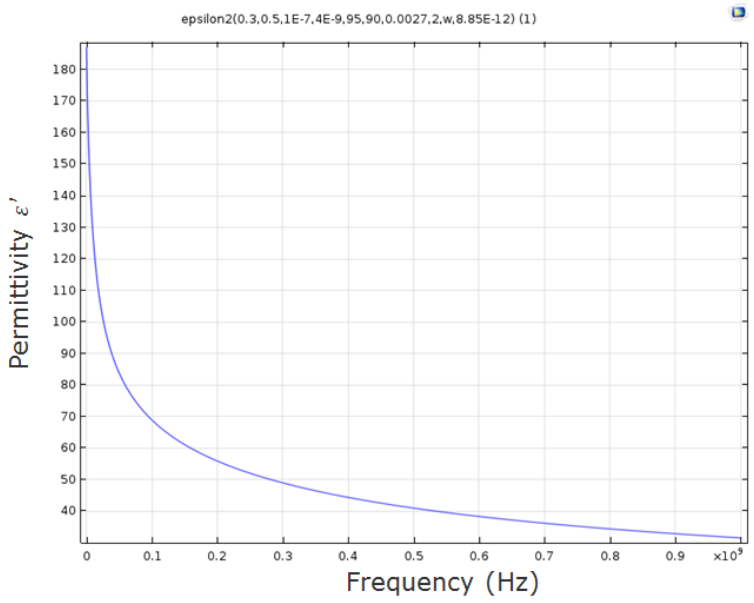

Figure 3.7: Dielectric permittivity of the semiconducting layer implemented in COMSOL

Antenna dimensions

$$wavelength\,(\lambda) = \frac{C_0}{f\sqrt{\epsilon_r}} \tag{3.4}$$

$$arm\,length = \frac{\lambda}{4} \tag{3.5}$$

$$radius\,of\,dipole = \frac{armlength}{20} \tag{3.6}$$

$$gap\,size = \frac{armlength}{100} \tag{3.7}$$

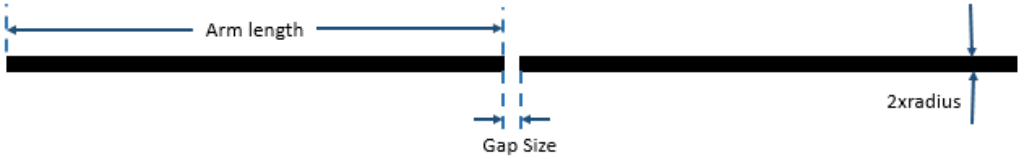

Figure 3.8: Dimensions of the dipole antenna

In COMSOL the electromagnetic wave module was used to model the antenna and it's associated boundary conditions. While the transmission line module was applied to the coaxial cable to obtain the transmission line parameters. The electromagnetic wave module in COMSOL solves for the electric and magnetic fields through Eq.3.8[22];

$$\bigtriangledown \times \mu_r^-1(\bigtriangledown \times E) - k_0^2(\epsilon_r - \frac{j\sigma}{\omega\epsilon_0}) = 0 \tag{3.8}$$

where, $k_0 = \omega\sqrt{\epsilon_o\mu_o}$. The first term solves for the magnetic field through the Maxwell-Faraday's law and the second term solves for the electric field through the equation for current continuity $J = \sigma E$ and the displacement field D.

The transmission line module solves for the transmission line parameters through the generic Eq.3.9;

$$\frac{\partial}{\partial x}(\frac{1}{R + j\omega L}\frac{\partial V}{\partial x}) - (G + j\omega C)V = 0 \tag{3.9}$$

A user defined lumped port of specific dimensions of the gap area was set-up at the antenna feed point (gap) and assigned an input voltage of 1 V in case of the antenna being tested as a transmitter. Since there was no information on the impedance of the antenna in this configuration, a partial reflection of the power was expected. However, after one trial run, COMSOL calculates the impedance of the port in the specific configuration and hence this value can be fed back to the antenna port to facilitate sufficient conjugate matching. Alternatively, when modelling it as a receiver, no field excitation is assigned at the antenna feed while a 1 V wave

excitation is provided at the cable end (assigned as lumped port). The coaxial cable was modelled as in earlier simulations with all cable layers while the cable ends were assigned with the value of characteristic impedance to prevent wave reflection from impedance mismatch. Reflections are undesirable since they may lead to constructive or destructive interference in the set-up leading to errors. The impedance matching can be accomplished in COMSOL by assigning the expression in Eq.3.1 to the Z_{ref} field under lumped ports.

Firstly, an eigenfrequency study was performed on the model to obtain the resonant frequency of the transceiver which resulted at 198 MHz. This is very close to the actual resonant frequency that the antenna was modelled for, namely 200 MHz. This was done in order to check the deviation of the resonant frequency inside the coaxial structure from that in air.

The final simulation was built on COMSOL with a 3 m long cable and 2 dipoles on either end, the configuration was tested with one dipole assigned as a transmitter and the other as the receiver. Strangely enough, a travelling wave along the coaxial cable wave guide was observed. This can be seen in Figure 3.9, it shows the electric and magnetic field distribution of the travelling wave over the coaxial cable.

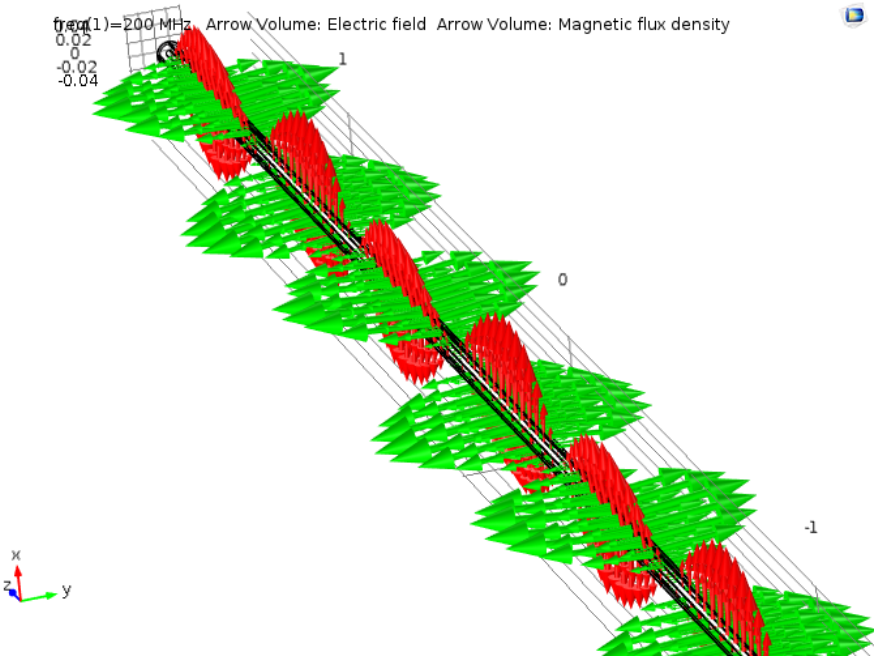

Figure 3.9: The 3-dimensional field distribution of the wave propagating along the cable as a result of the radiating dipole antenna. The electric field in V/m given by red arrows and the magnetic field in Tesla given by green arrows.

The results of the simulation are tabulated in Table 3.3. A rough estimate of the coupling between the antenna and the coaxial cable can be derived by taking the ratio of the voltages at different ports, which in this case is 4.6-6.1%. The poor performance of the dipole antenna is because the TEM waves of the cable are cross-polarized with respect to the antenna, in other words, the angle between the electric field lines of the cable and those of the radiating antenna is 90°. Figure 3.10a shows the electric field distribution around the dipole antenna when placed in air and Figure 3.10b shows the electric field pattern when placed inside a coaxial wave guide. It is observed here that the field lines are re-oriented in a specific way in order to obey the laws of electrostatics.

Table 3.3: Voltage on various ports from the COMSOL simulation of dipole antenna

	Voltage (mV)	**Port impedance (Ω)**
Radiating antenna	$1300\angle -49°$	$43\angle -90°$
Receiving antenna	$3.5\angle -43°$	$50\angle 0°$
Cable end 1 (close to radiating antenna)	$59.9\angle 126°$	$45\angle 180$
Cable end 2 (close to receiving antenna)	$58.0\angle 66°$	$48\angle 180$

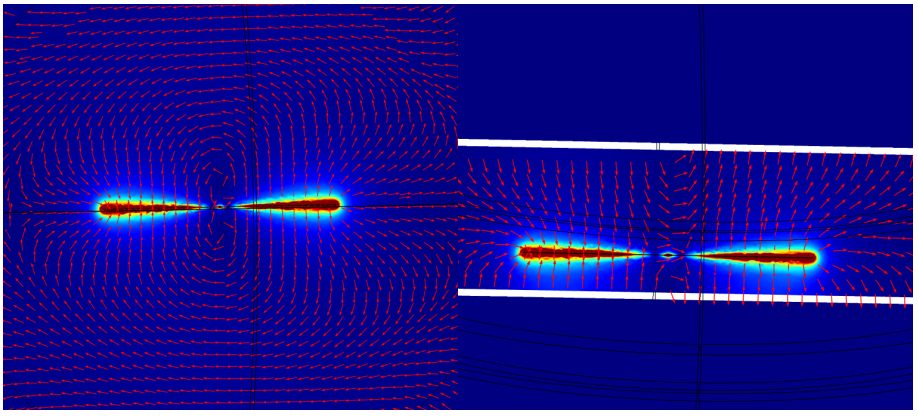

(a) In air (b) In coaxial wave guide

Figure 3.10: Results of the COMSOL simulation showing the electric field lines around a dipole when (a) placed in air and (b) placed inside a coaxial wave guide

Nevertheless, ignoring the dismal performance of the antenna design, this already provides sufficient proof of concept for the application of antennas inside power cables. It is a question of how efficiently the system can accomplish the task and what is considered as 'good performance'.

Conclusion

It has been observed that though the antenna resonates inside the coaxial cable only a very small fraction of the energy couples back and forth between the antenna and the cable. This is because the antenna is cross polarized with respect to the TEM wave in the cable. Hence a more suitable antenna configuration which is the patch antenna is explored in the next section.

Patch antenna model

The model of the patch antenna is built in Solidworks software with a metal patch of dimension 45x45 mm mounted over a substrate of 63x70x1 mm. The dimensions were derived from the book of Balanis on Antenna Theory [21]. The model can be seen in figure 3.11.

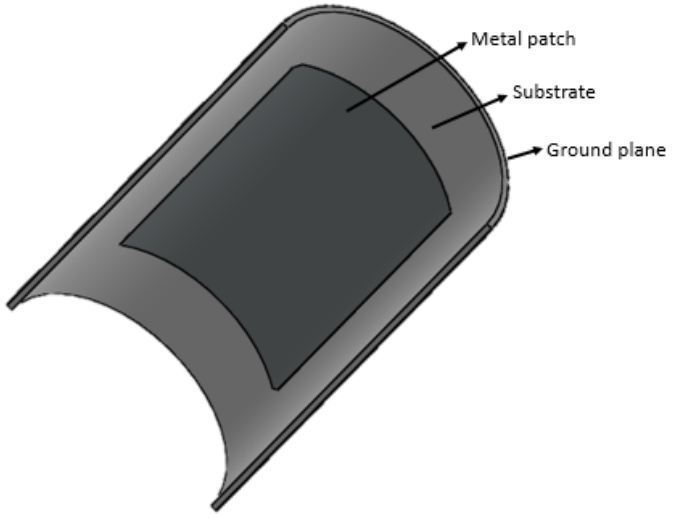

Figure 3.11: Model of the patch antenna built using Solidworks software package

Antenna dimensions

$$W = \frac{C_o}{2f_r}\sqrt{\frac{2}{\epsilon_r + 1}} \tag{3.10}$$

$$\epsilon_{reff} = \frac{\epsilon_r + 1}{2} + \frac{\epsilon_r - 1}{2}[1 + 12\frac{h}{W}]^{-1/2}, \frac{W}{h} > 1 \tag{3.11}$$

$$\frac{\triangle L}{h} = \frac{0.412(\epsilon_{reff} + 0.3)(\frac{W}{h} + 0.264)}{(\epsilon_{reff} - 0.258)(\frac{W}{h} + 0.8)} \tag{3.12}$$

$$L = \frac{c_0}{2f_r\sqrt{\epsilon_{reff}}} = -2\triangle L \tag{3.13}$$

An initial simulation was performed to obtain the resonant frequency of the antenna design using the eigenfrequency solver available in COMSOL. The results of the simulation showed that the antenna resonates at the frequencies: 2.7, 4.2, 5.1 and 5.2 GHz, but these frequencies are unfit for the specific application. Therefore, the frequency of operation was required to be scaled down below 50 MHz for its successful functioning. However, based on the Eq.3.10 to 3.13, the dimensions of such an antenna should be close to $2 \times 2\,m$. This is impossible to implement in reality as the width of the antenna structure is limited by the circumference of the cable. However, it was checked on COMSOL to obtain the exact resonant frequency of an alternative design with $2\,m \times 5\,cm$ dimensions. Through the simulation it was deduced that the design has sub-resonant peaks at: 41, 43.6, 51, 61.5 and 71 MHz. The associated far field radiation pattern of this design is shown in Figure 3.12. This could be a possible alternative to the dipole antenna.

Subsequently, simulation is performed on the patch antenna design with dimensions 45×45 mm in order to obtain the coupling coefficient of the antenna configuration inside the coaxial wave guide. The resultant field pattern that arises from the radiating patch antenna can be seen in Figure 3.13 and the results are tabulated in Table 3.4. The coupling coefficient from the patch antenna to the cable is about 13.5-15%, which is much higher than the coupling coefficient of the dipole configuration. This is because the patch antenna is co-polarized with the TEM waves of the coaxial cable. In other words, the angle between the electric field lines of the cable and those of the radiating antenna is 0°.

Table 3.4: Voltage on various ports from the COMSOL simulation of patch antenna

	Voltage(mV)	**Port impedance (Ω)**
Antenna port	305∠81.8°	14.8∠45.8°
Cable port 1	45.7∠111.4°	47.5∠179°
Cable port 2	41.4∠62°	47.4∠179°

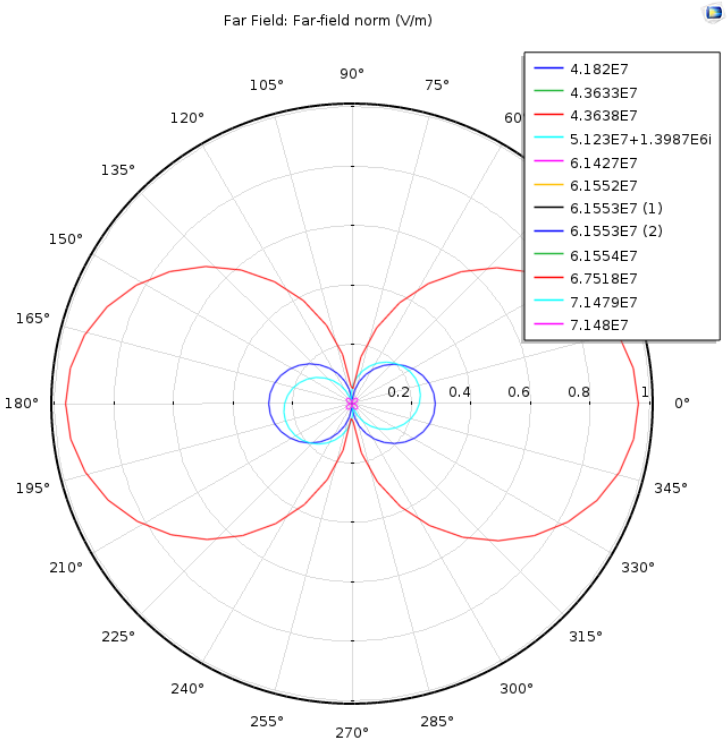

Figure 3.12: The far field radiation pattern of the patch antenna structure obtained through COMSOL eigenfrequency study

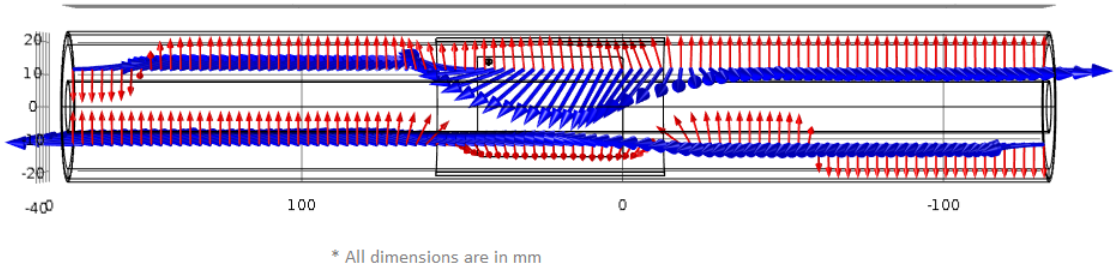

Figure 3.13: The field distribution of the propagating wave along the coaxial cable arising from the radiating patch antenna. The electric field in V/m given by the red arrows and the magnetic field in Tesla given by the blue arrows.

Conclusion

In both cases, the dipole antenna and the patch antenna, it can be inferred that it is quite strange for the antennas to function as it does, inside a coaxial cable structure. The reason for its successful functioning is the fact that the wave guide being a perfect electric conductor acts as a channel to alter the field pattern and make the electric fields orthogonal to the wave guide and the electric and magnetic fields orthogonal to each other like in the case of a TEM wave. This makes it favourable for the antenna like transceivers to function inside the coaxial cable. Additionally, the dipole antenna is able to be modelled suitably to resonate at the lower frequencies of interest while the patch antenna is not. This leads to a compromise between an ill-functioning resonant dipole or a sub-optimal patch antenna (functioning outside the resonant frequency band).

3.3 Other potential methods

There has been a spike in research of electro-optic applications in partial discharge monitoring. The main reason being their immunity towards electromagnetic interference. The following sections investigates the trends and possibilities available towards their application in power cables.

3.3.1 Electro-optic modulators for PD sensing

Though there are several electro-optic based applications for the detection of partial discharges. Only a limited number of these systems are completely capable to fulfil the objective when it comes to power cables. [15] is one such article that demonstrates the use of optical transducer to measure the acoustic emissions from a PD at locations of joints or in GIS. In order to explore the potential in the field of electro-optics, several papers were reviewed [23][24][25][26]. Most of them used the Pockel's effect, Kerr effect or acoustic means to measure sensitive electric fields.

The literature review on techniques to measure sensitive electric fields yielded a seemingly suitable method that was adaptable for the application in power cables. Its suitability was decided based on the small size of the sensor and highly sensitive electric field measurement capability. The novel method is called guided resonances on lithium niobate for extremely small electric field detection and is presented in [27] and [28]. It is based on coherence modulation of light using Lithium Niobate crystals ($LiNbO_3$). Electrical signals are imprinted on light as a sequence of optical delays

greater than the coherence time of the optical source. The lithium niobate crystals are used as electro-optic retarders to introduce optical delays. The additional use of a bowtie antenna in [28] is to provide electric field enhancement. A maximum sensitivity of $50\,\mu V/m$ can be achieved with such a system. This would mean that, the inclusion of this sensor in the outer semiconducting screen will allow the detection of partial discharges. This is because the semiconducting layer serves as an apparent ground in case of the 50 Hz voltage but not at the high frequencies associated with PDs. Figure 3.14 briefly sums up the process of guided resonance in Lithium Niobate.

Incidentally, the sensitivity is in the order of the fields associated with a PD. But regrettably this idea cannot be pursued since the technology is expensive and still under development. Hence, this is listed as a potential idea for future research.

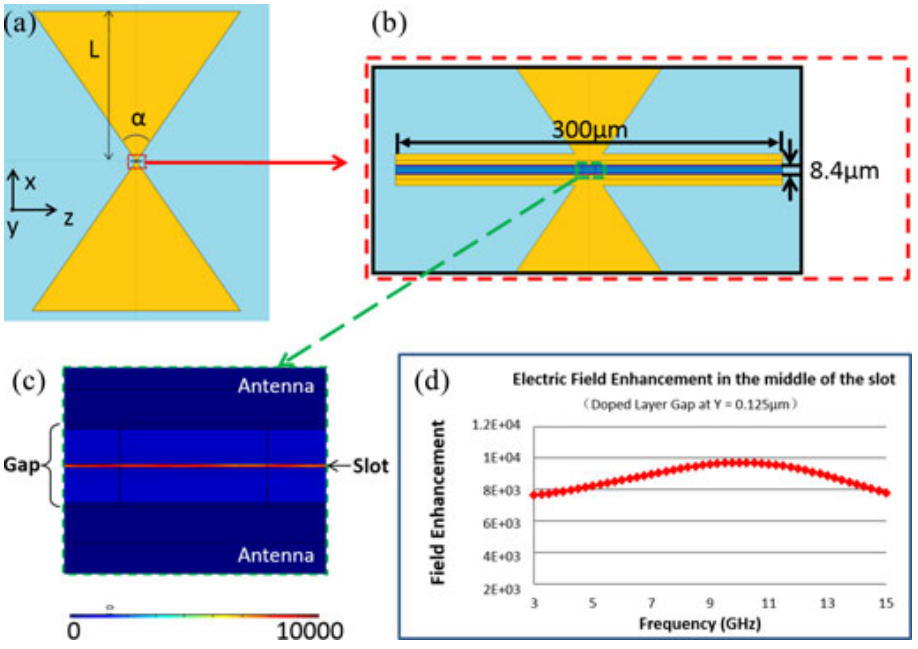

Figure 3.14: Novel method of electric field measurement by guided resonance in Lithium Niobate crystals [28] (a) Schematic top view of the bowtie antenna.(b) Magnified image of the feed gap region in (a). (c) Top view of electric field enhancement distribution inside the feed gap of the antenna. (d) Variation of the field enhancement factor inside the slot versus incident RF frequency.

Table 3.5: Outcomes of feasibility study

Measurement Unit	Methods		Merits	Demerits	Final Comment
VOLTAGE	1	Capacitive sensor [29]	Proven technology	Challenge of max.range remains Not suitable to existing cables	APPLICABLE
	2	TEV sensor[30]	Proven technology	No TEV in 'ideal' coaxial cables	NOT APPLICABLE
	3	Antenna as receiver	Wide range of poosibilities	Challenge of tuning inside cable	APPLICABLE
CURRENT	4	Inductive sensor[31]	Proven technology Suitable for existing cables	Need to separate earth screen from conductor to allow sensing Challenge of range remains	APPLICABLE
	5	Helical earth screen	Simple construction/setup	Limited application Not suitable for cables with Lead screen	NOT APPLICABLE

Measurement Unit	Methods			Merits	Demerits	Final Comment
CURRENT	6	Physical alterations to earth screen for tuning of magnetic fields				
		A	EPIR materials [32]	Reversible effect Sufficiency of thin layer	High threshold voltage for phase reversal	NOT ALPPLICABLE
		B	Additional helical ribbon in semicon	Functions theoretically	Increased skin effects in practice Requires tedious manufacturing	NOT APPLICABLE
		C	Angled earth screen with semicircular lumps	Functions theoretically	Practical problems in cable laying due to lumps in cable	NOT APPLICABLE
		D	Doping of semicon layer	Functions theoretically	Impractical to perform doping on the extruded cable material	NOT APPLICABLE, FUTURISTIC
EM FIELD	7		Passive harmonic tags	Easy and cheap	Works only at resonant frequency Insufficient range	NOT APPLICABLE
	8		RFID tags [33]	Cheap and effective Small power requirements	Challenge of tailoring a special design for PD application	APPLICABLE
	9		Acousto-magnetic tags	Cheap and effective	Requires large bias magnetic field	NOT APPLICABLE

Measurement Unit	Methods		Merits	Demerits	Final Comment
E-FIELD	10	Lithium Niobate optical transducer[28]	Sensitive detection range (μV/m)	Expensive, new technology	NOT APPLICABLE, FUTURISTIC
B-FIELD	11	Giant magneto-impedance sensitive element[34]	small size and sufficient range	Requirement for a reference acoustic signal	NOT APPLICABLE
ACOUSTIC PULSE	12	Michaelson's interferometer	Free from electromagnetic interference	Large size and increased attenuation with distance	NOT APPLICABLE
LIGHT	13	Fluorescent optic fibers	Proven technology in GIS etc	Inapplicable to cable systems	NOT APPLICABLE
THERMAL	14	Infrared cameras	Used in substations	Inapplicable to cable systems	NOT APPLICABLE
RESIDUAL GASES	15	Carbon Nano Tubes (CNT)	Proven technology used in GIS etc.	Inapplicable to cable systems	NOT APPLICABLE

3.4 Conclusion

Combining the results of Table 3.5 and the COMSOL simulations it is evident that the potential PD sensing techniques are the well-established methods namely the capacitive and inductive sensors. With that said, the other seemingly positive area is the field of antennas. The positive results obtained in the simulations employing antennas as transceivers guides the research in the direction of distributed sensor technology which communicate by means of transceivers. Moreover, during the course of research, RFID tags which are cheap and widely used at present came across as a befitting idea which can combine the functions of sensing and communication. This idea is explained in greater detail in Chapter 4.

CHAPTER

4

RFID INSPIRED SENSOR

4.1 Introduction

From the feasibility study it was lucid that the communication between sensors is crucial for a scheme with distributed sensors to function successfully. The final goal of the communication is the information transfer from the sensor to the data center (end of cable or substation where data is analysed. This chapter refers to the different points of sensing as 'nodes'). Therefore, it was unanimously chosen to explore the field of 'RFID-like' technology to fulfil the role of communication between sensor nodes. This technology is highly promising and preliminary research gives it a good leverage over the others.

4.2 Illustration of concept

The envisioned system consists of a series of distributed sensor nodes over the length of the cable circuit. In case of a discharge in the cable, the node closest to the discharge location senses it and transmits the information to its neighbouring nodes. The neighbouring nodes in turn retransmit the information to their subsequent

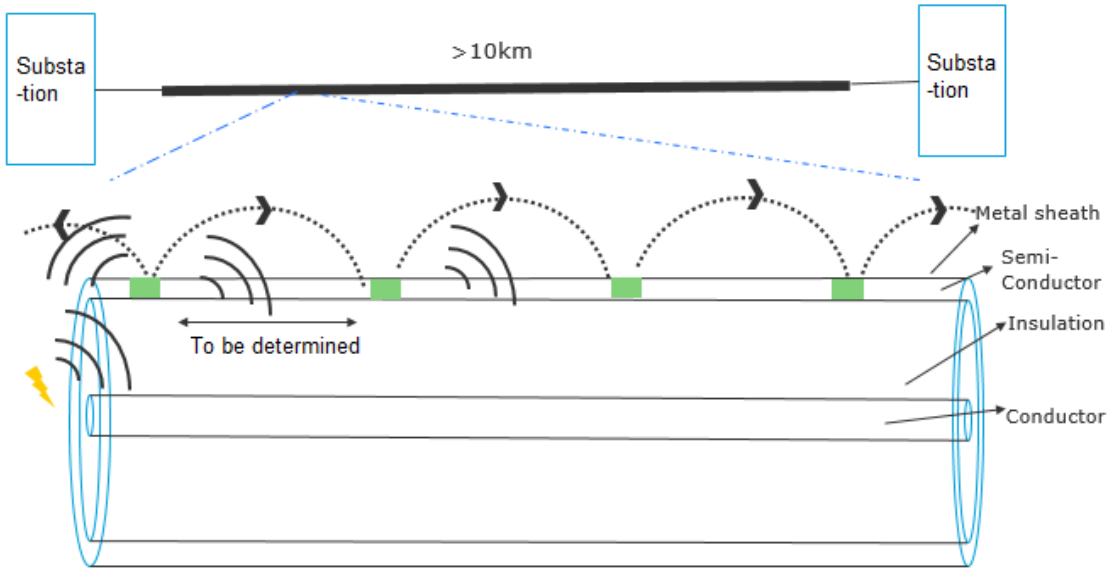

Figure 4.1: Illustration of the sensing scheme

neighbours, this is continued until the information reaches the cable end where it is analysed. Figure 4.1 shows a simple schematic of the sensing scheme.

The implementation of such a PD sensing system is broken down into three broad areas: Sensing, Communication and Power supply. A simplified illustration of the associated functional blocks are as shown in Figure 4.2. In order to show the closeness to the RFID tag technology, the RFID tag architecture is shown in Figure 4.3. The reason for the title of the chapter is that the design of the final unit is conceived to function like a RFID tag which senses a field (Electric or magnetic) and responds with it's characteristic field. Since the sensing of the PD is the most primary and vital followed by the communication scheme/technique which is highly challenging and new. This master thesis project deals prominently in these two areas and explores these in greater detail. This is a choice purely made due to the limitation in time and given the fact that there are in-numerous methods of supplying the sensor with necessary power, as the location of the sensor is in a region of high power density.

In order to develop a good correlation between the different parts, system engineering approach is adopted. The forthcoming sections describe the needs, requirements, trade off's and alternatives of each system block. Figure 4.4 shows the list of system objectives and their influences on each other. If the sensor unit is designed to have high functionality or intelligence, it sure would require more power for its functioning

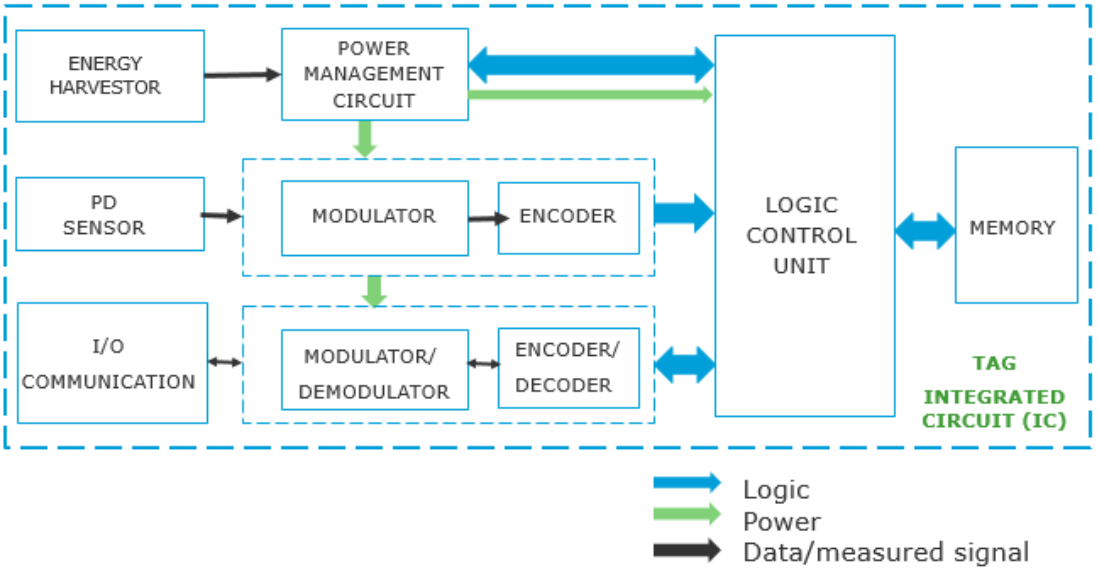

Figure 4.2: Block diagram of the envisioned sensor unit

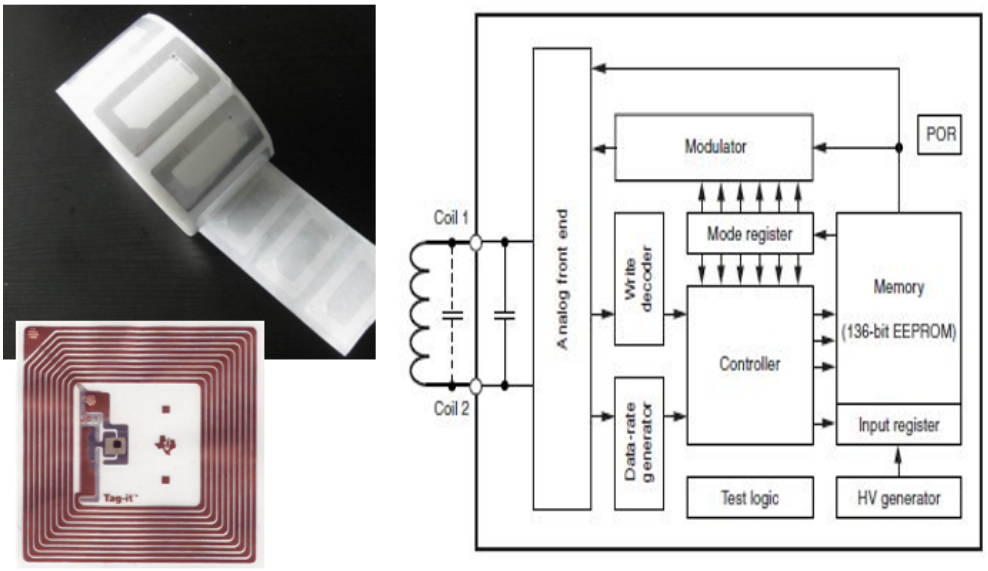

Figure 4.3: RFID tags (left) and the tag architecture (right). Courtesy:Tag-it©

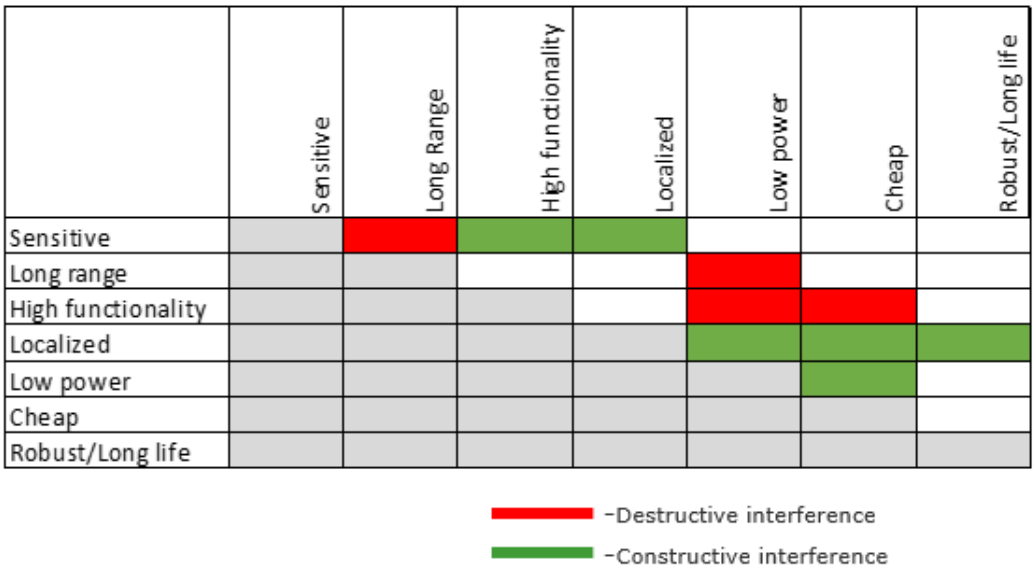

Figure 4.4: System synthesis with list of objectives and their influences on each other

which consequently would make the system more expensive. However, in case of designing a localized unit that is to be distributed along the cable, it needs to be designed with features such as low power, cheap and long life as this would make the system more feasible/economical. In case of clash between two objectives, there is a need to either resolve the clash with technical advancement in the field or by prioritizing one requirement over the other.

4.3 PD Sensing

The primary function of the whole system is the reliable detection of partial discharges. The conventional RFID tags that are based on communication through magnetic fields are not suitable for direct application in cables because the inclusion of such a tag on the curved outer surface (below the earth sheath) of the cable would leave the tag lying on the plane tangential to the magnetic field and no voltage will be induced on the tag. Therefore, alternative/customized designs need to be developed. In addition, the fact that RFIDs have only been known to function in air and are characterized by a narrow frequency band of reception and transmission makes the situation more complex for their direct implementation as a PD sensor. Thus, it

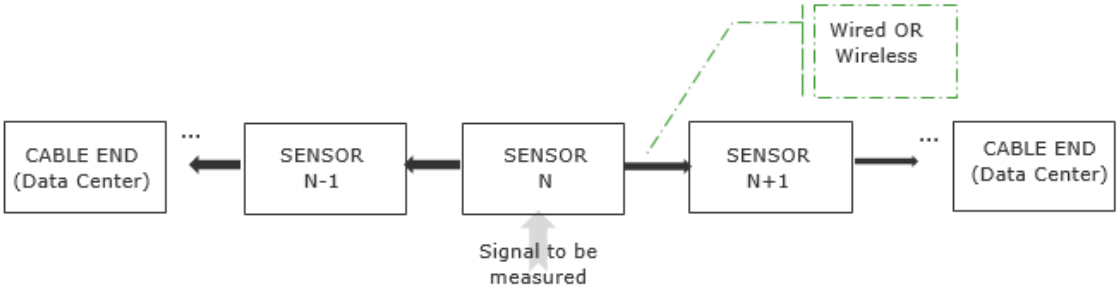

Figure 4.5: Relayed communication scheme

was recommended at the end of the feasibility analysis that the functionality of the RFID system be split into 2 sections, and the sensing of the fields (coming from the partial discharges) be accomplished by a dedicated sensor system that works continuously and the tag response or communication be fulfilled using another system such as the one with antennas/transceivers.

Once the decision to build localized sensor unit has been made, there are two other choices, either to include the sensor below the earth screen or create a possibility such as with the slot antennas to connect the sensor from the outside of the cable. Looking at this from the aspect of reliability of the cable network, the possibility of inclusion of a sensor from outside the cable would require some minor breach/opening of the earth screen (and/or lead screen) of the cables. And the safety regulations on HV cable systems do not allow that as it compromises the system robustness. Besides, for long cable systems that are commonly either underground or sub-sea there are very few opportunities to access the sensor unit for repair and refurbishment, since the associated costs are very high and close to the cost of replacement of a cable section in case of failure. Therefore, built-in sensor units are a better alternative than externally connected sensors.

With the conclusions of Chapter 3 combined with the insights in this section, distributed and built-in type capacitive and inductive sensor (to be included underneath the metallic earth screen of the cable) are chosen to be explored. Chapter 5 will discuss in depth the design and modelling of the built-in sensor types.

4.4 Communication

The success of the communication unit is crucial to the success of the sensing scheme. This section discusses various communication schemes available and concludes with

the most suitable alternative.

The two basic forms of communication: Direct and Relayed, will be weighed against each other in this section. By direct communication, it is meant that the sensor unit directly communicates the information to the cable end using a given channel, it may either be wireless or wired. While by relayed communication, reference is drawn to a scheme similar to the one shown in Figure 4.5. All things considered, relayed communication is more rewarding since there is more redundancy in the system in spite of it being more complex than the first. The next choice to be made is the nature of the channel that will be used to relay information between the sensor units, the two obvious choices will be: wired or wireless. In this case, arguably, wireless communication is the better amongst the two because wired communication despite being simple to execute creates a single point of failure. However, in case of the wireless scheme, since it is not possible to communicate the information from inside the cable to the outside (skin effects on the metallic screen prevents this), the cable itself is used as the communication channel. It is a challenge to solve the task of inclusion of the transceiver inside the coaxial cable and dimension it suitably so as to function in a prescribed frequency range that will not be highly attenuated by the cable. Taking leads from the antenna simulations of Chapter 3, it is a good opportunity to test one of the alternatives to fulfil the requirement of the communication task.

In summary, relayed wireless communication based on 'wireless antenna-like transceivers' is chosen as the final model for the communication module.

4.5 Power Supply

Power supply is a major concern in most sensor implementation schemes, especially when the sensor is installed remotely. Though it is not the priority of this project, the field is touched upon briefly to know what the possible alternatives are in this case. The major alternatives that one can think about are as listed below:

1. **Wired power transfer from cable ends:**

   This is the most crude and basic scheme that can be used to fulfill the energy requirements. However, it may prove to be the single point of failure. Nevertheless, several systems work based on wired energy, the biggest of its kind being the electrical grid. The major advantage of this scheme is its simplicity in implementation. In the case of a stand alone sensor unit such as this, the moajor advantage is the adequacy of a transducer and power regulator in contrast to an antenna, matching circuit and a rectifier in the case of wireless

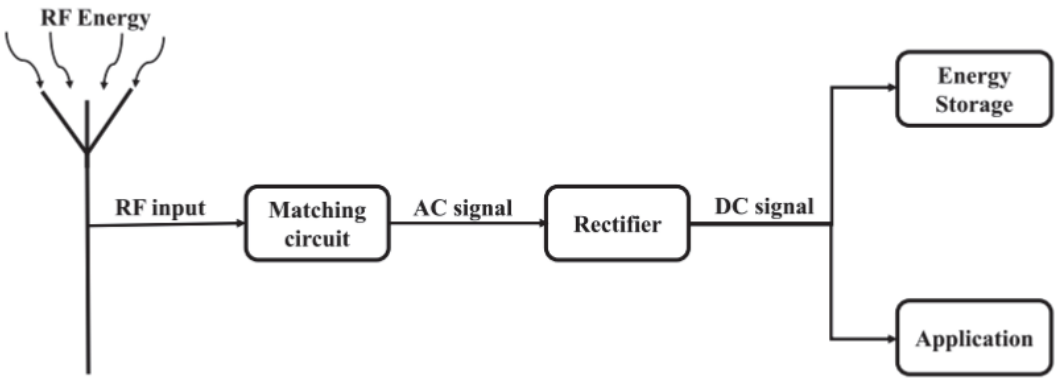

Figure 4.6: A simplified RF energy harvesting scheme [37]

power harvesting. One such method is described in[35], called contact-less power transfer using an unshielded twisted pair (UTP), which is interesting for this application. But it can be argued that the large fields at 50 Hz that are prevalent inside the cable will have a severe effect on this scheme limiting its implementation. But, that is a discussion for future research.

2. **Wireless energy harvesting from the 50 Hz field:**

   Inductive coils are used to harvest energy from the 50 Hz magnetic field. These coils are required to have a large value of inductance in the order of a few Henrys and hence are bulky. [36] is one such conference proceeding that demonstrates the same. Due to their large size it would not be possible to incorporate them inside the cable for powering distributed sensors. Hence, this is not a suitable solution.

3. **Wireless energy harvesting from additional RF fields:**

   It is a widely used method to harvest energy from RF fields, [37] presents one such scheme using an antenna and a rectifier as shown in Figure 4.6. It is demonstrated in the same that a patch antenna working in the frequency range of 1-10 GHz can harvest energy with an efficiency of 85%. It is clear that transmission of such high frequencies are out of the question when it comes to HV power cables. Nevertheless, this is considered as an area with high potential for this application since it is possible to supply additional energy at radio frequency to power the sensor.

4. **Localized energy harvesting in the semi-conductive layer:**

   Since the semiconducting layer of the cable is not a perfect conductor and

the electric field lines (though very few) extend beyond this layer at 50 Hz. It provides an opportunity to harvest energy over this layer using it like a capacitive divider. Drawing up some rough estimates of electric field, the average electric field in this layer is around 4 V/mm. This provides sufficient opportunity to harvest energy locally at the sensor location. Again, it may be argued that the intricate circuiting within the cable layers and inclusion of electronics is practically impossible to realize, that is again a discussion for future research. Since it is out of the scope of this thesis, its effects and required protection schemes will be studied in detail in the future research.

4.6 Dealing with contingency events such as Short-circuit and Lightning strike

In the case of chance events of faults or lightning strike over the system connected to the cable circuit equipped with built-in capacitive dividers, it becomes imperative to think about its potential destructive effects on the sensor unit. The energy induced over the sensor, heat produced, or flash overs across the divider due to large voltages may be some of the potential effects. These effects cannot be determined accurately at this stage. However, we can foresee the use of a device such as a spark gap or a fuse that will help bypass the large fault currents from damaging the sensor.

4.7 Conclusion

This chapter describes the envisioned system and its associated parts. Based on the recommendations made in this chapter partial discharge sensor types namely, the built-in capacitive and inductive sensors are modelled in detail and their transfer functions are compared in the next chapter.

CHAPTER

5

PD SENSOR MODELLING

5.1 Introduction

In this chapter, two sensor alternatives, namely the built-in capacitive sensor and the built-in inductive sensor are designed and their transfer functions are simulated using MATLAB. Their design details, dimensions and associated equivalent circuits are presented sequentially. The generalized design steps are as listed below:

General steps to the sensor modelling

1. Derive the equivalent circuit.
2. Obtain the circuit elements.
3. Implement the attenuation (gamma) of the cable.
4. Implement a generic PD pulse.
5. Derive the transfer function based on the equivalent circuit.
6. Obtain the sensitivity of the sensor.

5.2 Built-in capacitive sensor

The capacitive sensor is modelled internally in the power cable, located above the extruded insulation screen which is a semi conductive layer. The insulation screen is commonly followed by a layer of swelling tape which is also semi conductive in nature. However, in order to improve the electrical coupling to the sensor, this layer is removed and a layer of insulation of similar thickness is introduced instead. Figure 5.1 illustrates the proposed idea.

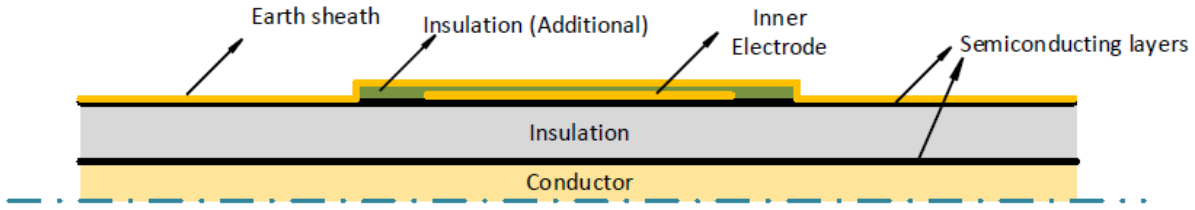

Figure 5.1: An illustration of the built-in capacitive sensor

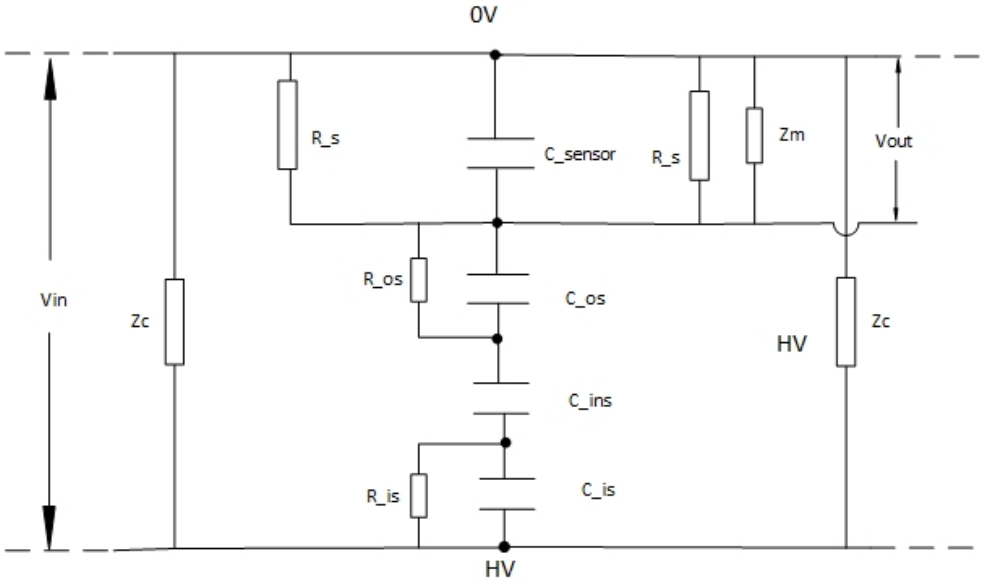

Figure 5.2: Equivalent circuit of the built-in capacitive sensor

The first step towards modelling a capacitive sensor is making an equivalent circuit and deriving its transfer function/ratio. The equivalent circuit of the sensor is shown in Figure 5.2. C_{ins} here represents the capacitance of the cable insulation, $C_{is}||R_{is}$ and $C_{os}||R_{os}$ represent capacitance of the inner and outer semi conductive layers modelled with a loss resistor in parallel, C_{sensor} represents the capacitance of the sensor due to the additional insulating layer that is introduced, R_s is the resistance of the semiconducting layer in the axial direction present across the output terminals of the sensor and Z_m is the measuring impedance, taken as 50 Ω.

From the equivalent circuit the transfer function of the sensor is derived which is given in Eq.5.1.The transfer ratio (also known as transmission coefficient) is defined as the fraction of the input pulse transferred to the output. In case of a capacitive sensor the transfer function is the ratio of the two voltages (output and input) and is hence unit less.

$$TF(\omega) = \frac{V_{out}(\omega)}{V_{in}(\omega)} = \frac{1}{X_{c1}}.[\frac{1}{Z_m} + \frac{1}{R_s} + \frac{1}{X_{sensor}}]^{-1} \tag{5.1}$$

$$\text{And } X_{c1} = [\tfrac{1}{j\omega}][\tfrac{1}{C_{ins}} + \tfrac{1}{C^*_{os}} + \tfrac{1}{C^*_{is}}]$$

where, C^*_{is} and C^*_{os} are the complex capacitance of the inner and outer semiconducting layers.

The values of C^*_{is} and C^*_{os} are obtained based on the high frequency characterization of the semiconducting layers as described in Section 2.5.1. Therefore, it includes the resistive losses R_{is} and R_{os} through the complex dielectric permittivity used in the calculation for the capacitance. The insulation is characterized by a relative permittivity of 2.3+j0.001 corresponding to XLPE. Figure 5.3 shows the transfer coefficient of the built-in capacitive divider obtained using MATLAB. The flat curve of the transfer coefficient at frequencies above 10 MHz is advantageous as it eliminates the need for additional electronics at the output of the sensor.

In order to model pulse propagation along the cable the attenuation of the cable obtained based on Eq.2.17 and validated in section 2.5.2 is used. A partial discharge pulse is modelled based on Eq.5.2. The width of a partial discharge pulse(current/ voltage) in reality depends on various factors such as the location of the PD, type of PD, distance travelled, insulation type etc. However, a generic PD pulse at the source of the discharge is a very narrow pulse in time domain with a very short rise time. Therefore, a dirac-delta function with amplitude 1 can be used as a sufficient estimate. Otherwise, in order to represent the model closer to reality a double exponential function can be used. The function that was used in the simulation is

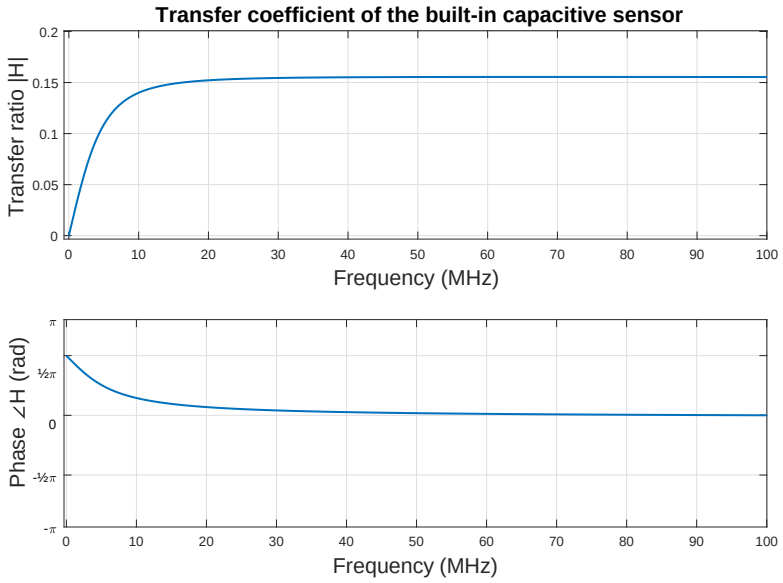

Figure 5.3: Transfer function of the built-in capacitive sensor

shown in Eq.5.2 and its respective pulse output is shown in Figure 5.4.

$$i_{cable} = e^{-A1.t/\tau} - e^{-A2.t/\tau} \tag{5.2}$$

The charge is estimated by integrating the current pulse over the pulse width and scaling it based on the input charge of the partial discharge. Figure 5.5 shows the sensitivity of the capacitive divider towards a 1 pC pulse(4 ns rise time) with distance. Table 5.1 lists the values of maximum voltage and current output of the sensor at various distances along the cable. The voltage and current can be used interchangeably based on the value of characteristic impedance of the cable which is taken as 30Ω in this case.

Table 5.1: Estimates of voltage and current at the output terminals of the built-in capacitive sensor

	Charge	1 pC		10 pC	
Distance (m)	Pulse width	Peak current (mA)	Peak voltage (mV)	Peak current (mA)	Peak voltage (mV)
0	5 ns	0.093	2.80	0.93	28.0
5	7.5 ns	0.063	1.90	0.63	19.0
10	10 ns	0.055	1.65	0.55	16.5
50	100 ns	0.022	0.65	0.22	6.5
100	150 ns	0.013	0.38	0.13	3.8

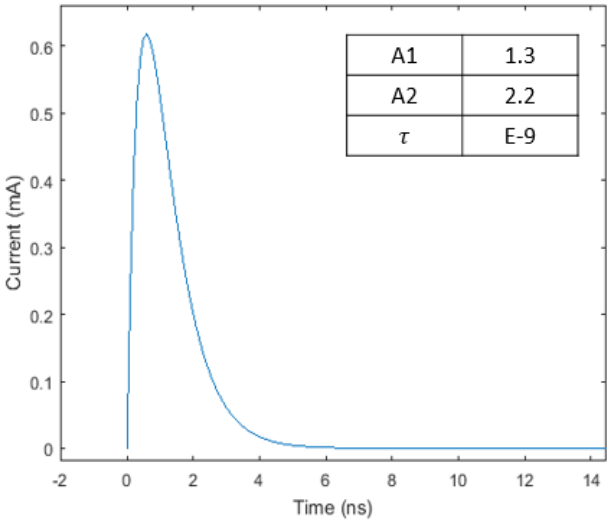

Figure 5.4: PD current pulse simulated based on Eq.5.2

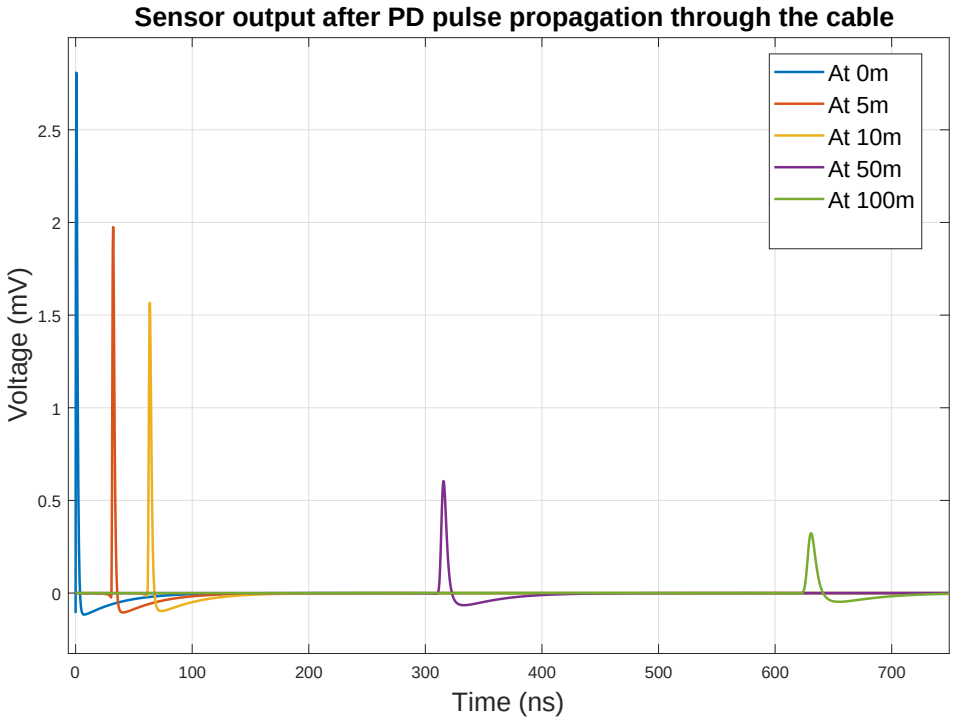

Figure 5.5: Sensitivity of the built-in capacitive sensor towards a 1 pC pulse with distance

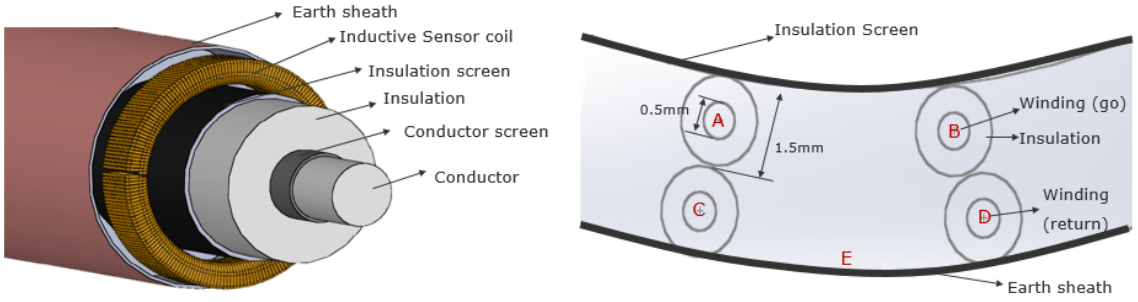

(a) 3-dimensional view

(b) Radial section

Figure 5.6: Illustration of the built-in inductive sensor

The sensitivity of the system is defined as the smallest magnitude of discharge that can be detected in the presence of noise and it is expressed in picocoulombs (pC). There are two kinds of noise in a system, one from the back-end electronics and the other from the circuit itself. The latter is a stochastic phenomenon and cannot be estimated since it differs with every circuit. Therefore, DNV GL'S Smart Cable Guard design is taken as a benchmark to deduce a maximum range. A realistic and achievable signal threshold of 1.5 mV (2×noise floor) is taken as the minimum detectable signal for the built-in capacitive sensor design and based on this a sensitivity of 1 pC at 10 m is achievable.

5.3 Built-in inductive sensor

The inductive sensor is modelled as a toroid of 1 mm thickness (between the windings) placed over the insulation screen of the cable as shown in Figure 5.6. However, the inductive coil in the figure is slightly exaggerated in size, with greater thickness and large number of turns for illustrative purposes. In reality, the number of windings is kept as low as possible in order to reduce the effect of inter-winding capacitance and the resonance between the self-inductance of the coil and the stray capacitance. The winding of the inductive sensor are insulated and the semi-conductive tape above the insulation screen is eliminated in order to prevent the short-circuiting of the windings. The inter-winding capacitance and the stray capacitance to the earth sheath of the cable is calculated and incorporated in the simulation in order to obtain a real representation of the sensor model. The equivalent circuit of the inductive sensor is shown in Figure 5.7 .

The expression in Eq.5.3 gives the transfer function of the inductive sensor. In some cases it is also referred to as the transfer impedance of the sensor as it is the

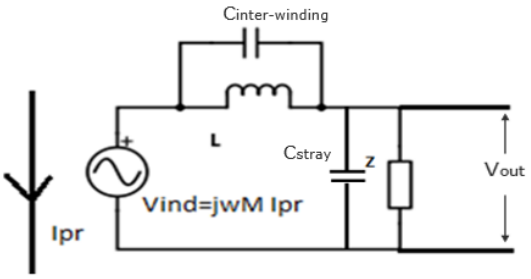

Figure 5.7: Equivalent circuit of the built-in inductive sensor model

ratio of the output voltage to the current in the primary circuit. The values of the stray capacitances between windings and to the earth sheath are deduced through the equivalent circuit shown in Figure 5.8. The stray capacitances are distributed over the windings and hence the terms C_w(inter-winding capacitance, between 2 windings) and C_s (stray capacitance, between winding and earth sheath) need to take note of the number of turns of coil used.

$$T(\omega) = \frac{V_{out}(\omega)}{I_{pr}(\omega)} = j\omega M_c . \frac{Z_1}{Z_1 + Z2} \tag{5.3}$$

$$where, Z_1 = \frac{Z_m}{1 + j\omega Z_m C_s}$$

$$Z_2 = \frac{j\omega L}{1 - \omega^2 L C_w}$$

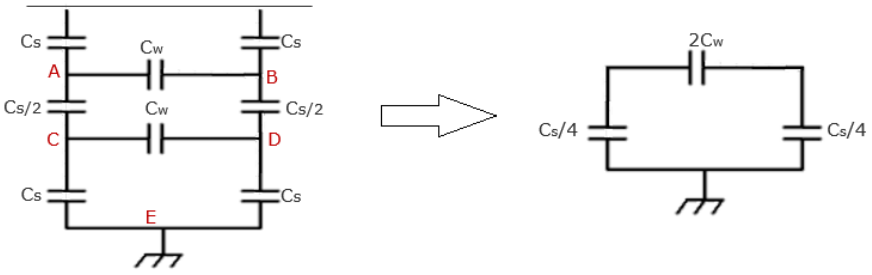

Figure 5.8: Equivalent circuit to obtain stay capacitive effects of the rogowski coil

Simulation of such a design show that the resonance between the self-inductance of the coil (L) and the stray capacitance to earth sheath (C_s) are very dominant

thereby annihilating the transfer function completely. Based on the values of L and C_s the resonance frequency is calculated using the expression $f_r = 1/(2\pi\sqrt{LC})$, at 4.43 MHz. Figure 5.9a gives the simulated estimation of the transfer coefficient showing the resonance peak at 4.4 MHz. The resonance effect can be seen in the plot for voltage output shown in Figure 5.9b.

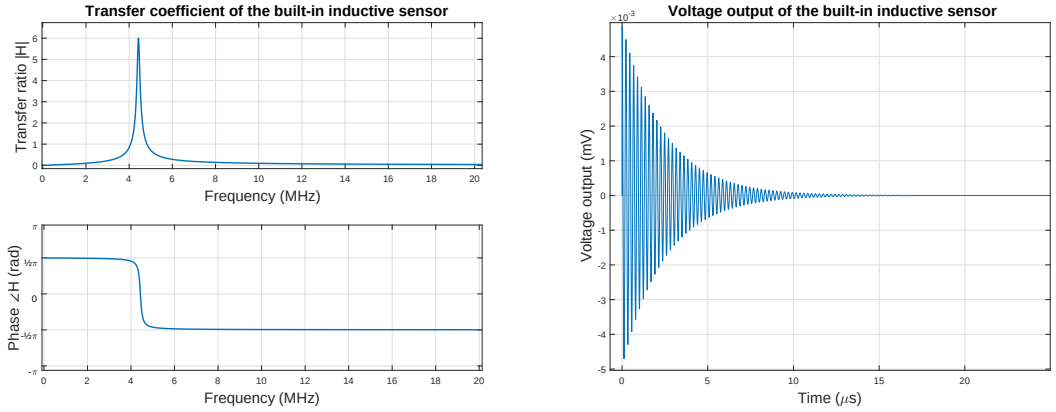

(a) (b)

Figure 5.9: Simulation results of the built-in inductive sensor. (a) Estimated transfer coefficient (b) Estimated output voltage

Due to the undesirable effects of resonance arising from the stray capacitances that hinder the implementation of the inductive sensor, a toroid with coaxial cable is implemented instead. Standard coaxial cable TCF119 that functions upto the microwave frequencies (upto 110 GHz) has a outer diameter of 1.7 mm and is suitable for the application because of its small thickness. The impedance of the cable is 50Ω and the distributed capacitance is 85 pF/m. The use of the coax helps eliminate the inter-winding capacitance but the distributed capacitance to screen remains and hence the new transfer function is as given in equation 5.4. The system has a resonance frequency at 68.87 MHz (between L and C_{coax}). This series resonance can be seen in figure 5.10a.

$$T(\omega) = \frac{V_{out}(\omega)}{I_{pr}(\omega)} = j\omega M_c.[1 + \frac{j\omega L}{Z_m}(1 + j\omega Z_m C_{coax})]^{-1} \tag{5.4}$$

The resonance frequency is pushed to a higher frequencies when compared to the previous case. However, the model does not provide reliable results for frequencies beyond the resonant limit because then the current probe requires to be modelled as a transmission line model with distributed parameters instead of a lumped parameter

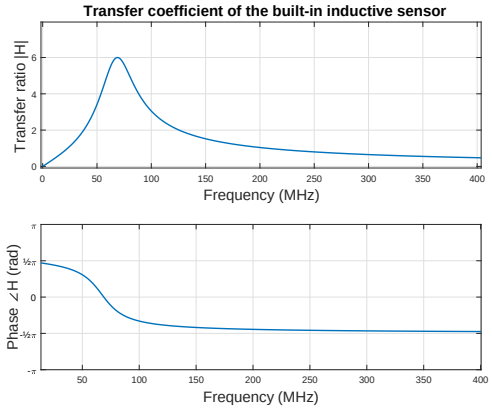

(a)

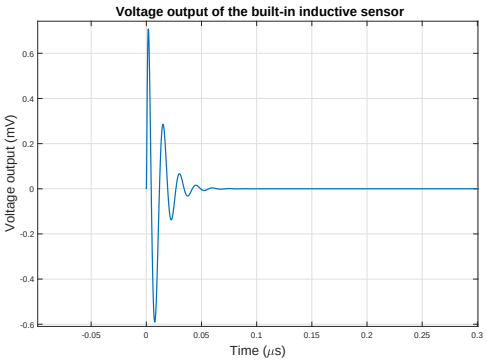

(b)

Figure 5.10: Simulation results of the built-in inductive sensor made with coaxial cable. (a) Estimated transfer coefficient (b) Estimated output voltage

model as done now. Nevertheless, Table 5.2 gives the sensitivity of the design towards a PD pulse with increasing distance from the origin.

Table 5.2: Voltage outputs at inductive sensor terminals implemented with Coaxial cable

Distance (m)	Charge	1 pC	5 pC
	Pulse width	Peak to peak voltage (mV)	Peak to peak voltage (mV)
0	5 ns	3	15
5	7.5 ns	1.15	5.75
10	10 ns	0.45	2.25
50	100 ns	0.038	0.19
100	150 ns	0.014	0.07

5.4 Conclusion

By comparing the flat transfer coefficient of the capacitive sensor and its simple and compact construction to the oscillating outputs obtained with the inductive sensor due to its resonant design and complicated construction. It can be concluded that the performance of the built-in capacitive sensor is relatively superior to the built-in inductive sensor design. Additionally, the integrity of the original cable structure is

preserved with the implementation of the capacitive sensor design. While the inductive sensor is difficult to build and requires more space above the insulation screen. As a consequence, the capacitive sensor is chosen as a more suitable alternative for this particular application. And the next chapter will discuss the experimental results on the built-in capacitive sensor.

CHAPTER

6

LABORATORY MEASUREMENTS

6.1 Built-in Capacitive sensor

The objective of the tests carried out on the built-in capacitive sensor were primarily to determine the performance of the design by obtaining its transfer function. The structural design was the same as used in the MATLAB simulations of Chapter 5. The experiments were carried out at the High voltage laboratory in TU Delft. The specification of the cable circuit used for the tests is listed in Table 6.1. Various design parameters were varied to check their influences on the transfer function, the results of which are presented in the forthcoming sections.

6.1.1 Measurement method

Since the measurements involve the injection of high frequency pulses, the nature of the connections should be made all coaxial, in order to minimize the impact of irregularities as far as possible in order to avoid reflections and large loops in the system that will impede the currents at high frequencies. As shown in Figure 6.1, a special adapter with a lead cap is built to fit perfectly on the cable end. The adapter is then securely fitted over the cable end using a house clamp. This set-up minimizes

the loops in the system and allows a smooth transition between the measuring cable (eg:50 Ω- RG58) to the power cable.

Table 6.1: Cable specifications

Cable specifications- TU Delft	
Insulation	XLPE
Circuit length	43.25 m
Earth screen type	Single, solid
Conductor radius (r_c)	8 mm($240\,mm^2$)
Thickness of conductor screen(t_{cs})	1 mm
Outer radius of insulation (r_i)	13 mm
Thickness of insulation screen (t_{is})	1 mm

Figure 6.1: Cable end prepared for pulse injection

The transmission line parameters need to be measured before the measurements for the sensor transfer function are performed. These measurements are based on the pulse reflection method as presented in [38] [39]. Since the measurements for the sensor transfer function are aimed to reach upto 50 MHz, the measurement system is first calibrated for such high frequencies. The connections are made based on Figure 6.2, at this stage the cable far end is left open. The coaxial cable used for

measurement is matched to the oscilloscope (at 50 Ω) to avoid reflections in the measurement cable. First, the long coaxial cable is calibrated by short-circuiting it. The injected pulse (V_{inj}) and the reflected pulses (V_r) are recorded and the reflection coefficient $H_{meas} = V_r/V_{inj}$ is calculated. In an ideal lossless system $H_{meas} = -1$. Secondly, the short circuit is removed from the long coax and the measuring cable is connected to the CBLUT (Cable under test). Using copper tape the CBLUT is short-circuited to calculate the series inductance of the adapter used in the set-up. The injected and the reflected pulses are recorded and the reflection coefficient is re-calculated by compensating for the attenuation in the measurement cable that was estimated in the previous step. This is given by the expression;

$$H_1 = \frac{V_r}{V_{inj}} = H_{meas} \cdot \frac{Z_{adpt} - Z_c}{Z_{adpt} + Z_c} \tag{6.1}$$

Where Z_c is the characteristic impedance of the measurement cable (50 Ω). From Eq.6.1 the impedance of the adapter (Z_{adpt}) is deduced. The value of which is in the range of 3 nH at the frequencies upto 50 MHz as shown in Figure 6.3.

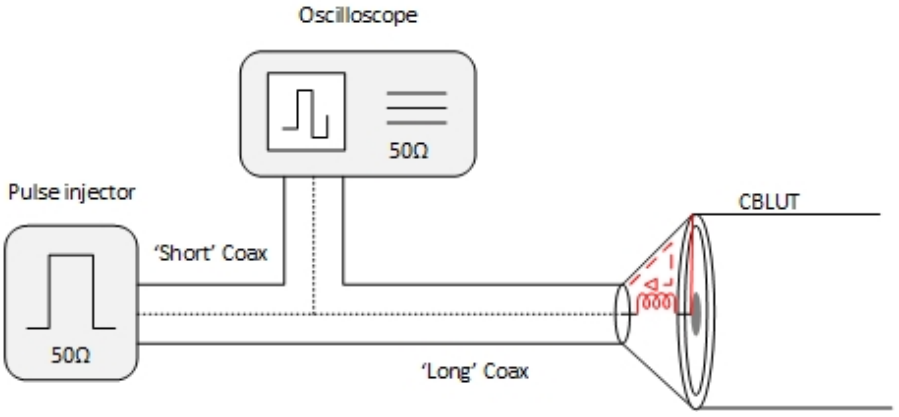

Figure 6.2: Measuring the inductance of the adapter

The short circuit is removed from the CBLUT and the pulses are injected using the PD calibrator. A series of pulse reflections are recorded through this measurement as shown in Figure 6.4. The first reflection (V_{r2}) from the cable near end and the injected pulse (V_{inj}) are recorded and the reflection coefficient $H_2 = V_{r1}/V_{inj}$ is calculated. The characteristic impedance of the cable is deduced through Eq.6.2 and is close to 20 Ω as shown in Figure 6.5.

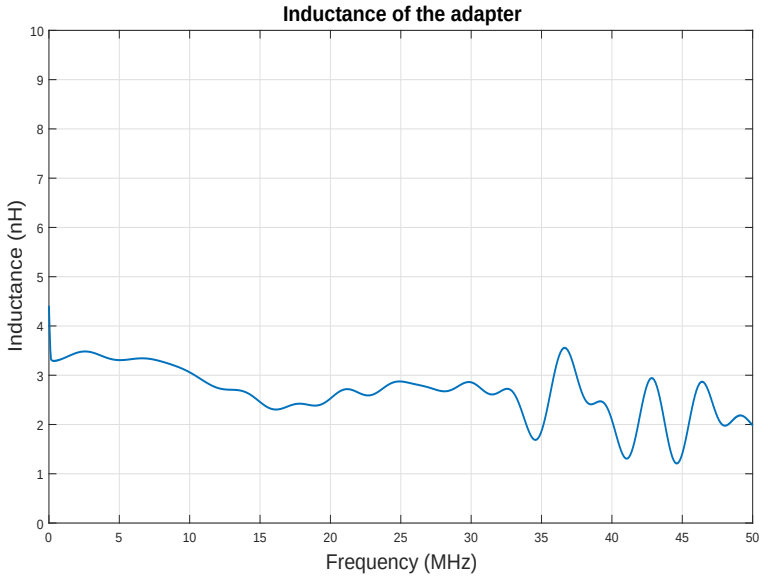

Figure 6.3: Measured inductance of the adapter

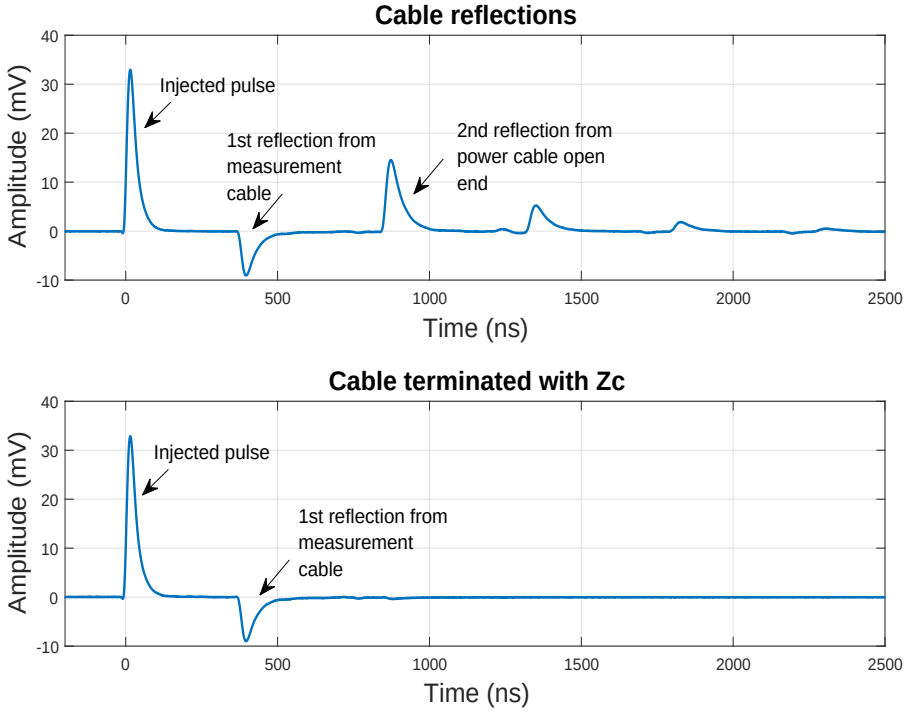

Figure 6.4: Pulse reflections before and after terminating the cable far end with the characteristic impedance of the CBLUT

$$Z_{c-CBLUT} = Z_c.\frac{H_{meas} + H_2}{H_{meas} - H_2} - Z_{adpt} \tag{6.2}$$

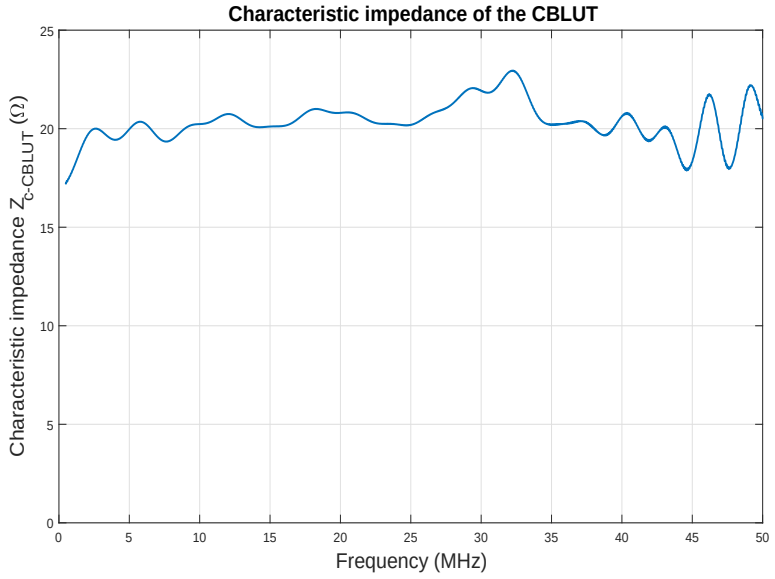

Figure 6.5: Measured characteristic impedance of the CBLUT

The second reflection (V_{r2}) from the power cable end shown in Figure 6.4 enables the calculation of the propagation constant(γ) of the CBLUT through Eq.6.3.

$$H_3 = \frac{V_{r2}}{V_{inj}} = H_{meas}.\Gamma_V^+.e^{-\gamma 2l_c}.\Gamma_V^- \tag{6.3}$$

Γ_V^+ is the transmission coefficient from the measuring cable to the CBLUT and Γ_V^- is the transmission coefficient from the CBLUT back to the measuring cable. They are given by Eq.6.4;

$$\Gamma_V^+ = \frac{2Z_{c-CBLUT}}{Z_{c-CBLUT} + Z_c + Z_{adpt}} \quad and \quad \Gamma_V^- = \frac{2Z_c}{Z_{c-CBLUT} + Z_c + Z_{adpt}} \tag{6.4}$$

The measured attenuation and phase velocity of the cable is shown in Figure 6.6. The values of attenuation are deviant at frequencies above 35 MHz, this is due to the low frequency content at these high frequencies in the pulse used for measurements.

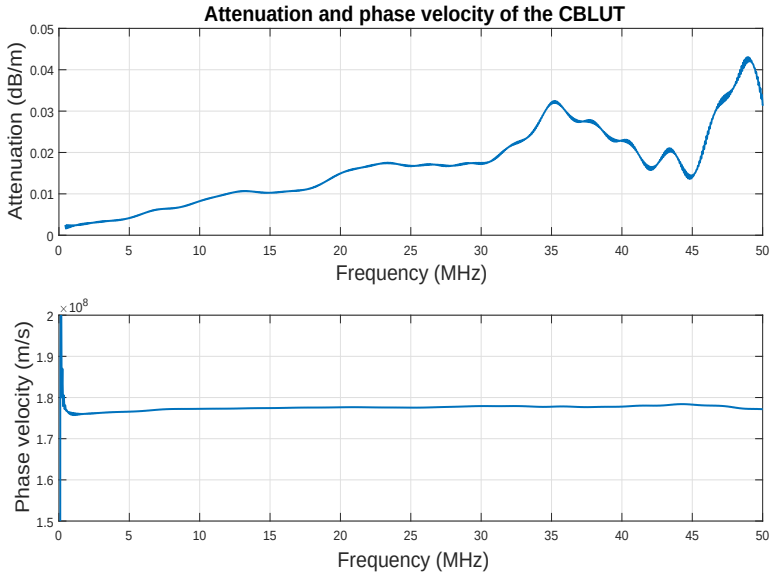

Figure 6.6: Measured attenuation and phase velocity of the CBLUT

The cable far end is terminated with a combination of resistors in parallel such that the net resistance value is close to the characteristic impedance of the cable that was pre-determined as discussed. Figure 6.4 shows the cable reflections before and after terminating the cable far end with the characteristic impedance Zc. The cable far end is then sufficiently insulated and shielded using copper mesh to avoid external disturbances in the measurement set-up, this is shown in Figure 6.7.

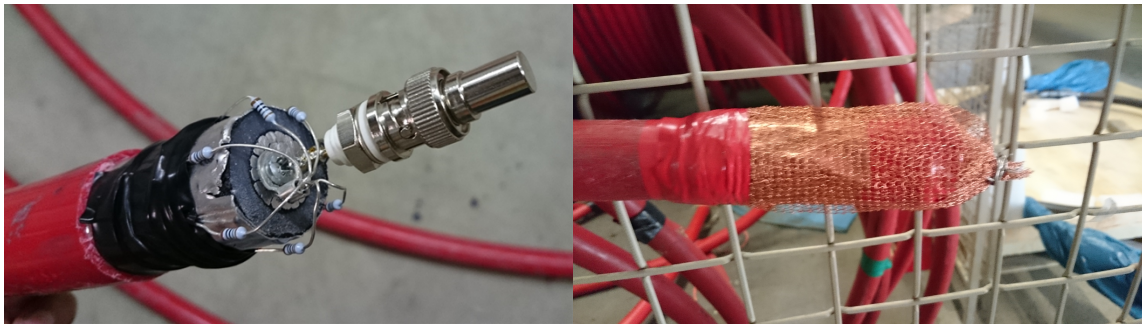

(a) (b)

Figure 6.7: Cable (a) terminated with the characteristic impedance (Z_c) and (b) shielded using copper mesh

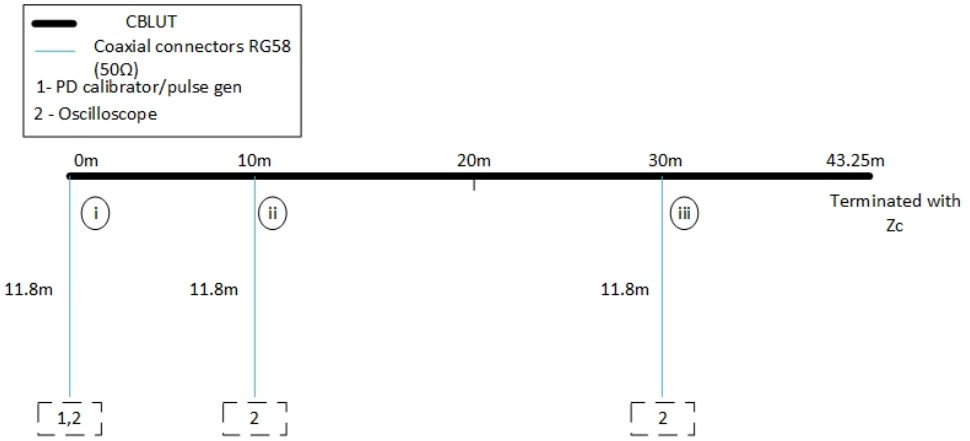

Figure 6.8: Schematic of the test plan showing the sensor locations

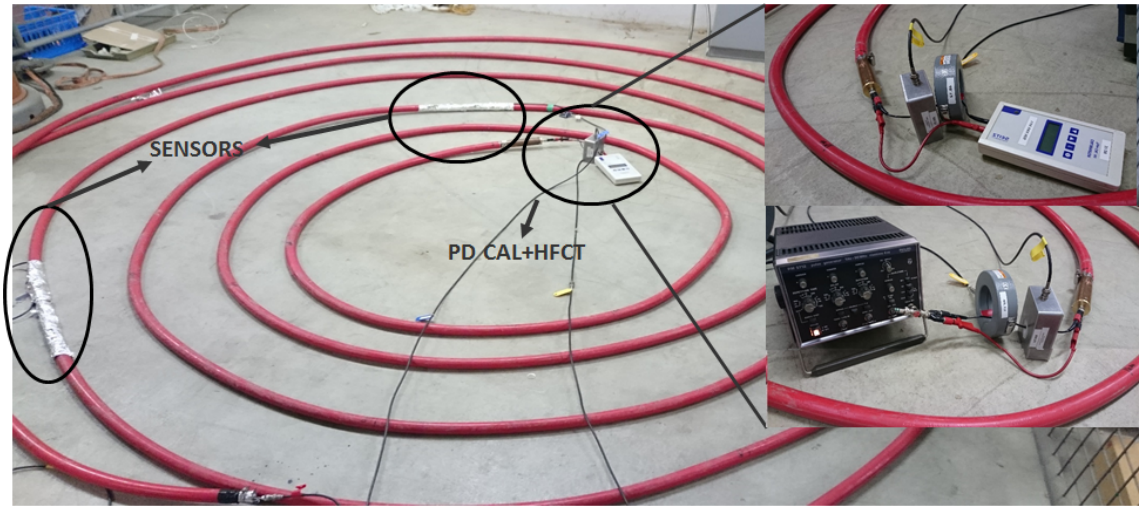

Figure 6.9: Actual test setup at the laboratory in TU Delft

The testing scheme used at the HV lab in TU Delft is shown in Figure 6.9. It can be observed from the figure that coaxial cables of equal lengths are used to make connections to the CBLUT, this is done in order to help eliminate the effect of additional time delay and attenuation in these cables thereby enabling an easy differentiation of the pulses coming from multiple cable locations without accounting for the losses in them. The detailed connection diagram to the sensor using coaxial cables is shown in Figure 6.10. The core of the coaxial cable (RG58) is connected to the inner electrode of the sensor and the screen of the coax is connected to the earth sheath.

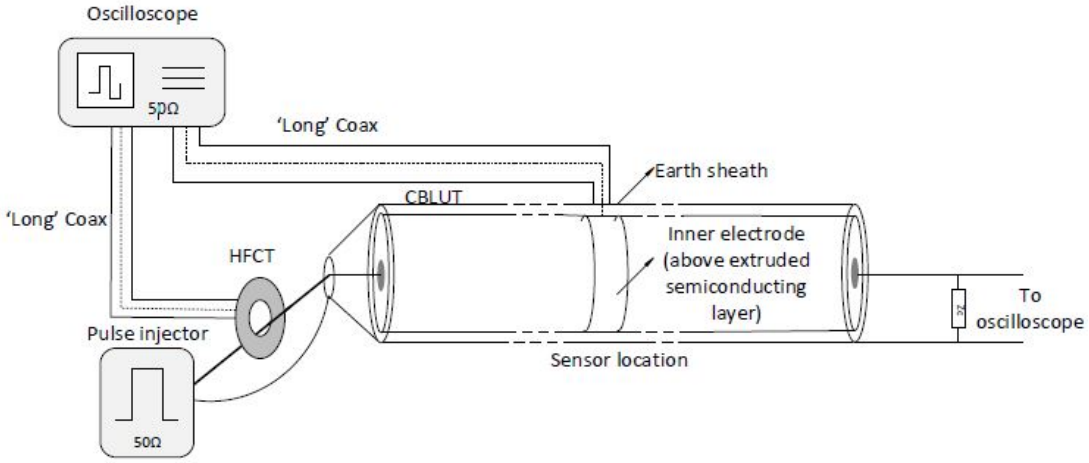

Figure 6.10: Measurement schematic showing the connection to one sensor unit

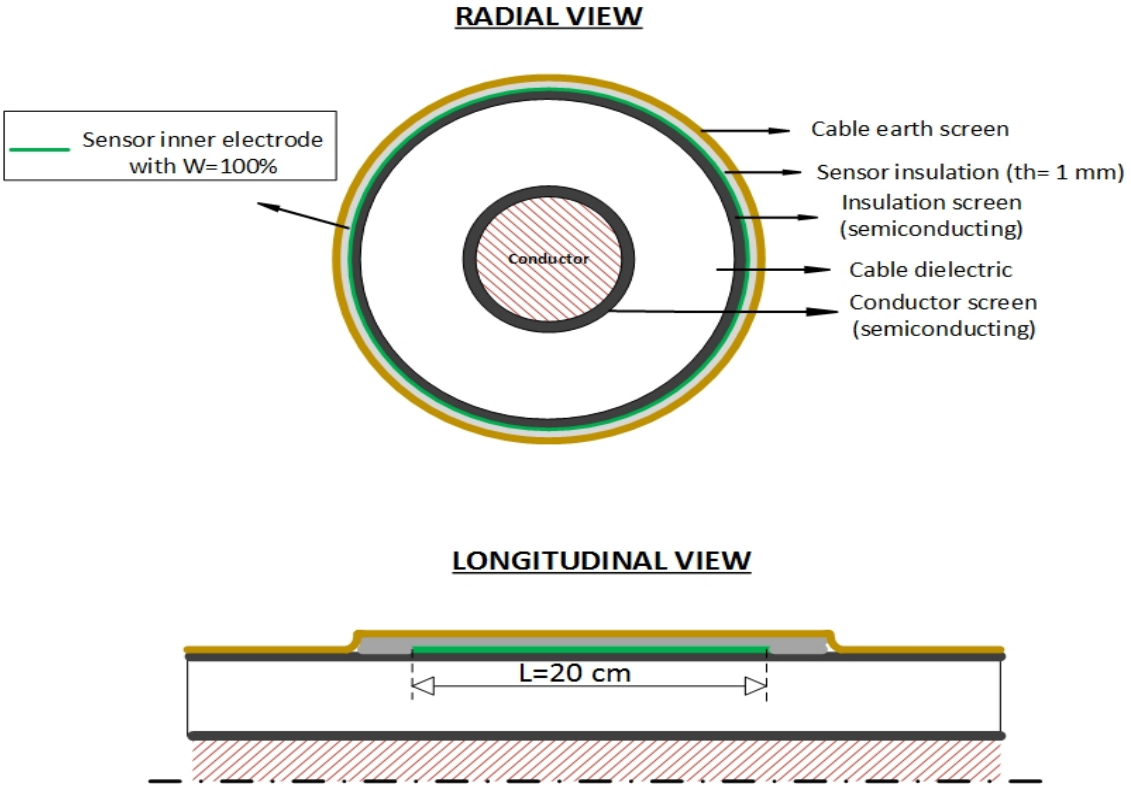

Figure 6.11: Illustration of the standard built-in capacitive sensor showing dimensions of inner electrode and thickness of insulation

The inner electrode of the sensors are constructed with copper foil as shown in Figure 6.12a, then 1 mm thickness of paper is used as insulation as shown in Figure 6.12b and finally the metallic earth screen is reconstructed as shown in Figure 6.12c. The dimensions of the standard sensor illustrated through Figure 6.11, are as follows:

1. Length of inner electrode- 20 cm
2. Width of inner electrode- 100%, concentric
3. Insulation thickness- 1 mm, paper (dry)

For pulse injection at the cable near end, two alternatives are used.

- **PD calibrator-** Pulses with rise time of 6-8 ns
- **PHILIPS pulse injector-** Pulses with rise time of 4 ns

While the PD calibrator is capable of injecting pulses of 10 pC upto 1000 nC, on the other hand the Philips pulse injector can only inject pulses upto a peak voltage of 10 V. In order to record the individual pulse shapes of the PD calibrator and the pulse injector, the two are first connected directly to the oscilloscope and then connected to the cable circuit through a HFCT (High Frequency Current Transformer). Through this is possible to see the transformation of the pulse shape due to the load (the cable system) connected to the output of the PD calibrator/pulse injector. The pulses and their frequency content through FFT (Fast Fourier Transformation) is shown in Figure 6.13 and 6.14. The Philips pulse injector has frequency content upto 350 MHz while the PD calibrator is limited to 150 MHz. Two different Current transformers are used, the both have a different transfer impedance (Z_t) and bandwidth. The purpose of which is to check against each others performance in order to improve the reliability of the results obtained. The specifications of the two CTs are listed below;

- **HFCT 1-** Z_t=9.1 mV/mA, BW-30 kHz up to 100 MHz
- **HFCT 2-** Z_t=1 mV/mA, BW-10 kHz up to 500 MHz

The transformation of the two pulse waveforms after connection to the cable circuit, recorded using the two CTs is shown in Figure 6.15 and 6.16.

However, the frequency content of the voltage pulse at the terminals of the CBLUT is less than 2% at frequencies above 100 MHz irrespective of which device is used to inject pulses. This can be seen in Figure 6.17. Hence, the PD calibrator was used along with HFCT 1 for further measurements.

(a) Inner electrode

(b) Insulation over inner electrode

(c) Metallic earth screen reconstruction

Figure 6.12: Stepwise sensor construction

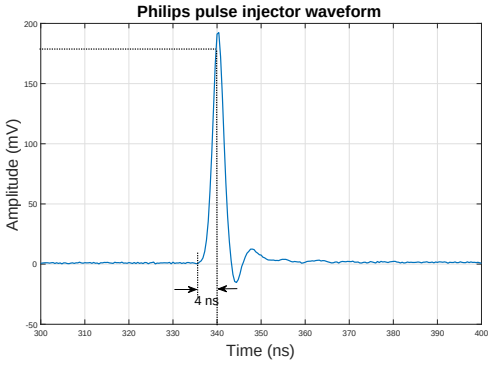

(a) Using Philips Pulse Injector

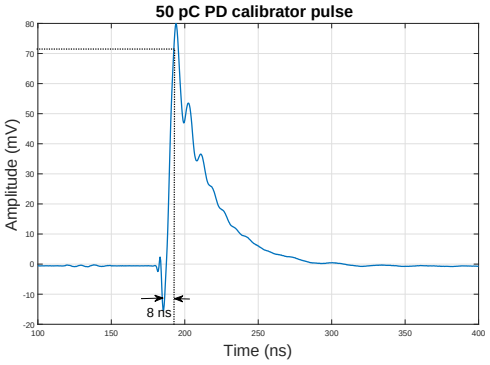

(b) Using PD calibrator

Figure 6.13: Waveform of the pulses injected during testing (a) Philips pulse injector and (b) the PD calibrator

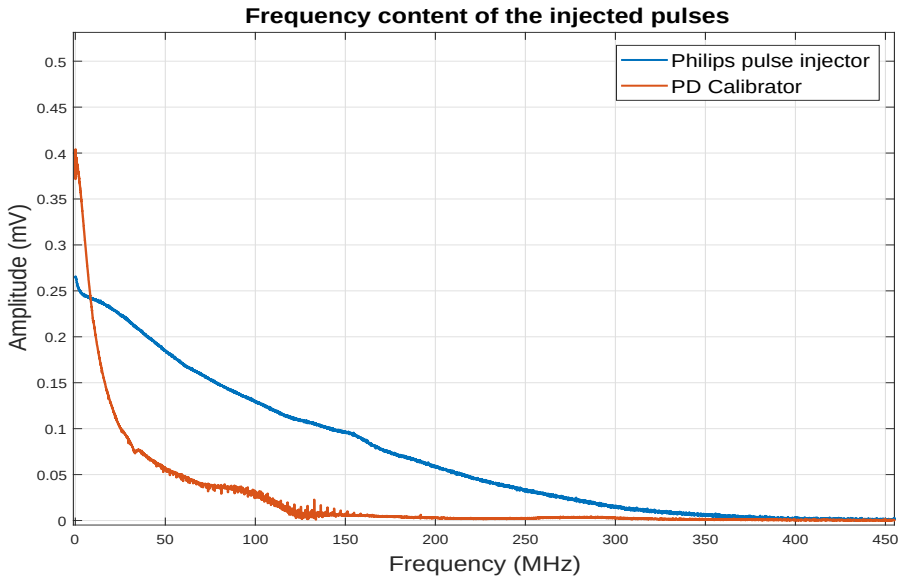

Figure 6.14: Frequency content of the two waveforms shown in Figure.6.13

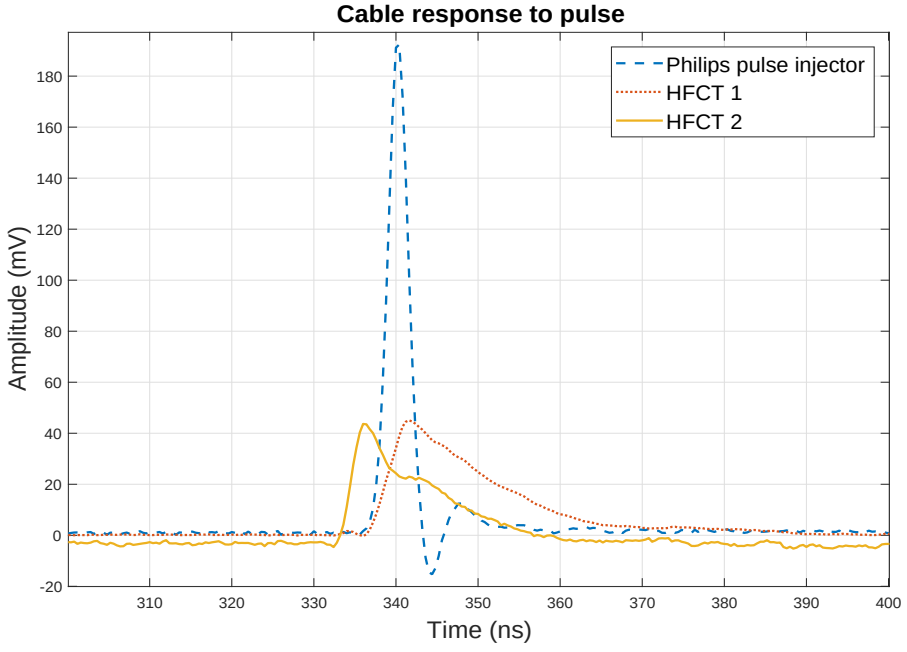

Figure 6.15: Pulse waveform of the Philips pulse injector on connection to the cable circuit

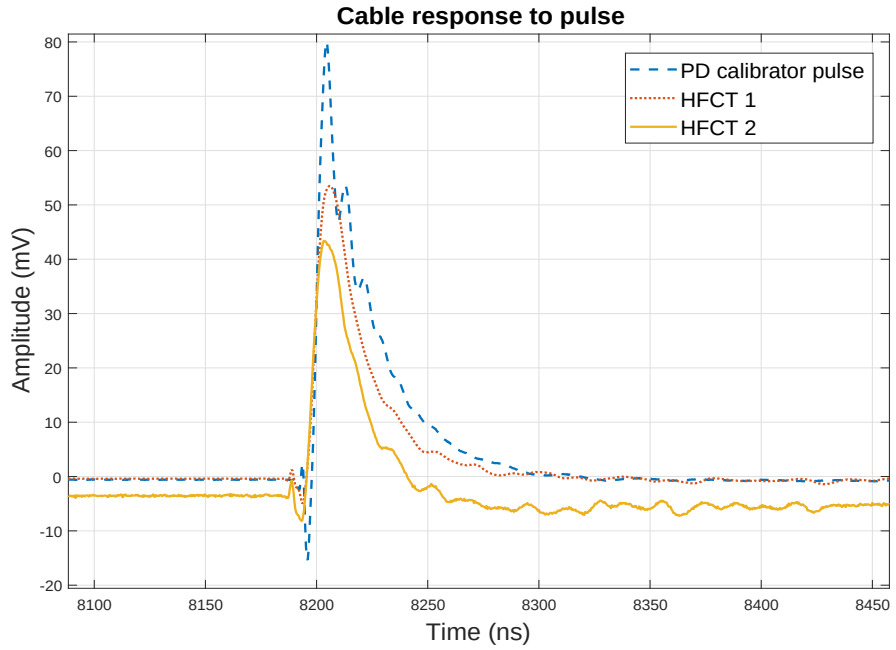

Figure 6.16: Pulse waveform of the PD calibrator on connection to the cable circuit

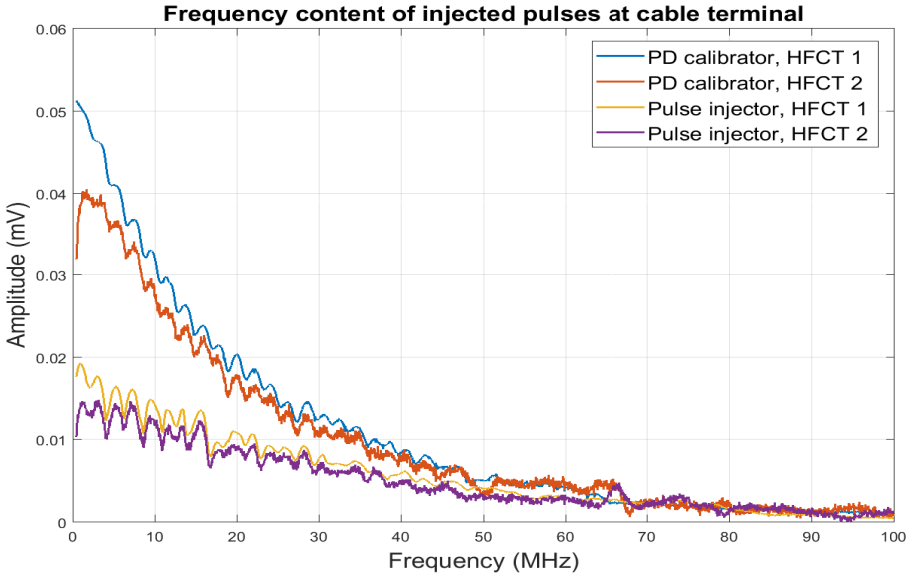

Figure 6.17: Frequency content of the voltage pulse at the terminals of the CBLUT

6.1.2 Measuring transfer function of the built-in capacitive sensor

The transfer function of the capacitive sensor (standard dimensions) constructed at 10 m is calculated experimentally by taking the ratio of the FFT of the output pulse at the sensor location to the attenuated pulse through the cable at 10 m.

$$TF(\omega) = \frac{V_o(\omega)}{V_i(\omega)} = \frac{FFT\ of\ output\ pulse}{FFT\ of\ attenuated\ injected\ pulse}$$

The injected pulse, attenuated pulse, and the pulse measured through the built-in capacitive divider along with their respective frequency contents are shown in Figure 6.18. The time shift of the pulses at 10 m reflect the propagation time of the cable.

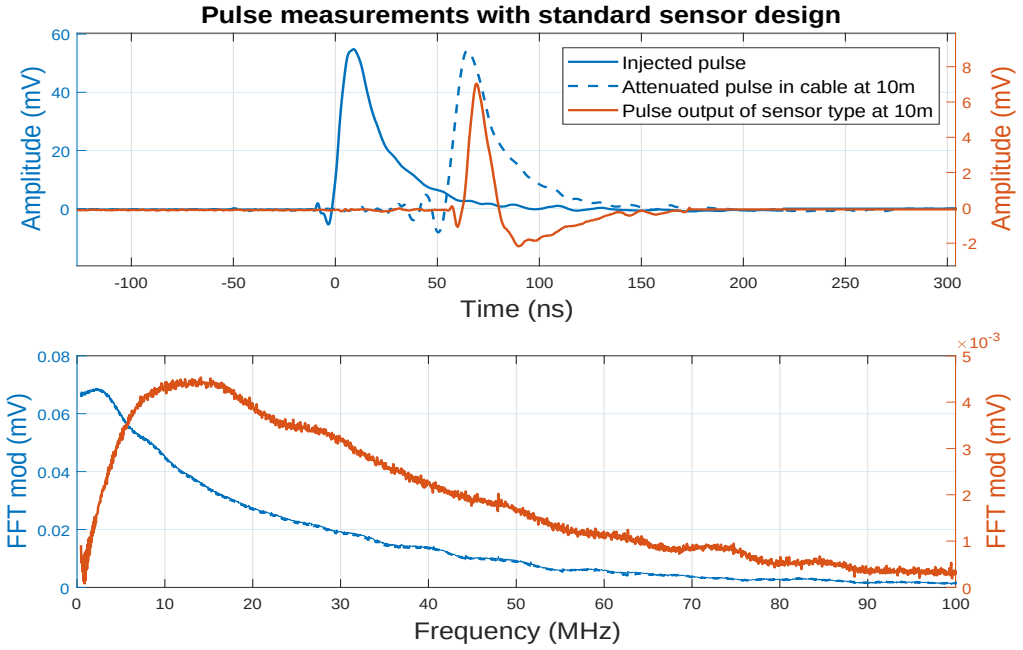

Figure 6.18: Pulse measurement with built-in capacitive sensor of standard dimensions

The transfer function of the standard capacitive sensor design is given in Figure 6.19. The transfer ratio determined through simulation is quite accurate when compared to the experimentally acquired results in the given frequency range (upto 50 MHz). Figure 6.19 also gives (in red) the frequency content of the partial discharge pulse at a distance of 100, 500 and 1000 m. This is indicative of which region of the

transfer function is more valuable with respect to the frequency content of the partial discharge pulse at various distances. Inferring from Figure 6.19, for PD detection upto 100 m from the source, detection at higher frequencies upto 50 MHz is possible. However for distances beyond 500 m, there is negligible frequency content above 20 MHz which renders the transfers at high frequencies rather futile.

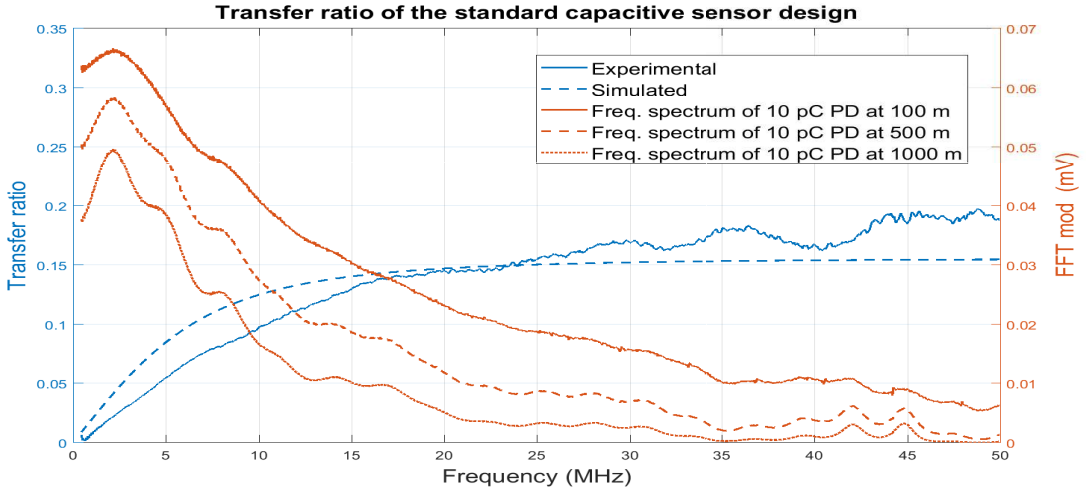

Figure 6.19: Experimental and estimated transfer function of the standard capacitive sensor

6.1.3 Calculating the sensitivity of the standard capacitive sensor

Since the objective of this project is to develop a sensitive (10 pC) PD measurement scheme. It becomes imperative to check the maximum output of the sensor towards a 10 pC partial discharge with varying distance. For this purpose a 10 pC discharge pulse is implemented as shown in Fig.6.20, with a 8 ns rise time and 100 ns pulse width. A large pulse width signifies a damped PD pulse, with limited higher frequencies. This is chosen in order to adopt a pessimistic approach while making estimates for sensitivity. The pulse propagation along the cable is simulated using the propagation constant determined experimentally. Using the transfer function obtained experimentally in the previous section the pulse outputs at various lengths away from the point of origin of PD is simulated and shown in Figure 6.21.

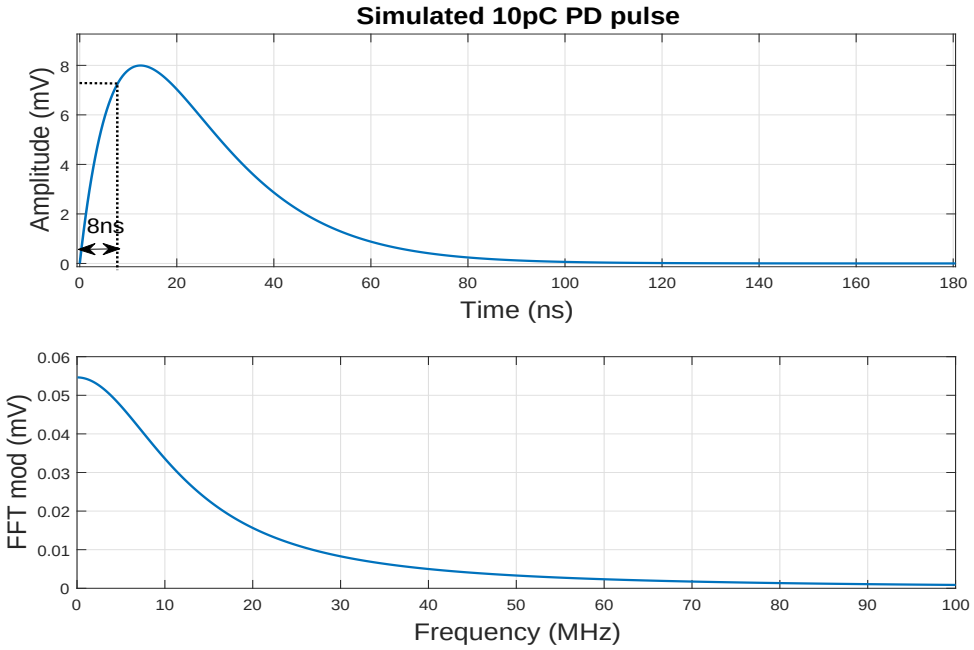

Figure 6.20: 10 pC Partial discharge pulse and its respective frequency content as used in the simulation to determine sensitivity of the standard capacitive sensor design

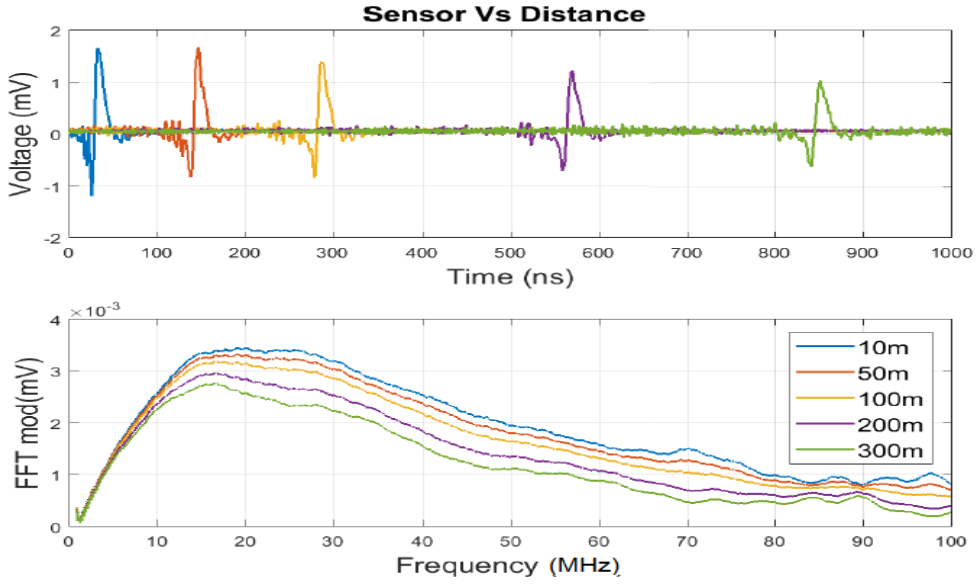

Figure 6.21: Output voltage of the standard capacitive sensor towards a 10 pC PD pulse with increasing distance from the source

(a) L=20 cm

(b) L=10 cm

Figure 6.22: Construction of the sensor with variable length of inner electrode

Based on Figure 6.21, it can be inferred that the peak voltage output of the standard capacitive sensor towards a 10 pC partial discharge pulse is ∼1 mV (1.25× noise floor; ref. Smart Cable Guard design) at a distance of 300 m from the source. However, in reality the noise threshold of the system when the cable is in operation determines this limit.

6.1.4 Varying the length of the inner electrode

The length of the inner electrode was varied in order to check the dependency of the parameter on the transfer ratio of the sensor design. Figure 6.22 shows the two different electrode lengths that were built during the tests. The dimensions of the new sensor were; L=10 cm, W=100% and insulation thickness=1 mm.

The transfer functions are calculated for this case and compared against both the results from the standard sensor design and the simulation results as shown in Figure 6.23. The analysis takes into consideration the frequency at -3 dB of the voltage output as it gives an impression of the slope of the curve. The -3 dB frequency doubles when the length of the electrode is halved. This is because the length of the electrode is directly proportional to the wavelength of reception of EM waves. Therefore, longer the length of the capacitive plate, greater is its ability to receive EM waves with longer wavelengths or lower frequencies. From a practical point of view, the manufacturing of a longer electrode is not a tedious task however, the smaller the components can be made, more cost-effective it will become.

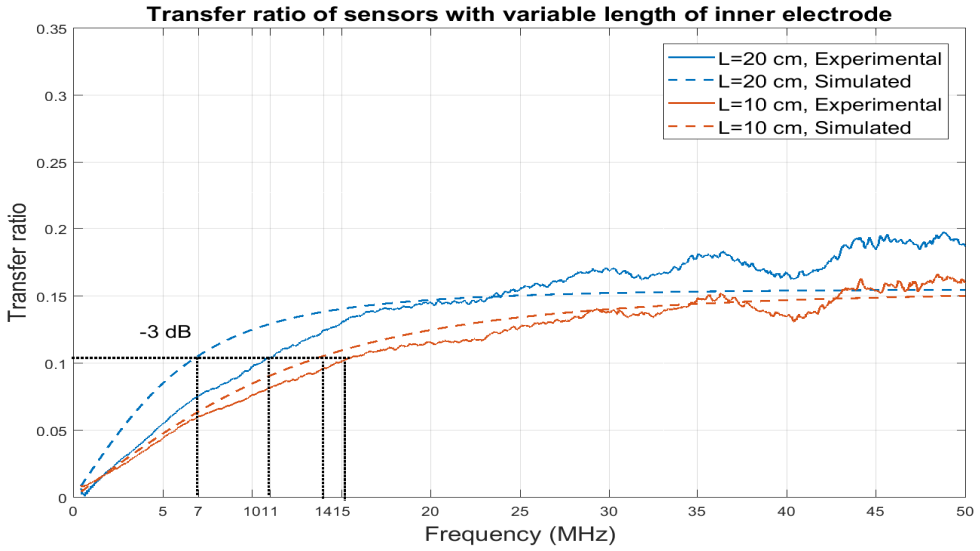

Figure 6.23: Transfer function of the sensors with variable length of inner electrode

6.1.5 Varying the width of the inner electrode

The width of the inner electrode was varied as a percentage of the circumference of the cable insulation screen. The standard capacitive sensor was built concentric around the cable, and hence is referred to as 100% of the circumference, the variant design was made with a inner electrode width of 25% of the circumference. The other parameters have been maintained constant (i.e. L=20 cm and ins.thickness=1 mm). The electrodes with variable width that were prepared can be seen in Figure 6.24.

The transfer function for this case is calculated and compared against the standard capacitive sensor design and the results from simulation. The reduction in area of the capacitive electrode leads to a drastic increase in the -3 dB frequency as shown in Figure 6.25. This is because the limited width of the electrode limits the voltage induced due to low frequency components. And hence only a restricted number of modes are accommodated in the electrode of reduced dimension when compared to the fuller electrode. Nevertheless, this means that the sensor would fail to benefit from the useful low frequency spectrum of the PD pulses.

Bearing in mind the aspect of large scale manufacturing of such units, it is more feasible to produce and install patch electrodes printed on insulating tapes and fitted over the insulation screen. Therefore, this analysis could be very useful in determining the trade-offs while making design decisions on the final sensor dimensions.

(a) W=100%

(b) W=25%

Figure 6.24: Construction of the sensor with variable width of inner electrode

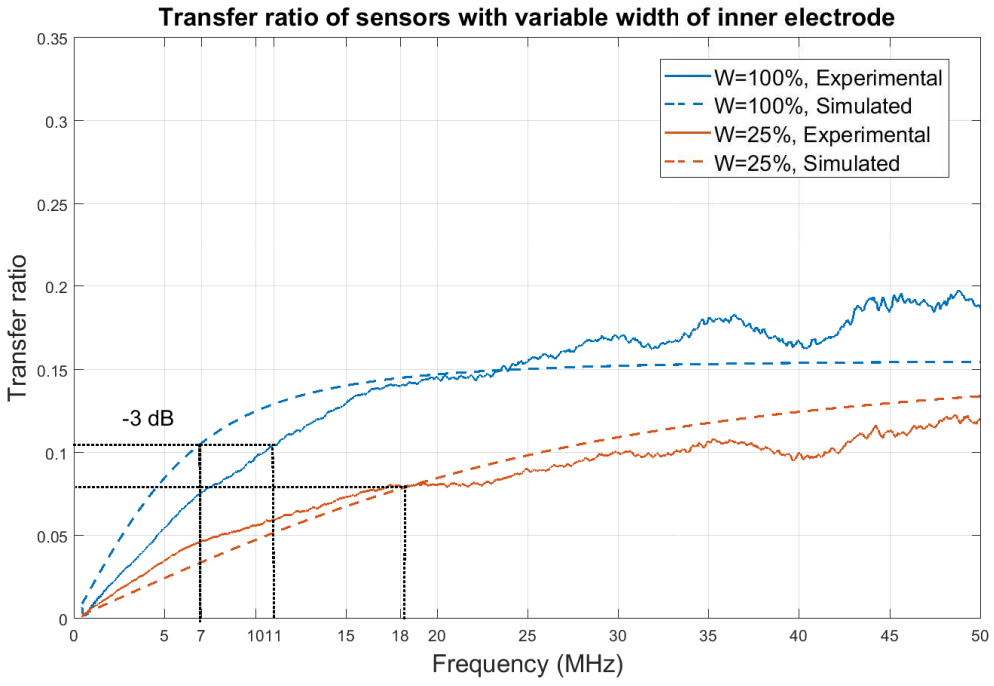

Figure 6.25: Transfer function of the sensors with variable width of inner electrode

6.1.6 Varying the thickness of insulation

The thickness of insulation directly influences the capacitance of the divider circuit. Since thickness of insulation (of the sensor) is a parameter that is related to the capacitance of the sensor alone and not to the cable layers unlike the length and width, its change has a considerable effect on the output. There is a direct reduction of the maximum transfer ratio to half when the thickness is halved. This follows the Eq.6.5 where the the reduction in thickness is represented by a reduced ratio of the outer and inner radii (given by b and a respectively).

$$\triangle V = \frac{q}{2\pi\epsilon_0} ln(\frac{b}{a}) \tag{6.5}$$

As seen from Figure 6.26 the transfer ratio reduces with reduced thickness of insulation and also the -3 dB frequency recedes to the lower frequencies. In other words, the sensor performs closely with the standard sensor design at the frequencies lower than 10 MHz but at higher frequencies the transfer ratio is half the transfer ratio offered by the standard sensor. Therefore, this could also be a good analysis to determine trade-offs in the design.

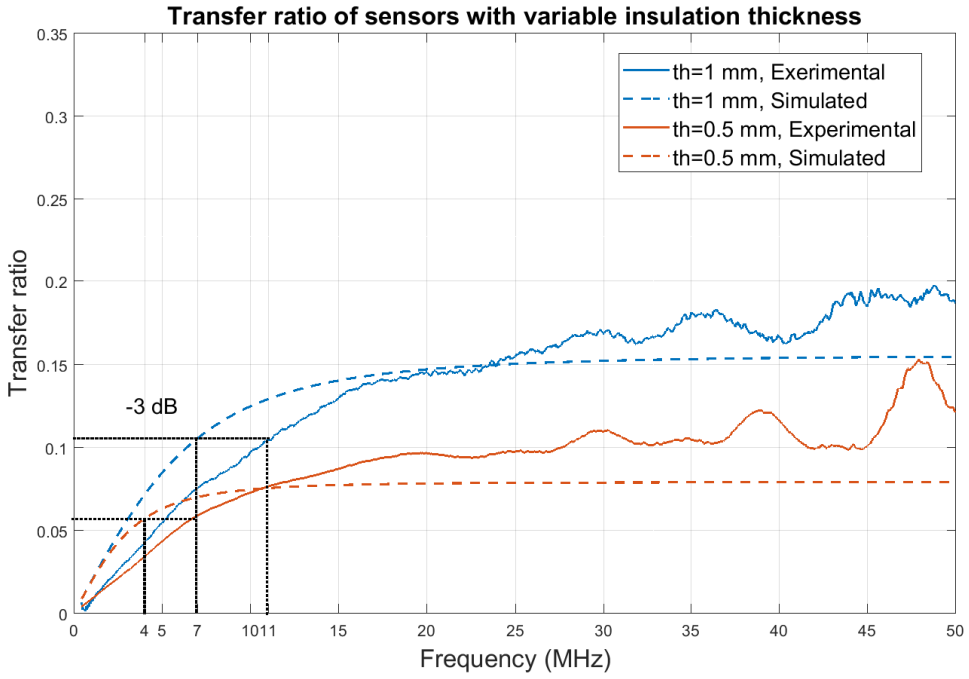

Figure 6.26: Transfer function of the sensors with variable insulation thickness

Conclusion on parameter variation of built-in capacitive sensor

The influences of variation in design parameters is studied in the previous sections. The objective of this study is to provide insight into the sensor performance with different designs so that the best combination can be selected. The absolute best performance is obtained with the standard sensor design (of L=20 cm, W=100% and th=1 mm). However, from the viewpoint of their practical implementation, a patch electrode (W<100%) is easier to produce and integrate into the cable. Its performance is inferior to the standard sensor design at lower frequencies but at higher frequencies they behave close to each other. Therefore, a partial inner electrode with reduced width could be a possible substitute to a fully concentric electrode.

6.1.7 Measuring with multiple sensors

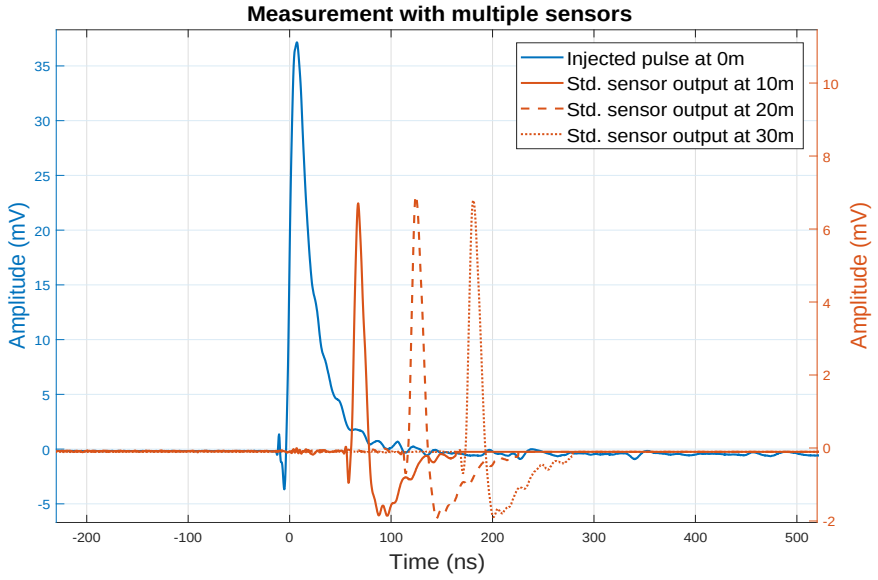

Figure 6.27: Measurement with multiple capacitive sensors of the standard design dimension at 10, 20 and 30 m.

The measurements using multiple sensors were performed to check the compliance of such a system to work at multiple locations on the same PD pulse with the same transfer function. In a lossless system it could be expected that the the same PD pulse could me measured multiple times before the energy in the pulse becomes insufficient. However, in reality the attenuation of the cable to PD pulses plays a greater role in determining this limit.

Figure 6.27 shows the results of measurement with multiple capacitive sensors of the standard design dimension built at 10, 20 and 30 m. The magnitude of the output pulses is observed to be precisely constant with distance. This is because the maximum transfer ratio of the sensor is only 15% , which means that only 2.25% of the energy at the specific frequency band is transferred over its output.

(Since energy=V^2/R, Transfer coefficient in terms of energy= 0.15×0.15=0.0225→ 2.25%)

Hence, several sensor units placed along the coaxial cable can measure the same PD pulse (if the cable is assumed lossless). This section reaffirms that the sensor by itself does not alter/have an effect on the propagating partial discharge pulse.

6.1.8 50 Hz test on the standard capacitive sensor

In the real system partial discharges will occur alongside the operating 50 Hz voltage. Which also means that the sensor has to sense the 50 Hz fields constantly irrespective of whether or not partial discharges occur. Therefore, careful consideration needs to be taken to make sure that the capacitive divider does not offer a high transfer towards the 50 Hz signals. If this would be the case, then expensive electronics for filtering would be essential. Therefore, a simple test is designed to check the sensitivity of the developed sensor towards 50 Hz voltage. The corresponding scheme for the test is shown in Figure 6.28.

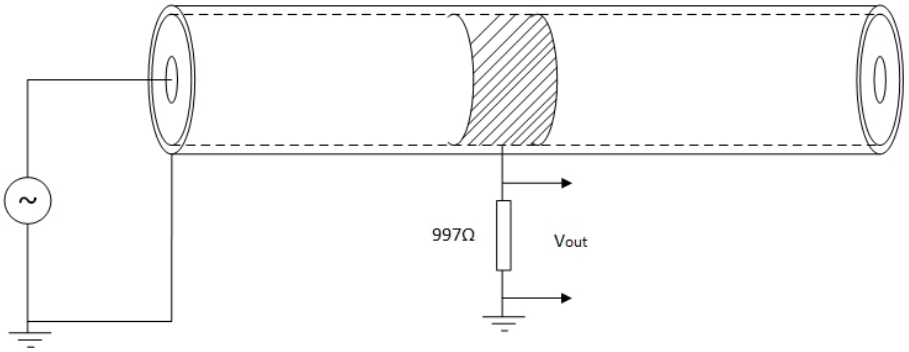

Figure 6.28: Schematic of the 50 Hz test performed on the standard capacitive sensor

An AC transformer with a maximum voltage limit of 50 kV was used alongside a variac to control the AC voltage feed to the test cable. A voltage probe on the HV side of the test set-up was connected to monitor the voltage and all connections to ground were securely made. A sensitive voltmeter was connected across the resistor

of 1 kΩ that was connected between the inner and the outer electrodes to check the voltage drop across the sensor. The values obtained are listed in Table 6.2.

The results of the test show that in case the capacitive divider has a sensitivity of 0.1 mV/kV towards 50 Hz voltage if the output is obtained across a 50Ω measuring impedance. This estimate would be useful during the final design phase of the sensor, since a high measurement impedance across the sensor output terminals would lead to a very high voltage transfer at 50 Hz.

Table 6.2: Results of the 50 Hz test performed on the standard capacitive sensor

AC voltage on CBLUT	**Voltage across 1 kΩ**
1 kV	0 mV
2 kV	4 mV
3 kV	5 mV
4 kV	6 mV
5 kV	8 mV
4 kV	7 mV
3 kV	6 mV
2 kV	5 mV
1 kV	3 mV

6.2 Antennas in power cables

The application of antenna like transceivers was tested experimentally during this master thesis project. Various antenna designs were experimented with during the process, some of which are shown in Figure 6.29. The results of the tests are presented in the forthcoming section.

6.2.1 Consolidated list of antenna designs tested experimentally

Table 6.3 gives a list of antennas that were tested experimentally during the master thesis. Their resonant frequencies in free space and when inserted inside the cable (under the earth screen) were measured using the Vector Network Analyser (VNA). These are subject to small variations with changes in the structure of the cable earth screen. This is because the metallic earth sheath serves as a perfect electric

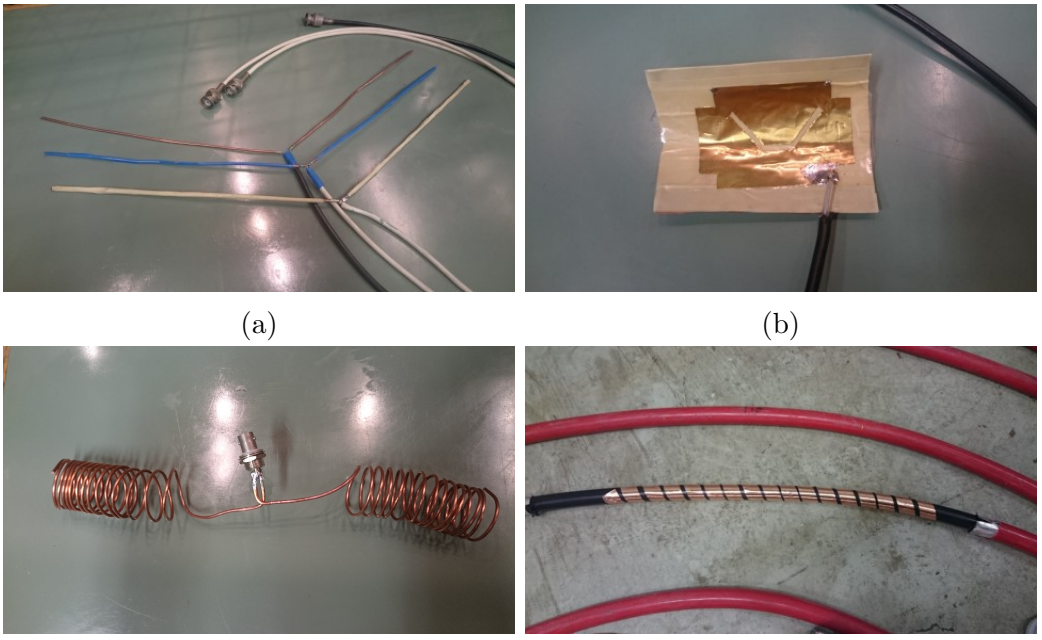

(a) (b)

(c) (d)

Figure 6.29: Antenna designs tested experimentally (a) Short dipole antennas with an arm length of 21.6 cm (b) Patch antenna with dimensions 7.9×11.2 cm (c) Long dipole antenna with an electrical length of 1.5 m (per pole) wound in the form of a coil (spiral) (d) Patch antenna with dimensions 1.5 m$\times$2 cm built in the form of a spiral around the cable

conductor with zero component of tangential electric field. And hence the structure and the closeness of this metallic earth sheath would dictate how the fields from the antenna are oriented. Therefore, extreme care is taking while reconstructing the metallic earth sheath to keep it uniformly coaxial as much as possible. Table 6.3 gives an exhaustive list of all the designs that were tested, the most relevant results based on which important conclusions are drawn are discussed in the forthcoming sections.

6.2.2 Dipole Antenna

A dipole antenna works based on the voltage drop that occurs across its arms, a more detailed working principle is discussed in Appendix B. It is very attractive for this application due to the simplicity in its construction. A range of dipole antennas were built and tested experimentally by including them under the earth screen of the cable. Figure 6.29a shows one such dipole that was built with a quarter

Table 6.3: Antenna types investigated

Antenna design	**Dimensions**	**Resonant freq. in free space**	**Resonant freq. in the cable**
Short dipole	2×21.6 cm, ϕ 2 mm	347 MHz	∼300 MHz
Short patch	7.9×11.2 cm	1.7 GHz	∼1.3 GHz
Long patch	1.5 m×2 cm	Unknown	∼700 MHz
Long dipole A	2×1.5 m, ϕ 2 mm	50 MHz	∼20-25 MHz
Long dipole B	2×2 m, ϕ 2 mm	37.5 MHz	∼20 MHz
Long dipole C	2×2 m, ϕ 1 mm	37.5 MHz	∼10,30 MHz
Long dipole D	2×3 m, ϕ 1 mm	25 MHz	∼30 MHz

wavelength of 21.6 cm which corresponds to a resonant frequency of 347 MHz in free space. The antenna poles were wound with PE tape and paper tape in an attempt to scale down the resonant frequency to below 100 MHz. However, this method was unsuccessful since it requires the antenna to be placed in a medium of a different permittivity altogether and a thin layer of coating does not change much as the effective permittivity of the medium still remains close to 1 (ϵ_r of air). Therefore, longer dipole antennas with a quarter wavelength of 1.5 m were constructed, which corresponds to a resonant frequency of 50 MHz in free space. However, it can be conjectured that it is close to impossible to handle such a long antenna. Therefore, the antenna was wound in the form of a coil and fixed around the cable as shown in Figure 6.30. This maintains the electrical length of the antenna constant while reducing its mechanical length. Hence, the radiation pattern of the antenna remains unchanged.

The resonant frequency of the long dipole A (ref. Table 6.3) was measured using the VNA after mounting it over the cable. The antenna resonated between 20-25 MHz. However, further tests relating to the transfer function couldn't be accomplished using the Network analyser due to three main drawbacks. Firstly, the network analyser uses sinusoidal pulses to acquire the reflection parameters, in case of which it was very difficult to find any error in the set-up due to external interference, reflections and standing waves. Secondly, the high impedance of the antenna port was not accounted by the network analyser since the antenna was connected to the VNA through a measuring cable (eg. RG58), and the use of measurement cables was unavoidable. Lastly, the travelling pulse was required to be compensated for the attenuation in the cable. However, as the antenna was mounted in the middle of the cable circuit it was not possible to calibrate just the half length of the cable. Though it was tried by calibrating the whole length of the cable, the magnitudes deduced were incorrect.

(a) Dipole antenna wound around the cable

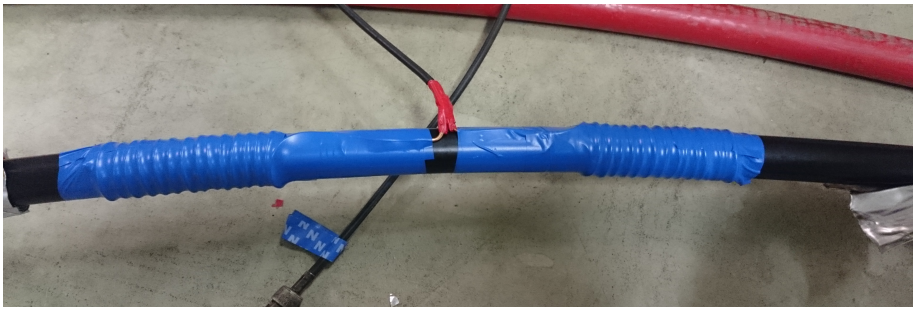

(b) Insulating the antenna to prevent short-circuit with the earth screen

(c) Reconstruction of the metallic earth screen

Figure 6.30: Stepwise construction of the long dipole antenna wound on the cable

Therefore, a new approach was adopted by using a waveform generator and a oscilloscope instead of a VNA. The schematic of the set-up and connections is shown in Figure 6.31. Both cable ends were terminated with the characteristic impedance to make the CBLUT appear as an infinite line (with no reflections). Special electromagnetically shielded boxes with feed-through were used to remove external noise. Pulses were injected at the antenna port and measured at the cable end using the oscilloscope and vice versa. The measurement procedure is described in the following section.

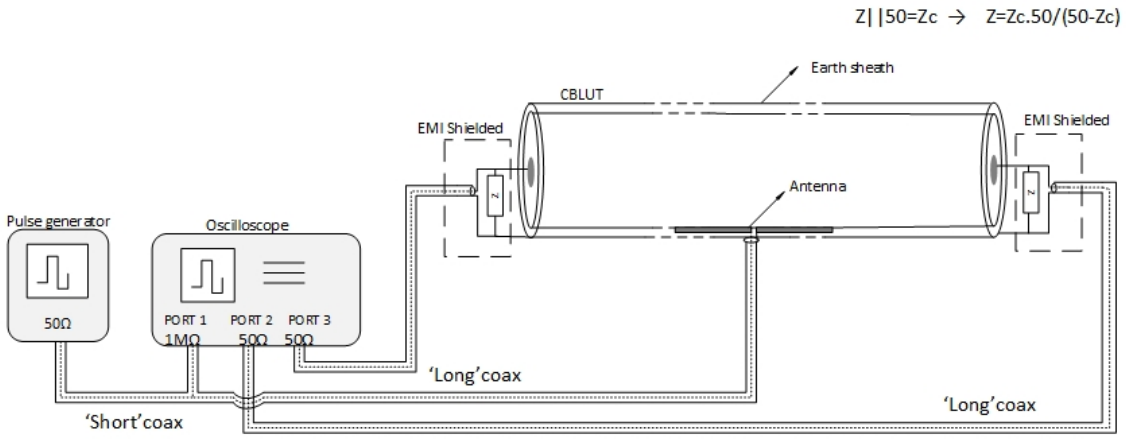

Figure 6.31: Schematic of the measurement setup with antennas

Dipole antenna as transmitter

The pulse waveform used for the measurements had a flat frequency spectrum upto 67 MHz as shown in Figure 6.32. As presented in the previous section with measurement on capacitive sensors, first, the attenuation in the measuring cables is recorded. The cables are short circuited and the ratio of the injected and reflected pulses is calculated; $H_{inj} = V_r/V_i$. Then the measuring cable is connected to the antenna which is mounted inside the cable (below the metallic earth screen) and the ratio of the injected and reflected pulses is recalculated, given by $H_1 = V_{r1}/V_i$. The impedance of the antenna can then be deduced through the expression

$$Z_a = Z_{meas}.[\frac{H_{inj} + H_1}{H_{inj} - H_1}] \tag{6.6}$$

where, Z_{meas} is the characteristic impedance of the measuring cable. In this case, the reflection coefficient at the antenna input port is positive which means that the impedance of the antenna port is higher than the impedance of the measuring cable (50 Ω). The experimentally obtained result indicate that the input impedance of the antenna is ∼150 Ω, it is as shown in Figure 6.33

The voltage over the antenna ports is calculated based on the voltage transmission coefficient of the antenna given by Eq.6.7, and shown in Figure 6.34.

$$\Gamma = 1 + H_1 \tag{6.7}$$

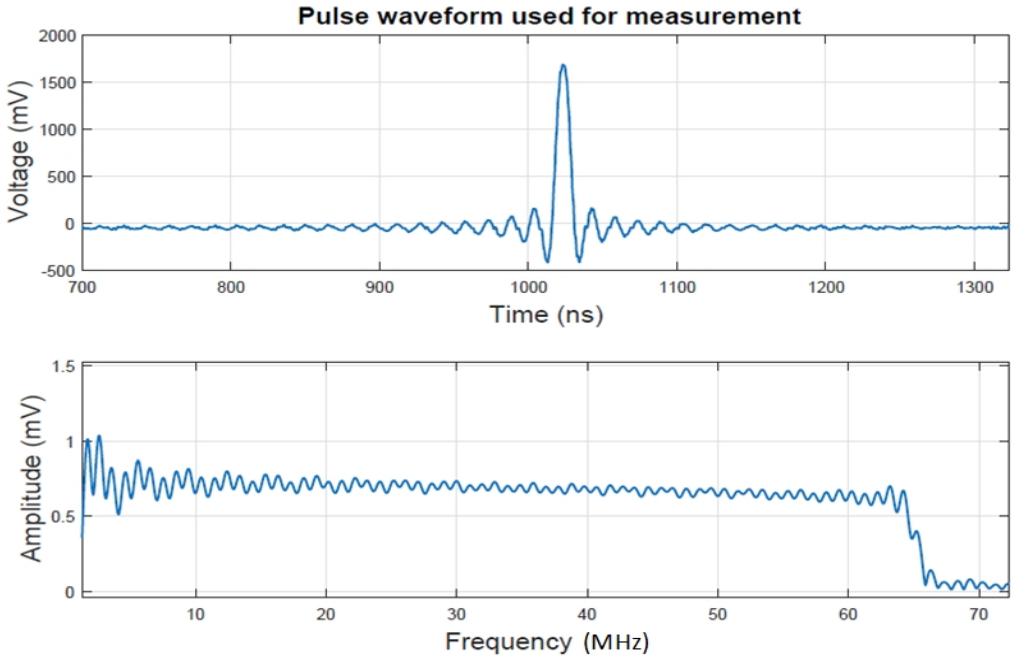

Figure 6.32: Pulse waveform used for the antenna measurements in time domain (top) and frequency domain (bottom)

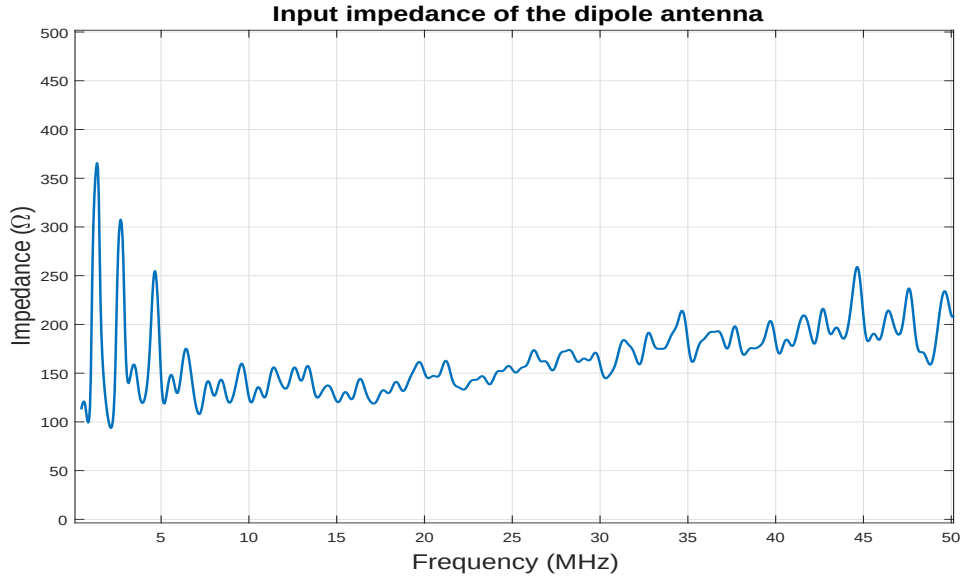

Figure 6.33: Input impedance of the dipole antenna placed inside the cable obtained experimentally

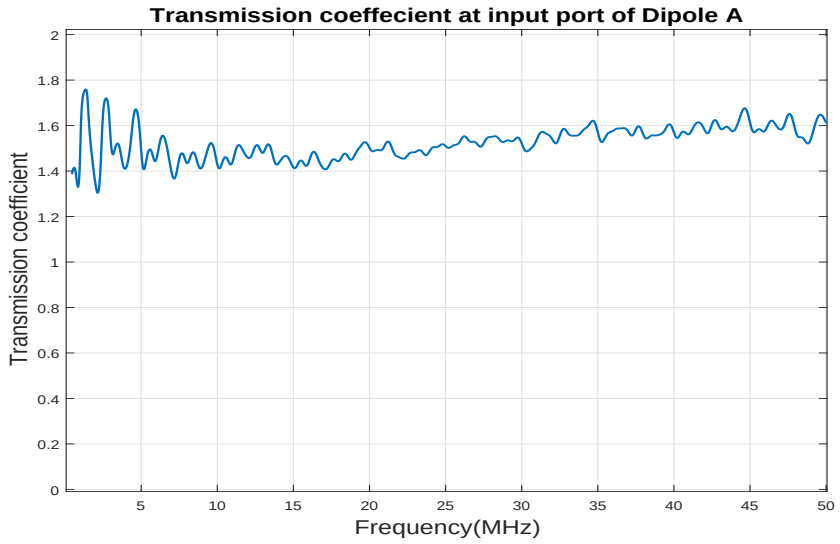

Figure 6.34: Voltage transmission coefficient from the measurement cable to the dipole antenna obtained experimentally

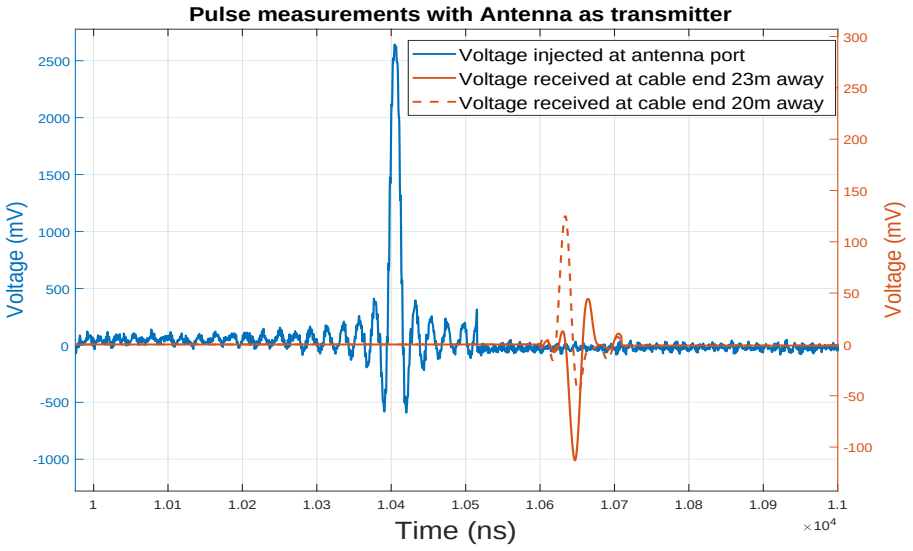

Figure 6.35: Pulses measured with dipole antenna A as a transmitter

The pulses measured at the cable ends are compensated for the attenuation along the cable through the propagation constant calculated and presented in Figure 6.6. The final result of the measurement is shown in Figure 6.35. The output pulses measures at the two cable ends are oppositely polarized since they represent two different

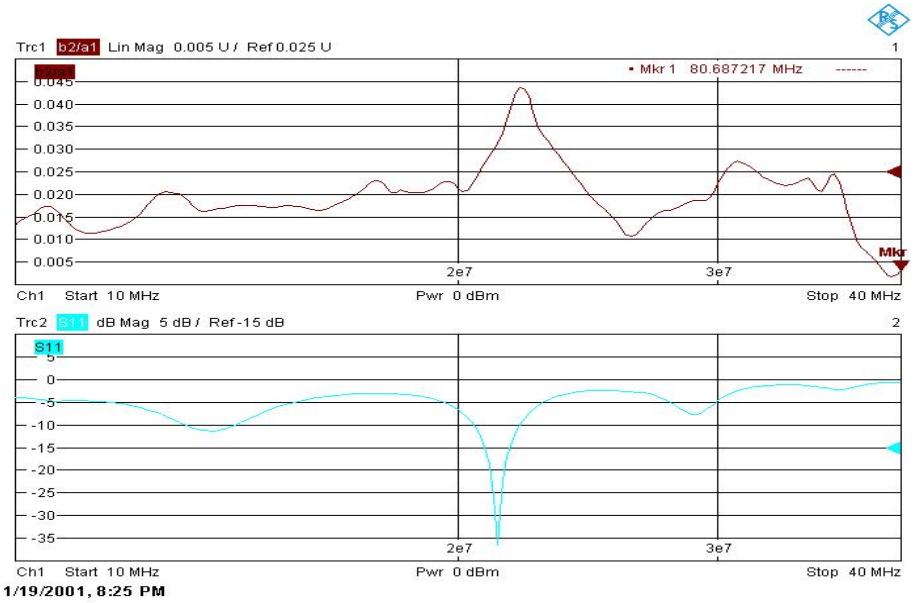

Figure 6.36: The transfer coefficient between the antenna and the cable (top) and the reflection coefficient at the antenna port (below) measured using the VNA

propagating waves travelling in opposite directions from the point of injection. In order to show the relationship between the transmission peaks and reflection peaks, a screen shot from the VNA is shown in Figure 6.36. This confirms that the coupling between the antenna and the power cable is certainly due to antenna radiation because the energy is transferred in the same frequency band in which the antenna resonates. The transfer coefficient of the dipole antenna A is obtained by taking the ratio of the FFT of output pulse at the cable end (after compensating for the attenuation) over the FFT of the voltage waveform across the dipole antenna.

In an attempt to make the set-up more compact, dipole antenna with a pole diameter of 1 mm were tested (2 mm was used earlier) . Dipoles with dimensions of 2×2 m and 2×3 m listed as dipole C and D respectively in Table 6.3 were built and the results of all the alternatives tested are presented in Figure 6.37. Scientifically, when the thickness of the dipole is reduced, the bandwidth reduces and the resonant frequency increases. This is because the degrees of freedom of the current through the dipole becomes limited and as a consequence only a limited number of modes can be supported. There is also a minor reduction in the radiation intensity associated with it. This could be reasoned on the different conductivity of the two wire antennas. Antennas A and B were built using copper wires. Whereas, antennas C and D were made with an alloy of Zinc-Chromium which has considerably lower conductivity compared to the former. However, the clear shift in the resonant frequency and

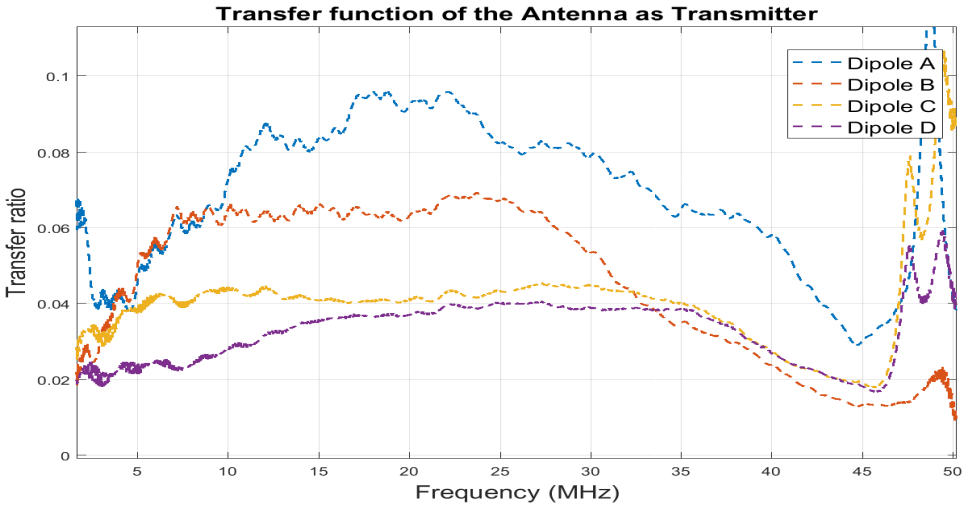

Figure 6.37: Transfer function of the dipole antenna placed inside the coaxial cable functioning as a transmitter

variation in the bandwidth can be seen in the plot of reflection coefficient measured using the VNA shown in Figure 6.38.

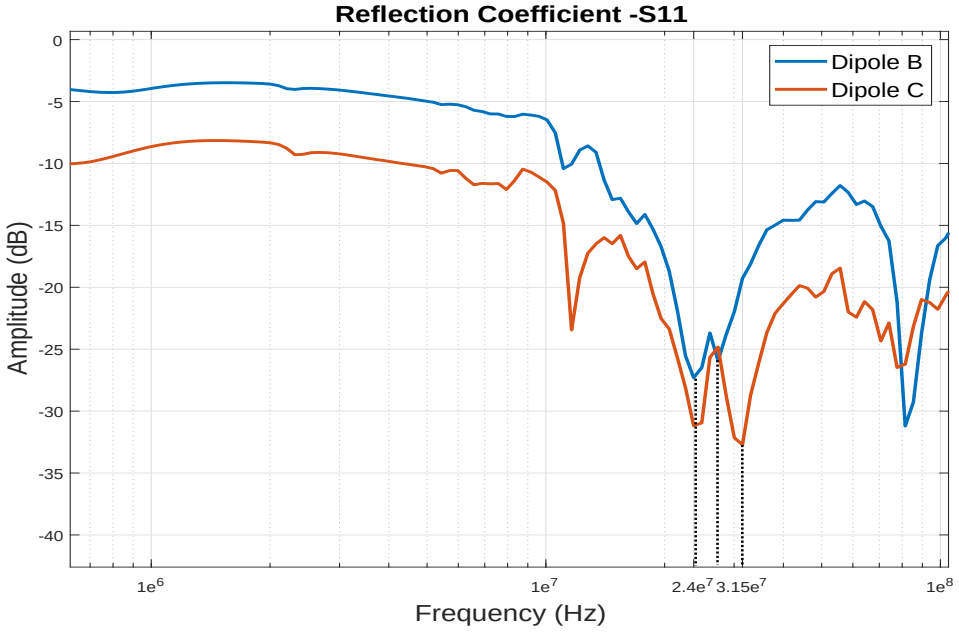

Figure 6.38: Reflection coefficient (S11) of the dipole antennas placed inside the power cable, measured using the VNA

Dipole antenna as Receiver

The dipole antenna is also tested as a receiver, by injecting a pulse at the cable end and measuring at the antenna terminals terminated at 50 Ω. The injected pulse is multiplied by the transmission coefficient from the measurement cable to the power cable given by Eq.6.8. This is made possible by measuring the input impedance of the cable port using pulse reflection method. Similarly, the received pulse at the antenna post is divided by the transmission coefficient from the antenna to the measurement cable given by Eq.6.9. The injected pulse is also compensated for the attenuation in the power cable from the cable end to the antenna location. Finally, the transfer function of the system is derived and it is as shown in Figure 6.39.

$$\tau_{cable} = \frac{2 * Z_{CBLUT-input}}{Z_{CBLUT-input} + Z_{meas}} \tag{6.8}$$

$$\tau_{antenna} = \frac{2 * Z_{meas}}{Z_{meas} + Z_a} \tag{6.9}$$

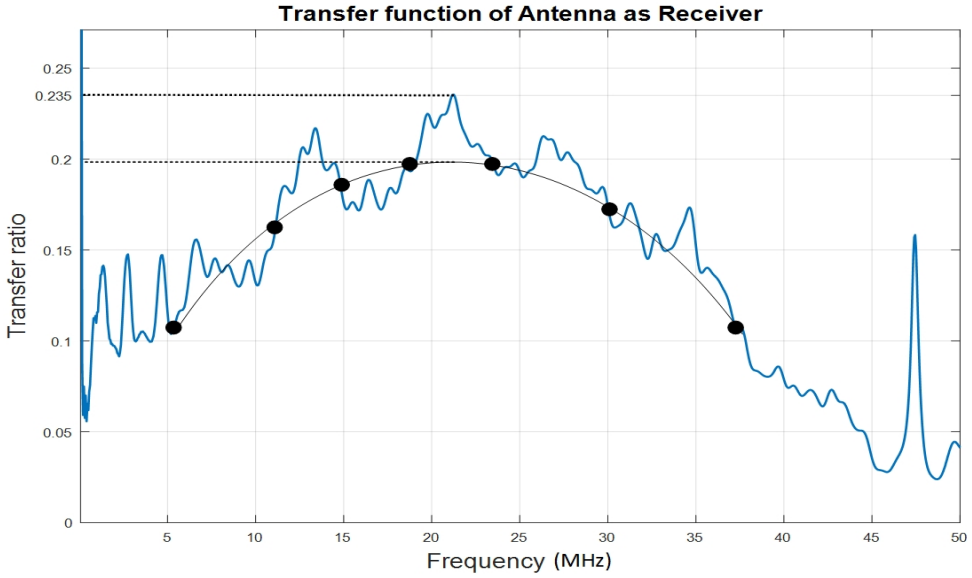

Figure 6.39: Transfer function of the dipole antenna A placed inside the coaxial cable functioning as a receiver

The maximum transfer coefficient of the system working as a receiver is precisely twice as that measured with the dipole as a transmitter. The reason here being,

when the dipole antenna is functioning as a transmitter, injecting energy into the cable. A set of two propagating EM waves are excited. These two propagating waves travel opposite to each other from the point of injection towards the cable ends. This is what we see in Figure 6.35 with the pulses of opposite polarity given in red. This also means that the energy is split into two channels giving rise to two sets of TEM waves. However, in case of the antenna working as a receiver, there is only one TEM wave, which is the TEM wave of the power cable. And the energy transfer to the antenna is derived from this alone. Therefore, this is the reason the transfer coefficient of the receiver system is twice that of the transmitter system.

6.2.3 Patch Antenna

A patch antenna is more suitable for this application given the fact that the electric field is co-polarized along the axis of reception of the patch. The detailed working of such an antenna is given in Appendix B. The first model was built with dimensions of 7.9×11.2 cm as shown in Figure 6.29b. The resonant frequency of this design

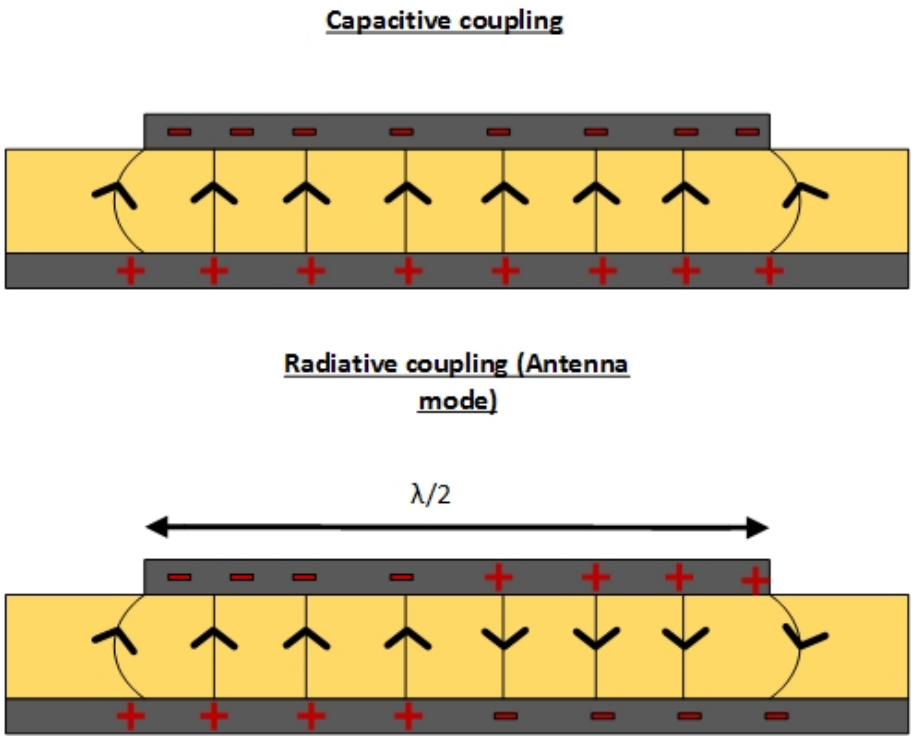

Figure 6.40: Patch antenna behaviour outside the resonant bandwidth (top) and at resonance (bottom)

was in the order of GHz when inserted inside the cable and from this it can be concluded that it is not suitable for this application. In order to build a resonant patch antenna for the 50 MHz range we would require a 2×2 m wide patch. But since the width of the patch is limited by the circumference of the cable, a different alternative was tested, a long patch antenna with dimensions 1.5 m×2 cm (simulated in Section 3.2.3). The idea was to test the patch at resonant frequency when the patch is functioning based on the antenna theory of radiation and not capacitively. The difference between the performance of a patch antenna inside and outside its resonant modes is shown through Figure 6.40. In case of capacitive coupling of the patch antenna with the TEM waves of the coaxial cable the displacement current between the patch and the ground plane defines the output of the patch antenna. While, in case of radiative coupling as in the antenna mode of operation, at resonance frequency. The voltage wave of half wavelength (from the cable) induces charges that are of opposite polarity along the length of the patch. The resultant fringing electric fields at the edge of the patch add up in phase to give a net non-zero voltage. This defines the operation of the patch as a receiver. In case of a transmitter, the net voltage produces the radiation of the patch antenna.

The spiral patch antenna as shown in Figure 6.29d was constructed on the cable with copper tape. The VNA was used to test the resonant characteristics of the design. The reflection coefficient of the antenna design showed that the antenna

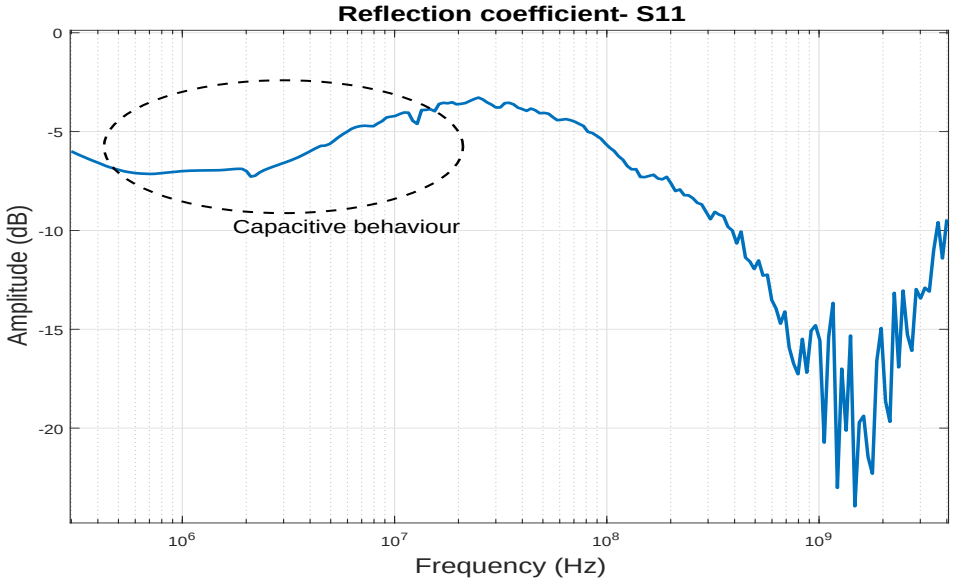

Figure 6.41: Reflection coefficient (S11) of the spiral patch antenna measured using the VNA

resonates at frequencies higher than 700 MHz as shown in Figure 6.41. The dip at lower frequencies indicates a capacitive behaviour. Thus, it could be inferred from this test that resonant patch antennas couldn't be implemented for this application and only sub-resonant patch antennas could be constructed. In other words, this is nothing but a test on a capacitive sensor used as an injector, to inject pulses into the cable.

An approach similar to the ones performed in the earlier sections is adopted to obtain the transfer coefficient of the system. Since the patch antenna has already been tested as a receiver in Section 6.1, its performance as transmitter is presented in Figure 6.42.

It is observed that there is an appreciable transfer at the frequencies outside the resonant peak. But it should be noted that this is not due to the resonant behaviour of the antenna but due to the the capacitively coupled voltage. Another important observation that can be made is the maximum transfer of 8% when the capacitive sensor is functioning as a transmitter/injector, in contrast to a transfer of 15% when it was tested as a receiver (under Section 6.1). This is due to same reason as explained with the dipole antenna, since the energy is split to excite two TEM waves in case of operation as a transmitter.

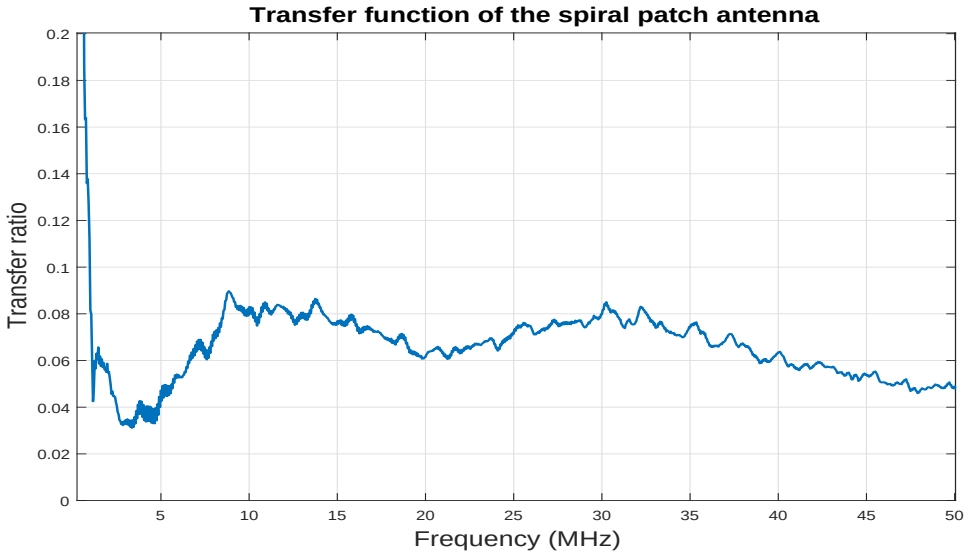

Figure 6.42: Transfer function of the spiral patch of dimensions 1.5 m×2 cm functioning as a transmitter

6.2.4 Comparing sensitivity of Dipole and Patch antennas

There are two competing scenarios that are being studied;

- First, a resonant dipole antenna which is cross-polarized to the E-field of the TEM mode of the power cable. Though its performance is suboptimal, it is relatively easy to make a dipole antenna as big as possible so as to resonate at the frequency of interest.
- Second, a sub-resonant patch antenna which is co-polarized to the E-field in the power cable, and has the ability to perform better than the dipole antenna. However, it is not possible to make it resonate at the frequencies of interest due to reasons sighted earlier.

This section will analyse the two scenarios in detail to arrive at a conclusion of sorts.

Antennas for communication (only)

While implementing a communication system with antennas, a narrow frequency band is preferred around the resonant frequency. This allows for superior SNR. Additionally, in case of a contingency such as a fault or lightning strike, the voltage at the antenna ports will be negligible (given that the sensor unit is sufficiently far away from the point of failure) since most of the higher frequencies are drastically attenuated with distance.

Based on the voltage distribution in the cable layers at 50 Hz, an average electric field of roughly 4 V/mm is present across the outer semiconducting layer. Assuming that this provides an opportunity to harvest roughly a few 100 mW of power locally, and that a voltage of 1 V is available at the beginning of the communication stage. The range of the system is estimated in Table 6.4. Efficiency of each hop refers to the ratio of output at the receiver to the input at the immediate (next) transmitter. Therefore, based on this efficiency, SNR (Assumption: SNR =10, voltage output of 10 times the noise floor levels as stated in Table 6.4) and the attenuation in the cable at 25 MHz (operating frequency of the antennas), a maximum range of communication is derived.

Antennas for PD sensing and Communication

The possibility of using antennas for both PD sensing and communication is certainly a compelling concept. From the results presented in Section 6.2 it is evident that the frequency spectrum of reception and transmission of the antennas is relatively

Table 6.4: Antenna performance as a transceiver

	Transmitter	**Receiver**	**Efficiency of each hop**	**Max.Distance***
Dipole Antenna	10%	20%	2% (-34 dB)	425m (-8.5 dB)
Patch Antenna	8%	15%	1.2% (-38 dB)	301m (-6 dB)
*With cable attenuation of 0.02 dB/m at 25 MHz Noise floor of 25 μA/ 0.75 mV (ref. DNV GL's field measurements)				

broadband and hence can be adapted towards functioning as a PD sensor as well. Since the sensitivity analysis of the patch antenna (capacitive sensor) was already discussed in Section 6.1.3, the sensitivity of the dipole antenna towards a 10 pC pulse is presented through Table 6.5. Results indicate that the dipole antenna can detect a PD of 10 pC magnitude, 300 m away from its source giving a maximum voltage output of 3.75 mV.

Table 6.5: Sensitivity of the dipole antenna towards a 10 pC PD pulse

	Dipole antenna
Sensitivity	10 pC
Max. voltage Output	3.75 mV
Range	300 m
SNR	5*
*Noise floor of 25 μA/ 0.75 mV (ref. DNV GL's field measurements)	

From this section, it is clear that the performance of the resonant dipole antenna, is marginally better than the sub-resonant patch antenna (capacitive sensor). Additionally, the dipole antenna is also easier to manufacture and build over the cable in contrast to the patch antenna.

6.3 Conclusion

In this chapter two concepts have been established and quantified. One, the performance of a built-in capacitive sensor and two, the performance of antennas inside power cables. Based on the results and detailed analysis on the two subjects as presented in the previous sections, the following conclusions can be made:

1. The wideband capacitive divider can be used for sensitive PD measurements over a long range of frequencies. There is also a possibility to position the

sensor close to the PD source and use its transfer coefficient at higher frequencies as this would help eliminate the problems of noise which is pervasive at the lower frequency bands. Though, the peak voltage output of the sensor towards a 10 pC PD pulse, 300 m away from the source is only ∼1 mV, its wide bandwidth provides a possibility for better reconstruction of the PD pulse waveform. Furthermore, the simple construction of the sensor unit provides an additional benefit from the prospect of manufacturing.

2. The performance of the dipole antenna is promising both as a communication unit and as a PD sensor. The ability to build and integrate a dipole antenna as long as possible, provides an opportunity to exploit the high coupling coefficients at the resonance band of the antenna. As a communication unit, it can achieve an estimated maximum range of 425 m (a maximum output of 7.5 mV after one hop/relay if the input voltage to the communication unit is assumed as 1 V). Likewise as a PD sensor, the dipole antenna can achieve a peak voltage output of ∼3.75 mV for a 10 pC PD pulse, 300 m away from the source. Which is marginally better than the performance of the capacitive divider. However, the absence of a flat and wide frequency bandwidth prevents the accurate reconstruction of the PD pulse waveform. Nevertheless, on all other respects, research so far indicates that the dipole antenna has an overall promising performance.

CHAPTER

7

CONCLUSIONS AND RECOMMENDATIONS

7.1 Conclusions

PHASE I

In phase I of this master thesis the feasibility of sensitive partial discharge measurements in power cables was studied. Various techniques were explored by analytical estimations using simulation tools such as COMSOL and MATLAB. From the results, it was concluded that the well-established electrical methods of PD sensing namely the capacitive and inductive methods are the most reliable and suited for application in power cables. However, since the sensitivity of these systems is very poor with measurement at cable ends, the sensors were opted to be built at distributed locations, embedded into the cable (under the metallic earth earth screen and above the extruded semiconducting layer). Nonetheless, the implementation of distributed sensors comes with an added challenge, which is to communicate the measured data to the cable end/substation. Therefore, to provide a solution for the problem of communication, antenna designs were researched and their working concept was studied using COMSOL simulations.

Based on all the estimations made via simulations in Phase I of the project a novel PD sensing scheme was derived and presented in Chapter 4. The scheme was based on the working principle of a RFID tag. It fulfilled the objective of communication between the built-in distributed sensors by relaying information through the coaxial power cable.

PHASE II

Phase II of the project involved the detailed modelling of the built-in capacitive and inductive sensor types in MATLAB. The nature of the transfer function obtained with the built-in capacitive sensor was a flat curve (above 10 MHz) with a wide frequency band. However, the inter-turn capacitances and stray capacitance to the metallic earth sheath lead to an oscillating response with the inductive sensor. Hence, based on both the technical performance and the simplicity in construction, the built-in capacitive sensor was chosen as the final design for the PD sensor.

Subsequently, a series of experiments were performed on the built-in capacitive sensor design to validate its performance as was predicted by simulation. The tests ascertained the nature of the flat transfer function and the magnitude of transfer of the capacitive sensor reliably for frequencies upto 50 MHz. The results of the simulation model developed using MATLAB were comparable to the results of practical tests. An analysis was performed on the parameter variation of the design in order to check their influences on the final transfer function. The results where studied in order to assist in the selection of the best dimensions for the sensor unit.

The next series of tests were performed on the antenna concept to verify how they work when placed below the metallic earth screen of the coaxial power cable. The dipole antenna design was studied and tested specifically due to its simplicity in construction and ease of integration into the power cable (below the earth screen and over the outer semiconducting screen). Based on the results of the tests, the possibility of an antenna to radiate/resonate inside a power cable was affirmed. In other words, the antenna was able to inject EM waves into the cable, thereby creating propagating TEM waves. The radiation pattern of the antenna inside the power cable is certainly different from that in air. However, the existence of a radiation pattern by itself provides an opportunity to utilize it as a transceiver inside the cable. The basic performance of a dipole antenna as a receiver and transmitter when implemented below the earth screen of the power cable has been analysed and documented. The research indicates an overall promising performance of the dipole antenna.

7.2 Answers to research questions

1. **Which PD sensing technology is most suitable for long power cables?**
   The electrical PD sensing methods, such as the capacitive and inductive methods are most suitable for PD measurements on power cables. However, the compactness of the capacitive sensor makes it more suited for the built-in application in cables.

2. **Is it feasible to implement sensors distributed along the cable? If yes, what are the requirements and constraints of such a system?**
   Initial research shows that it is feasible to implement sensors at distributed locations along the cable if the challenge of PD detection, communication and power supply can be solved. The major constraint of this system is the extremely limited space (∼1 mm) available below the earth screen of the cable for sensor inclusion. The extreme conditions inside the power cable, such as: high electric and magnetic fields, high temperature and high pressures among many others also pose as a constraint to sensor implementation. The success of all three parts is crucial to the overall project and defines its feasibility.

3. **How will the multiple sensors synchronize and communicate?**
   It has been proposed in this master thesis that the most efficient communication scheme for the distributed sensors will be a relayed topology via the coaxial power cable. In account of this, an investigation on the application of antennas in power cables was conducted. This was done as a first step towards fulfilling this role. However, more research needs to be conducted in order to realize the complete communication scheme.

4. **What will be the performance of such a system?**
   One of the objectives of the master thesis was to quantify the performance of the PD sensor block and a potential communication device. In account of this, the transfer functions and sensitivity of the built-in capacitive sensor were obtained. The sensitivity of which is a peak voltage output of 1 mV towards a 10 pC PD, 300 m away from its source. Similarly, the transfer function and sensitivity of the dipole antenna design were obtained. The dipole antenna shows a coupling coefficient of 20% to the TEM waves in the cable when functioning as a receiver and 10% coupling coefficient towards each channel (two opposite cable arms) in the coaxial cable when functioning as a transmitter. Based on estimations the dipole antenna could also measure a 10 pC PD pulse, 300 m away from its origin with a peak voltage output of 3.75 mV.

7.3 Recommendations for future work

The limited time span of the master thesis permitted the investigation on antenna designs for communication only to a certain extent. Although the theory and scientific principle of their operation has been attempted to be explained based on simulations and experiments. There is a need to build a concrete theory and a model that can accurately predict the functioning of an antenna-like element inside the power cable. Since this investigation is the first of its kind, no definitive remarks could be made at this stage. However, research so far gives it a good leverage in the specific application and there is immense scope for future research in this field of study.

In summary, to realize the proposed distributed sensing scheme with built-in sensors, a list of other tasks have to be accomplished. They are as follows;

- All the influencing factors need to be accounted for, allowing the development of a more accurate simulation model with antennas. As this will provide a deeper insight into their principle of working and also allow the prediction of various design features without the need for trial and error.
- An empirical formula can be developed to facilitate the prediction of the resonant frequency of the antennas inside the power cable based on the effective relative permittivity of the dielectric and other structural design features.
- The power requirements of the sensing scheme need to be estimated and the power supply of the sensors needs to be designed.
- The requirement of a sensor isolation scheme in case of a fault conditions needs to be studied and developed.
- The interconnection between the various system blocks with suitable back-end electronics needs to be designed. Additionally, the feasibility of their inclusion below the metallic earth sheath of the cable needs to be studied.

APPENDIX

A

SIGNAL PROCESSING

This appendix summarizes the definitions involved with time-discrete signals that are used throughout this thesis, both in time and frequency domain.

A.1 Fast Fourier Transform

Fast Fourier Transform uses the DFT (Discrete Fourier Transform) algorithm. It converts a finite sequence of equally-spaced samples of a function into an equivalent-length sequence of equally-spaced samples of the discrete-time Fourier transform (DTFT), which is a complex-valued function of frequency. Mathematically it can be expressed through the expression:

$$X_k = \sum_{n=0}^{N-1} x_n e^{-i2\pi kn/N} = \sum_{n=0}^{N-1} x_n [cos(2\pi kn/N) - i.sin(2\pi kn/N)]$$

where x_1, x_2, x_3,...,x_k is the discrete time signal and X_1, X_2, X_3,...,X_k is the discrete sampled signal in frequency domain. When Discrete Fourier Transform is used for signal spectral analysis the conversion of the continuous time signal x(t) to discrete time signal x[k] leads to distortion in the fourier transform, now the DFT is called

DTFT (Discrete Time Fourier Transform), the associated distortion is termed as 'aliasing'. This can be avoided by using the right sampling rate, such that the Nyquist frequency is equal to half the sampling frequency ($F_{nyq} = F_s/2$).

Time and frequency domain signals

If the continuous signal in time domain is given by y(t) then the discrete time sampled signal output of the oscilloscope is given by y[k] where k is the index of the samples. It can be expressed in terms of y(t) as:

$$y[k] = y(t_k) = y(k\triangle t)$$

Similarly, if the continuous signal in the frequency domain is given by Y(ω) then the discrete frequency sampled signal is given by Y[i]. It can be expressed in terms of Y(ω) by:

$$Y[i] = Y(\omega_i) = Y(\omega i\triangle f) = \sum_{k=0}^{N} y[k]e^{-j\omega i\triangle f k\triangle t} = DFT(y[k])$$

where i the index of the discrete frequency samples ranging from 1 to N-1 and $\triangle f$ is the frequency resolution of the DFT in Hz. It is given by;

$$\triangle f = \frac{1}{N\triangle t}$$

As all the acquired signals are bandwidth limited, the frequency domain signal Y[i] contains frequency components from 0 Hz upwards to the Nyquist frequency. The indices above the Nyquist frequency are a mirror of the ones before, this is called aliasing in signal processing terms.

The discrete sampled signals from frequency domain can also be converted back to discrete time signals using the Inverse Discrete Fourier Transform (IDFT). It is given by;

$$y[k] = \sum_{i=0}^{N-1} Y[i]e^{j2\pi i\triangle f k\triangle t} = IDFT(Y[i])$$

APPENDIX

B

ANTENNA THEORY

B.1 General equivalent circuit

The *IEEE Standard Definitions of Terms for Antennas* (IEEE Std 145–1983) defines antennas as a means for receiving and radiating radio-waves. The thevenin's equivalent circuit of an antenna as a transmitter is given in Figure B.1. The source is represented by an ideal voltage generator V_g with an impedance of Z_g. A transmission line with a characteristic impedance Z_c is connected to the antenna which is represented by an impedance, $Z_A = (R_L + R_r) + jX_A$. The resistance R_L represents the conduction and dielectric losses associated with the antenna structure, the term R_r represents the *Radiation resistance* which is due to the antenna radiation. The last term X_A is the imaginary part of the impedance associated with the radiation of the antenna.

In most cases, the mismatch of the characteristic impedance of the transmission line and the antenna leads to problems of reflections and standing wave as shown in Figure B.1. Maximum power is delivered to the antenna in the case of *Conjugate matching*, when both the impedances are equal. In improperly designed systems the transmission line could act as a energy storage element instead of a wave guiding device.

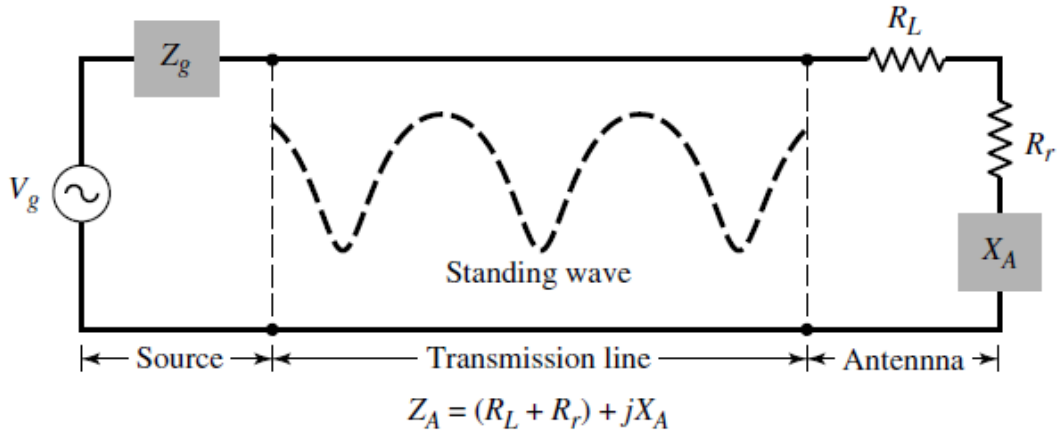

Figure B.1: Thevenin's equivalent circuit of an antenna as a transmitter[21]

B.2 Current distribution in a dipole

If the diameter of each wire is very small ($d << \lambda$), the ideal standing wave pattern of the current along the arms of the dipole is sinusoidal with a null at the end. However, its overall form depends on the length of each arm. For center-fed dipoles with $l << \lambda, l = \lambda/2, \lambda/2 < l < \lambda$ and $\lambda < l < 3\lambda/2$, the current patterns are illustrated in Figures B.2(a–d). The current pattern of a very small dipole (usually $\lambda/50 < l \leq \lambda/10$) can be approximated by a triangular distribution since $sin(kl/2)$ $kl/2$ when kl /2 is very small. This is illustrated in Figure B.2(a). Because of its cyclical spatial variations, the current standing wave pattern of a dipole longer than $\lambda(l > \lambda)$ undergoes 180° phase reversals between adjoining half-cycles. Therefore the current in all parts of the dipole does not have the same phase. This is demonstrated graphically in Figure B.2(d) for $\lambda < l < 3\lambda/2$. In turn , the fields radiated by some parts of the dipole will not reinforce those of the others. As a result severe interference and cancelling effects will be noted in the radiation pattern.

It is also interesting to see the current distribution over a straight dipole of length $\lambda/2$ at different time instances, this is shown in Figure B.3

B.3 Radiation characteristics of a patch antenna

Microstrip antennas, as shown in Figure B.4, consist of a very thin (t<< λ_0, where λ_0 is the free-space wavelength) metallic strip (patch) placed a small fraction of a

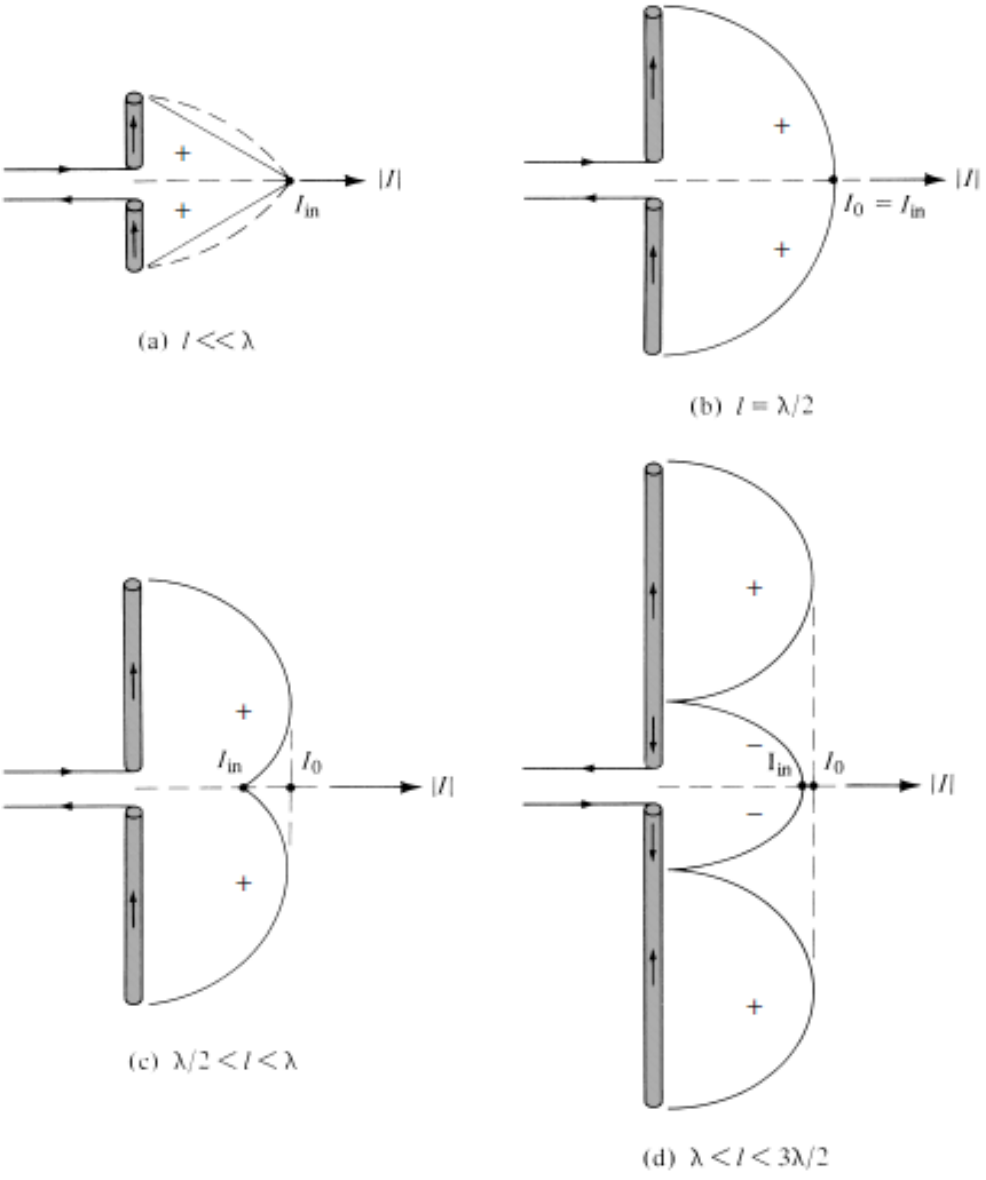

Figure B.2: Current distribution in a linear dipole[21]

wavelength (h<< λ_0, usually $0.003\lambda_0 \leq h \leq 0.05\lambda_0$) above a ground plane. The microstrip patch is designed so its pattern maximum is normal to the patch (broadside radiator)[40].

For a rectangular patch, the length L of the element is usually $\lambda_0/3 < L < \lambda_0/2$. The strip (patch) and the ground plane are separated by a dielectric sheet (referred

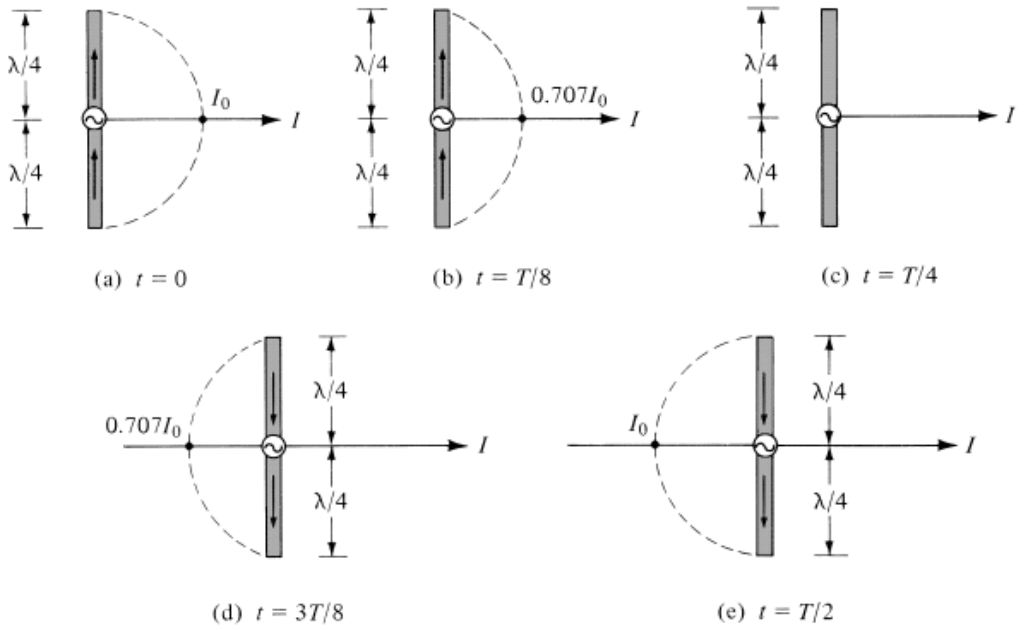

Figure B.3: Current distribution in a linear dipole at different times[21]

to as the substrate).

The functioning of a micro-strip antenna can be described in 2 ways, using the transmission line model or the cavity model. The transmission line model is more commonly used, it represents the patch antenna as 2 slots separated by a low impedance of Zc (of the transmission line of length L) as shown in Figure B.4. Whereas, the cavity model treats it like a cavity bound by electric conductors (above and below it) and by magnetic walls along the perimeter of the patch.

When a micro-strip patch is energized, a charge distribution as shown in Figure B.5 is established. Due to attractive and repulsive forces between opposite and like charges respectively, small surface currents J_t and J_b flow on the top and bottom surface. A small amount of current flows across the edges, however, when the height to width ratio is decreased, this current decreases. So in an ideal case the walls of the patch are considered to be perfect magnetic conductors so that there is no tangential component of magnetic field. Therefore, this model provides a normalized electric and magnetic field distribution below the patch.

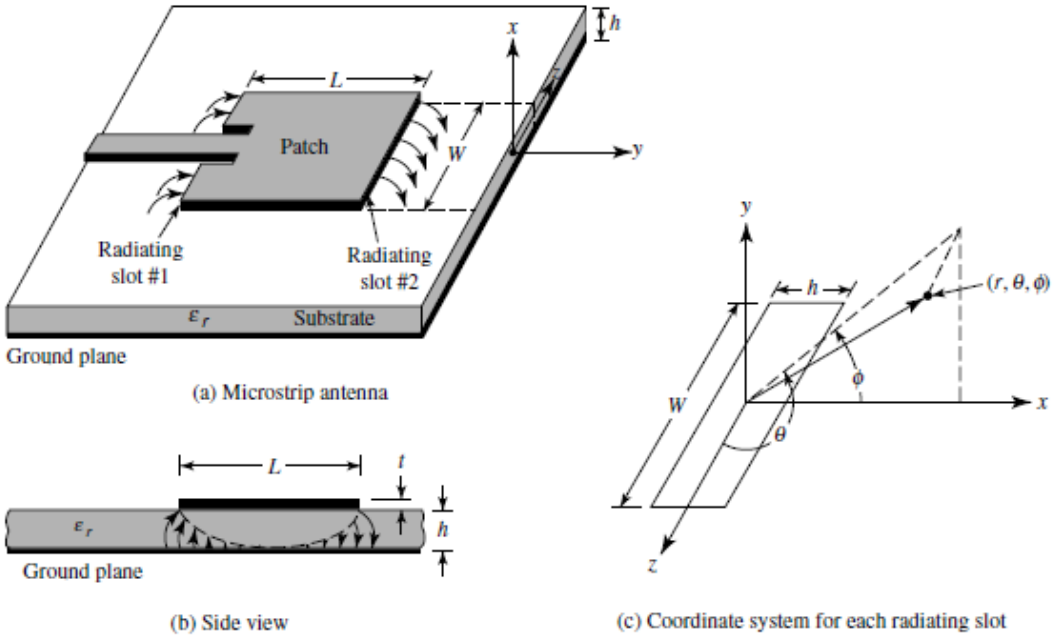

Figure B.4: Micro-strip antenna [21]

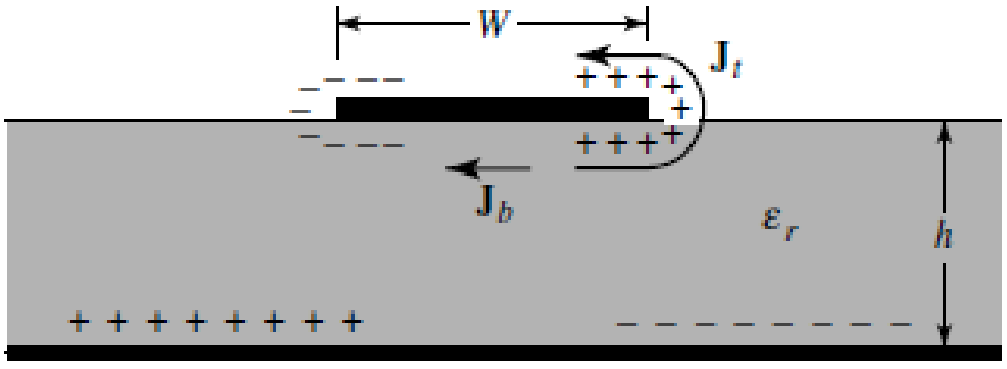

Figure B.5: Charge distribution on a micro-strip antenna [21]

BIBLIOGRAPHY

[1] Frederik H Kreuger. *Partial discharge detection in high-voltage equipment.* Butterworth-Heinemann, 1989.

[2] EF Steenis, Robert Ross, Nico Van Schaik, Wim Boone, and Dick M Van Aartrijk. Partial discharge diagnostics of long and branched medium-voltage cables. pages 27–30, 2001.

[3] M Muhr, T Strehl, E Gulski, K Feser, E Gockenbach, W Hauschild, and E Lemke. Sensors and sensing used for non-conventional pd detection. *CIGRE, Paris*, pages 1–7, 2006.

[4] R MacKinlay. Measurement of remaining life of hv cables: part 1 experiences in the field. 1986.

[5] EF Steennis, E Hetzel, and CWJ Verhoeven. Diagnostic medium voltage cable test at 0.1 hz. pages 408–414, 1991.

[6] N Van Schaik, EF Steennis, W Boone, and DM van Aatrijk. Partial discharge diagnostics on very long and branched cable circuits. 2001.

[7] Y Tian, PL Lewin, and AE Davies. Comparison of on-line partial discharge detection methods for hv cable joints. *IEEE Transactions on Dielectrics and Electrical Insulation*, 9(4):604–615, 2002.

[8] Min Chen, Koji Urano, Zhipeng Zhou, and Tengbiao Chen. Application study of variable pd sensors for pd measurement of power cable circuit in operation. pages 118–122, 2016.

[9] PCJM Van Der Wielen, J Veen, PAAF Wouters, and EF Steennis. Sensors for on-line pd detection in mv power cables and their locations in substations. 1:215–219, 2003.

[10] Peter CJM Van Der Wielen, Jeroen Veen, Peter AAF Wouters, and E Fred Steennis. On-line partial discharge detection of mv cables with defect localisation (pdol) based on two time synchronised sensors. pages 1–5, 2005.

[11] Ehsan Azordegan and Behzad Kordi. Remote assessment of high voltage insulators using wideband electromagnetic radiation signature. *IEEE Transactions on Dielectrics and Electrical Insulation*, 23(3):1467–1474, 2016.

[12] Rodrigo Paludo, Guilherme Cunha da Silva, and Vitoldo Swinka Filho. The study of semiconductor layer effect on underground cables with time domain reflectometry (tdr).

[13] Gavita Mugala, Roland Eriksson, Uno Gafvert, and P Petterson. Measurement technique for high frequency characterization of semiconducting materials in extruded cables. *IEEE transactions on dielectrics and electrical insulation*, 11(3):471–480, 2004.

[14] M Hasheminezhad and M Vakilian. Direct introduction of semicon layers in a cable model. *Scientia Iranica*, 15(2):203–210, 2008.

[15] Tongzhi Zhang, Fufei Pang, Huanhuan Liu, Jiajing Cheng, Longbao Lv, Xiaobei Zhang, Na Chen, and Tingyun Wang. A fiber-optic sensor for acoustic emission detection in a high voltage cable system. *Sensors*, 16(12):2026, 2016.

[16] E Lemke. A critical review of partial-discharge models. *IEEE Electrical Insulation Magazine*, 28(6), 2012.

[17] Ieee standard for high-voltage switchgear (above 1000 v) test techniques - partial discharge measurements. *IEEE Std C37.301-2009*, pages c1–63, March 2009.

[18] Steven Boggs, Ash Pathak, and Philip Walker. Partial discharge. xxii. high frequency attenuation in shielded solid dielectric power cable and implications thereof for pd location. *IEEE Electrical Insulation Magazine*, 12(1):9–16, 1996.

[19] GC Stone and SA Boggs. Propagation of partial discharge pulses in shielded power cable. pages 275–280, 1982.

[20] E Pultrum. On-site testing of cable systems after laying, monitoring with hf partial discharge detection. 1995.

[21] Constantine A Balanis. Antena theory. 2012.

[22] COMSOL Inc. RF module User's Guide version 4.3, 2012.

[23] Jingzhou Hou, Hui Ding, Bin Wei, Chao Gao, and Xianli Li. Microfiber knot resonator based electric field sensor. *Instrumentation Science & Technology*, 45(3):259–267, 2017.

[24] Celso Gutiérrez-Martínez, Gregorio Trinidad-García, and Jorge Rodríguez-Asomoza. Electric field sensing system using coherence modulation of light. *IEEE Transactions on instrumentation and Measurement*, 51(5):985–989, 2002.

[25] Lu Wan, Yu Chen, Yonghong Yin, Wei Jia, Yiying Liu, Yonghong Cheng, and Sergio A Pignari. Multiphysics modeling and analysis of integrated optical e-field sensor for sub-nanosecond intense electromagnetic pulse measurement. pages 131–134, 2016.

[26] Peng Zhang, Hong Hu, Fayyaz Muhammad, and Yulin Lei. High frequency passive micro-magnetic sensor based on surface acoustic wave transponder and giant magnetoimpedance sensitive element. *Sensors and Actuators A: Physical*, 254:54–60, 2017.

[27] Wentao Qiu, Abdoulaye Ndao, Huihui Lu, Maria-Pilar Bernal, and Fadi Issam Baida. Guided resonances on lithium niobate for extremely small electric field detection investigated by accurate sensitivity analysis. *Optics express*, 24(18):20196–20209, 2016.

[28] Xingyu Zhang, Amir Hosseini, Harish Subbaraman, Shiyi Wang, Qiwen Zhan, Jingdong Luo, Alex K-Y Jen, and Ray T Chen. Integrated photonic electromagnetic field sensor based on broadband bowtie antenna coupled silicon organic hybrid modulator. *Journal of Lightwave technology*, 32(20):3774–3784, 2014.

[29] L Zhong, Y Xu, G Chen, AE Davies, Z Richardson, and SG Swingler. Use of capacitive couplers for partial discharge measurements in power cables and joints. In *Solid Dielectrics, 2001. ICSD'01. Proceedings of the 2001 IEEE 7th International Conference on*, pages 412–415. IEEE, 2001.

[30] Ming Ren, Ming Dong, Zhong Ren, Hua-Dong Peng, and Ai-Ci Qiu. Transient earth voltage measurement in pd detection of artificial defect models in sf6. *IEEE Transactions on Plasma Science*, 40(8):2002–2008, 2012.

[31] Yanqun Liao, Bing Feng, Xiao Gu, Tingxi Sun, Yang Xu, and Zhengpeng Zhang. Application of the online partial discharge monitoring for the ehv xlpe cable system. In *Condition Monitoring and Diagnosis (CMD), 2016 International Conference on*, pages 896–899. IEEE, 2016.

[32] Jonas Norpoth, Stephanie Mildner, Malte Scherff, Jörg Hoffmann, and Christian Jooss. In situ tem analysis of resistive switching in manganite based thin-film heterostructures. *Nanoscale*, 6(16):9852–9862, 2014.

[33] Gaetano Marrocco. The art of uhf rfid antenna design: Impedance-matching and size-reduction techniques. *IEEE antennas and propagation magazine*, 50(1), 2008.

[34] Peng Zhang, Hong Hu, Fayyaz Muhammad, and Yulin Lei. High frequency passive micro-magnetic sensor based on surface acoustic wave transponder and giant magnetoimpedance sensitive element. *Sensors and Actuators A: Physical*, 254:54–60, 2017.

[35] Tetsuya Kusumoto and Yoshikazu Furuta. Wireless power transfer for in-vehicle contact-less power line communication systems. pages 1–3, 2016.

[36] Vikram Gupta, Arvind Kandhalu, and Ragunathan Raj Rajkumar. Energy harvesting from electromagnetic energy radiating from ac power lines. page 17, 2010.

[37] Lanxiang Wang, Menglong He, Zhao Wang, Mark Leach, Jingchen Wang, Kalok Man, and Eng Gee Lim. Radio frequency energy harvesting technology. pages 219–220, 2016.

[38] Ruslan Papazyan and Roland Eriksson. Calibration for time domain propagation constant measurements on power cables. *IEEE Transactions on Instrumentation and Measurement*, 52(2):415–418, 2003.

[39] Paul Wagenaars. Integration of online partial discharge monitoring and defect location in medium-voltage cable networks. 2010.

[40] Ramesh Garg. *Microstrip antenna design handbook*. Artech house, 2001.

NOMENCLATURE

Abbreviations

$CBLUT$	Cable Under Test
EM	Electromagnetic
EMF/emf	Electro Motive Force
EMW	Electro Magnetic Waves
$EPIR$	Electro Pulse Induced Resonance
FFT	Fast Fourier Transform
GIS	Gas Insulated Substation
HD	Harmonization Document
HF	High Frequency
$HFCT$	High Frequency Current Transformer
HV	High Voltage
IEC	International Electro-technical Commission
MV	Medium Voltage
PD	Partial Discharge
$PDOL$	PD Detection On-line with Localization
PE	Polyethylene
$RFCT$	Radio Frequency Current Transformer
$RFID$	Radio Frequency Identification
SCG	Smart Cable Guard
SNR	Signal to Noise Ratio
TEM	Transverse Electro Magnetic
TEV	Transient Earth Voltage
TF	Transfer Function
UHF	Ultra High Frequency
VNA	Vector Network Analyser

Symbols

α	Cable attenuation	Np/m or dB/m
β	Phase velocity	rad/m
$\epsilon^{''}$	Complex part of specific dielectric constant	-
$\epsilon^{'}$	Real part of specific dielectric constant	-
ϵ_o	Dielectric permittivity	F/m
ϵ_r	Relative permittivity	-
Γ	Voltage transmission coefficient	-
γ	Propagation constant of the cable	Np/m
Γ_V^+	Transmission coefficient from meas. cable to CBLUT	-
Γ_V^-	Transmission coefficient from CBLUT to meas. cable	-
λ	Wavelength	m
μ_o	Magnetic permeability	H/m
ω	Angular velocity	rad/s
ϕ	Diameter	m
ϕ	Flux output	Wb
σ	Conductivity	S/m
τ	Voltage reflection coefficient	-
$\vec{B}$	Magnetic flux density	Wb/m^2
C	Capacitance	F
c	Velocity of light in vacuum	m/s
C^*	Complex capacitance	F
C_{is}^*	Complex capacitance of inner screen	F
C_{os}^*	Complex capacitance of outer screen	F
C_o	Geometric capacitance	F
C_w	Inter-winding capacitance	F
C_{coax}	Capacitance of measuring coax	F
C_{ins}	Capacitance of insulation	F
C_s	Stray capacitance to cable earth screen	F
f	Frequency	Hz
G	Conductance	Ω^{-1}
H_{meas}	Reflection coefficient of the measurement cable	-
i	Current in time domain	A
i_{cable}	Current in time domain	A
I_{pr}	Current in primary circuit in frequency domain	A
k_o	Wave number of free space	rad/m
L	Inductance	H
L_c	Self inductance of the coil	H
M	Mutual inductance	H
R	Resistance	Ω

R_s	Axial resistance of outer screen	Ω
t	Instantaneous time of the pulse	s
t_h	Transmission time for each hop	s
V	Voltage in frequency domain	V
v	Voltage in time domain	V
V_o	Output voltage	V
V_o^+	Voltage of forward travelling wave	V
V_o^-	Voltage of backward travelling wave	V
V_p	Phase velocity	m/s
V_r	Voltage of reflected pulse	V
V_{inj}	Voltage of injected pulse	V
V_{in}	Input voltage	V
X_{sensor}	Reactance of sensor	Ω
y	Admittance	Ω^{-1}
z	Instantaneous distance of the pulse	m
Z_c	Characteristic impedance	Ω
Z_L	Load impedance	Ω
Z_m	Impedance of measurement equipment	Ω
Z_{adpt}	Impedance of the adapter	Ω
Z_a	Input impedance of the antenna	Ω
$Z_{c-CBLUT}$	Characteristic impedance of the CBLUT	Ω
Z_c	Characteristic impedance of the measurement cable	Ω
Z_t	Transfer impedance of HFCT	Ω
L	Length on sensor inner electrode	cm
q	Induced charge	C
S11	Forward reflection coefficient	-
th	Thickness of sensor insulation	mm
W	Width on sensor inner electrode as a % of cable circumference	%